

Preliminary Feasibility Analysis of Tubular Braided Composites Composed of Natural Fibers

by

Brianna Maria Bruni-Bossio

A thesis submitted in partial fulfillment of the requirements for the degree of

Master of Science

Department of Mechanical Engineering
University of Alberta

© Brianna Maria Bruni-Bossio, 2018

Abstract

Naturally derived or “green” based materials are increasing in demand for use as reinforcement and matrix materials in composites. However, it is still relatively unknown how well these materials can perform as constituents in tubular braided composite materials. In this work, tubular braided composites were manufactured with 100% cellulose natural fibres and two different types of high-bio content resins. The viability of these materials is evaluated by two different studies. In the first study, the sample preparation and quality control is evaluated by examining the final geometry and microstructure of the samples with the use of micro-computed tomography (μ CT). With the use of μ CT imaging, the void content, fibre volume fraction, final diameter and braid angle of each sample are quantified and visualized into 3D solid models. In the second study, the tensile elastic properties are determined by measuring the 3D deformation with stereo-digital image correlation. There are two main contributions from this work. For one, these materials are capable of producing high-quality composite materials with consistent mechanical properties and low content of voids and imperfections. In addition, due to their reasonable properties and very low density, their specific stiffness properties are comparable to e-glass braided composites. A feasible application could be low load-bearing applications inside automotive vehicles and other non-critical structures, sports equipment.

Acknowledgements

Firstly, I would like to thank my main supervisor Dr. Jason Carey for his unwavering guidance and support throughout my Master's degree. Dr. Carey provided me with many opportunities to grow as a person as well as a researcher over the past 2 years. Dr. Carey went above and beyond to help me to develop myself professionally on top of my research work, and I am extremely grateful to have had such an amazing supervisor during this experience.

Secondly, I would like to thank my second supervisor Dr. Cagri Ayranci for his support and suggestions with any questions or concerns I had with my research project.

Thirdly, I would like to thank Dr. Garrett Melenka, who was a great mentor to me throughout this experience, both technically and professionally. The many things I learned from Dr. Melenka helped me through graduate school and will continue to help me in my career to come.

Fourthly, I would like to thank everyone in my lab group throughout the years. In my lab, I was extremely lucky to be surrounded by some of the most brilliant and kind individuals I know, which made my graduate school experience so much more enjoyable. I am truly honoured to have had the opportunity to work with (and learn from) this exceptional group of people.

Finally, I would like to thank my family and friends for their unconditional encouragement and emotional support throughout my degree.

Table of Contents

Chapter 1	Introduction.....	1
1.1	Motivation	1
1.2	Thesis Scope.....	1
1.3	Thesis Outline	2
1.4	References	3
Chapter 2	Literature Review.....	4
2.1	Composite Materials	4
2.2	Tubular Braided Composites.....	5
2.3	Natural Fiber Polymer Composites (NFPCs).....	8
2.3.1	Definition	8
2.3.2	Green Materials.....	8
2.3.3	Challenges Faced by Green Braids.....	11
2.3.4	Advances in Literature.....	13
2.4	Conclusions	17
2.5	References	17
Chapter 3	Sample Preparation and Quality Control Evaluation of Natural Fiber and Bio-Matrix Braided Composites	22
3.1	Introduction	22

3.2	Methods.....	24
3.2.1	Materials	24
3.2.2	Sample Preparation	25
3.2.3	Geometry Evaluation	29
3.2.4	μ CT Imaging.....	30
3.3	Results and Discussion.....	36
3.3.1	Geometry Measurement.....	36
3.3.2	Braid micro-structure	37
3.4	Conclusions	51
3.5	References	52
Chapter 4	Mechanical Testing of Cellulose Braided Composites.....	54
4.1	Introduction	54
4.2	Experimental Methods	55
4.2.1	Sample Preparation.....	55
4.2.2	Stereo-Digital Image Correlation (DIC)	56
4.2.3	Calibration.....	57
4.2.4	Testing.....	58
4.2.5	Image Processing and Correlation	61
4.2.6	Tensile Elastic Properties.....	64

4.3	Results and Discussion.....	65
4.3.1	Measurements	65
4.3.2	Calibration.....	66
4.3.3	Strain Mapping.....	67
4.3.4	Applied Load and Stress	71
4.3.5	Stress-Strain Curves.....	72
4.3.6	Tensile Elastic Properties.....	75
4.3.7	Comparison with Conventional Materials	79
4.4	Uncertainty.....	81
4.5	Conclusions	82
4.6	References	83
Chapter 5	Conclusions and Future Work	86
5.1	Conclusions	86
5.2	Recommendations/Limitations.....	88
5.3	Future Work	89
References	91

List of Figures

Figure 2-1: Maypole braiding machine. Two different systems of carriers are attached two horn gears which move along the perimeter in opposite directions, interlacing strands over and under each other to create a tubular braided preform around the mandrel.	6
Figure 2-2: Diagram of a preform braid, with annotations to highlight the key variables used in describing the braid geometry.....	7
Figure 3-1. Maypole braiding machine and components.....	25
Figure 3-2. Braiding head and take-up mechanisms used to manufacture the tubular braided preform	26
Figure 3-3. Illustration of a regular braid with key parameters used to define its architecture	27
Figure 3-4. Regular cured braids at three braid angles (a) 40°, (b) 50°, and (c) 60°, all cured without vacuum bagging with Ecopoxy resin.....	27
Figure 3-5. Schematic describing system used to cure Ecopoxy samples within a vacuum	28
Figure 3-6. Experimental setup of u-CT scanner with braided sample inside.....	30
Figure 3-7. (a) Shadow projection image produced from the x-ray scans with red line indicating particular image cross-section location (b) a sample cross sectional image created using reconstruction software with scale to demonstrate size.....	32
Figure 3-8. Example braid structure segmentation analysis (a) original braid sample reconstructed cross-section image and the results of segmentation of its (b) voids (c) fibers, and (d) resin	33
Figure 3-9. Flow chart describing process using binary segmentation to determine the fiber volume content of each braid sample.....	34
Figure 3-10. Flow chart describing process using binary segmentation to determine void content of braid sample	35

Figure 3-11. Visual comparison of the impregnation of resin in 50° preform samples under 3 different curing methods (a) hemp resin cured without vacuum bagging (b) Ecopoxy resin cured without vacuum bagging and (c) Ecopoxy resin cured with vacuum bagging	38
Figure 3-12. Visual comparison of the impregnation of Ecopoxy resin cured under vacuum bags for (a) 40° (b) 50° (c) 60°	40
Figure 3-13. Solid models showing segmentation results for samples 1 to 9: (a) 40° Ecopoxy, (b) 40° Vacuum-Bagged Ecopoxy, (c) 40° hemp resin, (d) 50° Ecopoxy, (e) 50° Vacuum-Bagged Ecopoxy, (f) 50° hemp resin, (g) 60° Ecopoxy, (h) 60° Vacuum-Bagged Ecopoxy, and (i) 60° hemp resin. Voids are shown in black and fibers are shown in legend colours at 30% transparency. Resin is omitted for clarity.....	42
Figure 3-14. A sliced view of voids present in samples 1 to 9 respectively. (a) 40° hemp, (b) 40° Ecopoxy, (c) 40° Ecopoxy vacuum-bagged, (d) 50° hemp, (e) 50° Ecopoxy, (f) 50° Ecopoxy vacuum-bagged, (g) 60° hemp, (h) 60° Ecopoxy, (i) and 60° Ecopoxy vacuum-bagged.	43
Figure 3-15. Fiber volume fraction for each sample calculated from μ CT results.....	44
Figure 3-16. Matrix volume fraction for each sample calculated from μ CT results	44
Figure 3-17. Void volume fraction for each sample calculated from μ CT results	46
Figure 3-18. Total number of voids present in each sample calculated from μ CT results	46
Figure 3-19. Void distribution at 40°, 50° and 60° braid angles for (a) Ecopoxy samples (b) Vacuum-Bagged Ecopoxy samples and (c) hemp samples	48
Figure 3-20. Sensitivity analysis on fiber and resin threshold limits; (a) selected threshold for fibers, and (b) a fiber threshold that is 1% greater.....	50
Figure 4-1. Image of cured samples at 3 different braid angles (a) 40°, (b) 50°, and (c) 60°	55
Figure 4-2. Image of a braid sample with high-contrast speckle pattern applied	56

Figure 4-3. Illustration of DIC strain field on a composite braid	57
Figure 4-4. Schematic with dimensions of stereo-calibration target	58
Figure 4-5. Schematic of experimental setup for tensile tests	59
Figure 4-6. Field of view for image capture during tensile test.....	60
Figure 4-7. Illustration of original image compared with processed image	61
Figure 4-8. Correlation algorithm configuration steps. (a) Define image mask, seeding points and subset size; and, (b) define correlation mode and expected deformation.	63
Figure 4-9. Overview of correlation process	64
Figure 4-10. Image identifying the reinforcement and resin rich regions	67
Figure 4-11. Images of a sample strain field produced at the image of maximum stress for at each braid angle; (a) 40°, (b) 50° and (c) 60°	69
Figure 4-12. Image of the virtual strain gage used to average strain over the field of view for an arbitrary image frame.....	69
Figure 4-13. (a) Graph demonstrating the sensitivity of the location of virtual strain gauge line on the output of strain for five different lines on Sample 15 (b) Stress-strain curve for sample 15 used to demonstrate sensitivity of strain gauge placement	71
Figure 4-14. Plot of the original noisy voltage data and voltage data with a zero-phase distortion filter as a function of time.....	72
Figure 4-15 Plot showing the stress-strain curves for five samples at each the three sample braid angles	73
Figure 4-16. Image comparison of the failure modes of the three different braid angles.....	75

Figure 4-17. Scatterplot showing the experimental results of longitudinal elastic modulus as a function of braid angle compared with values predicted by a model created by Melenka et al. [18]. Experimental results were fitted with a least squares regression line.....	77
Figure 4-18. Bar graph showing the variation in elastic modulus for each desired braid angle.....	78
Figure 4-19. Scatter plot showing the comparison of longitudinal elastic moduli of BioMid samples with several other studies on tubular braids comprised of conventional materials	80
Figure 4-20. Scatterplot showing the comparison of the ratio of longitudinal elastic modulus over density of the reinforcing fiber	81
Figure A-1. Illustration of the parameters used to calculate braid angle based on the picks per inch (PPI)	98
Figure A-2. Curves demonstrating the load calibration data	99
Figure B-3. DIC strain field at maximum stress for (a) sample 1 ($\sigma_{\max} = 53.3$ MPa), (b) sample 2 ($\sigma_{\max} = 46.0$ MPa), (c) sample 3 ($\sigma_{\max} = 53.0$ MPa), (d) sample 4 ($\sigma_{\max} = 51.4$ MPa), (e) sample 5 ($\sigma_{\max} = 45.9$ MPa), (f) sample 6 ($\sigma_{\max} = 28.1$ MPa), (g) sample 7 ($\sigma_{\max} = 24.3$ MPa), (h) sample 8 ($\sigma_{\max} = 21.0$ MPa), (i) sample 9 ($\sigma_{\max} = 19.6$ MPa), (j) sample 10 ($\sigma_{\max} = 29.3$ MPa), (k) sample 11 ($\sigma_{\max} = 9.48$ MPa), (l) sample 12 ($\sigma_{\max} = 14.9$ MPa), (m) sample 13 ($\sigma_{\max} = 9.70$ MPa), (n) sample 14 ($\sigma_{\max} = 14.3$ MPa) and (o) sample 15 ($\sigma_{\max} = 10.2$ MPa)	104
Figure B-4. Stress strain curve for sample 1 ($E = 3.33$ GPa)	105
Figure B-5. Stress strain curve for sample 2 ($E = 3.60$ GPa)	105
Figure B-6. Stress strain curve for sample 3 ($E = 3.74$ GPa)	106
Figure B-7. Stress strain curve for sample 4 ($E = 3.07$ GPa)	106
Figure B-8. Stress strain curve for sample 5 ($E = 4.20$ GPa)	107
Figure B-9. Stress strain curve for sample 6 ($E = 2.50$ GPa)	107

Figure B-10. Stress strain curve for sample 7 ($E = 2.67$ GPa)	108
Figure B-11. Stress strain curve for sample 8 ($E = 2.09$ GPa)	108
Figure B-12. Stress strain curve for sample 9 ($E = 1.94$ GPa)	109
Figure B-13. Stress strain curve for sample 10 ($E = 2.42$ GPa)	109
Figure B-14. Stress strain curve for sample 11 ($E = 1.68$ GPa)	110
Figure B-15. Stress strain curve for sample 12 ($E = 1.99$ GPa)	110
Figure B-16. Stress strain curve for sample 13 ($E = 1.89$ GPa)	111
Figure B-17. Stress strain curve for sample 14 ($E = 2.14$ GPa)	111
Figure B-18. Stress strain curve for sample 15 ($E = 1.40$ GPa)	112
Figure C-1. Strain error as a function of rigid body displacement	115

List of Tables

Table 3-1. Description of 9 scanned samples	29
Table 3-2. Settings used in u-CT scan	30
Table 3-3. The braid angle measurements for all 9 samples measured from the radiograph images with ImageJ software compared with the desired braid angle.....	36
Table 3-4. The diameter measurements for all 9 sample made both from the cross-sectional images in CTAn and physically with a micrometer.....	37
Table 3-5. Average and deviation of fiber and matrix content per unit mm of sample length.....	45
Table 4-1. Results for the geometry measurements of all samples used in this study.....	66
Table 4-2. Pinhole calibration parameter results	66
Table 4-3. Elastic modulus and fit parameters calculated for each sample	76
Table 4-4. Variation in measured braid angle and elastic modulus.....	78
Table A-1. Calculated pick per inch setting on braiding machine to produce desired braid angles..	98
Table A-2. Magnification factor calibration	100

Chapter 1 Introduction

1.1 Motivation

The depletion of natural resources and increase in greenhouse gas emissions has recently given rise to efforts to reduce the environmental impact of a wide range of industries. In the composites industry, these efforts are being addressed by investigating the feasibility of natural-based reinforcement and matrix materials. The advantages of using bio-based materials for composite structures include the fact that they are renewable and mostly biodegradable, as opposed to conventional synthetic materials that are non-renewable and largely disposed of in landfills at their end of life [1].

However, the ability of these natural-based materials to perform as consistently and reliably as conventional materials is still relatively unknown. Some of the main challenges that have hindered the adoption of naturally-derived composite materials include poor fibre-matrix bonding and lower or inconsistent strength properties when compared with conventional synthetic materials [2,3].

Therefore, a preliminary feasibility analysis is required to determine if it is possible to manufacture strong and dependable braided composites with continuous natural fibres.

1.2 Thesis Scope

For this thesis, tubular braided composites composed of cellulose fibres and a bio-based resin will be manufactured and two separate studies will be undertaken to help understand their mechanical feasibility. The first study will assess the microstructure and content of voids and imperfections with the use of micro-computed tomography (μ CT) imaging. The second study will determine their tensile elastic properties. The results from the two studies will help to answer whether these materials may be used to fabricate reliable and consistent composite materials and if they are

mechanically viable for further research and development. It should be noted that this is a preliminary study and much more is required to determine the full viability of these materials. These include shear properties, durability and both an economic and emissions based life cycle analysis on the materials. However, these are out of the scope of this work.

1.3 Thesis Outline

This thesis consists of 5 chapters. Chapter 2 contains background information and a review of the current literature related to natural fibre braided composites. In chapter 3, the preparation and quality control of samples prepared with cellulose fibres and a bio-based resin are outlined. In this study, micro-computed tomography was used to investigate the interaction of the constituent materials and determine the effect of modifying braid angle, resin type, and curing method on fibre volume fraction, void volume and void distribution. In Chapter 4 study, the tensile properties of the samples are determined with the use of three-dimensional digital image correlation to compare performance with existing synthetic composites. In Chapter 5, the undertakings and findings of this study were summarized and the future work required is discussed.

Supplementary data, calculations and codes to support this work can be found in the appendices. In Appendix A the calibration and setup procedures for the equipment used are outlined. In Appendix B the full results for the DIC strain fields and stress-strain curves of all samples. Appendix C contains the calculations for an uncertainty analysis done to estimate the error in determining the elastic modulus.

1.4 References

- [1] X. Huang and A. N. Netravali, "Environment-Friendly 'Green' Resins and Advanced Green Composites," in *Cellulose Based Composites*, J. P. Hinestroza and A. N. Netravali, Eds. Wiley-VCH Verlag GmbH & Co. KGaA, 2014, pp. 137–155.
- [2] K. L. Pickering, M. G. A. Efendy, and T. M. Le, "A review of recent developments in natural fibre composites and their mechanical performance," *Compos. Part Appl. Sci. Manuf.*, vol. 83, pp. 98–112, Apr. 2016.
- [3] H. Lilholt and J. M. Lawther, "1.10 - Natural Organic Fibers A2 - Kelly, Anthony," in *Comprehensive Composite Materials*, C. Zweben, Ed. Oxford: Pergamon, 2000, pp. 303–325.

Chapter 2 Literature Review

2.1 Composite Materials

Composite materials are manufactured using a combination of two or more individual materials [4]. The mechanical properties of the combined materials differ from the mechanical properties of each constituent material individually [4]. Generally, composite materials consist of one strong fibrous material, called the reinforcing material, and one weaker binding resin material called the matrix [3]. The matrix helps to evenly distribute load amongst the fibers and maintain the fibers in a fixed shape [4]. The concept of composite materials go back as early humans built houses using straw as reinforcement in mud walls [5]. However, the methods of forming and fabricating composite materials as well as their applications have since been advancing in many different research areas. The composites market has grown to an \$8 billion industry in 2017 and is expected to expand to \$10.6 billion by 2022 [6]. The applications of composites are vast in a variety of industries such as automotive, aerospace, medical equipment, sports equipment, structural applications and many more. The main benefits of composites over metals include their high specific strength and stiffness, good corrosion resistance, durability, lower coefficient of thermal expansion, and ease of tailoring the material mechanics to obtain an optimal design for each application. E-glass and epoxy laminates can have a tensile elastic modulus of approximately 25 GPa along the fiber direction [7]. Carbon fiber and epoxy laminates have a tensile elastic modulus of approximately 85 GPa along the fiber direction [8]. Aluminum is known to have an elastic modulus of approximately 70 GPa, therefore certain types of composites have the ability to replace metals in some applications if designed appropriately. However, what makes composites most attractive are their specific properties compared to those of metals. For instance, aluminum has a density of 2800 kg/m^3 , carbon fiber has a density of 1800 kg/m^3 [4] making composites are very appealing for applications that

require high stiffness or strength while maintaining low weight. The favorable properties and versatility of composites are fueling the expansion of the industry.

The increased adoption of composites industry faces a few challenges, such as their high cost of manufacture, complexity in analysis and failure prediction, and low strength in directions that are not parallel to the fiber orientation. Additionally, modelling fiber-reinforced composites is challenging since the materials are heterogeneous and thus have anisotropic behavior. There is, however, an abundance of research addressing these issues showing promise for the future of the composites industry.

2.2 Tubular Braided Composites

Tubular braids are a particular type of fiber-reinforced composite often manufactured by interlacing fiber yarns around a mandrel in a specific pattern with a Maypole braiding machine [9], as shown in Figure 2-1.

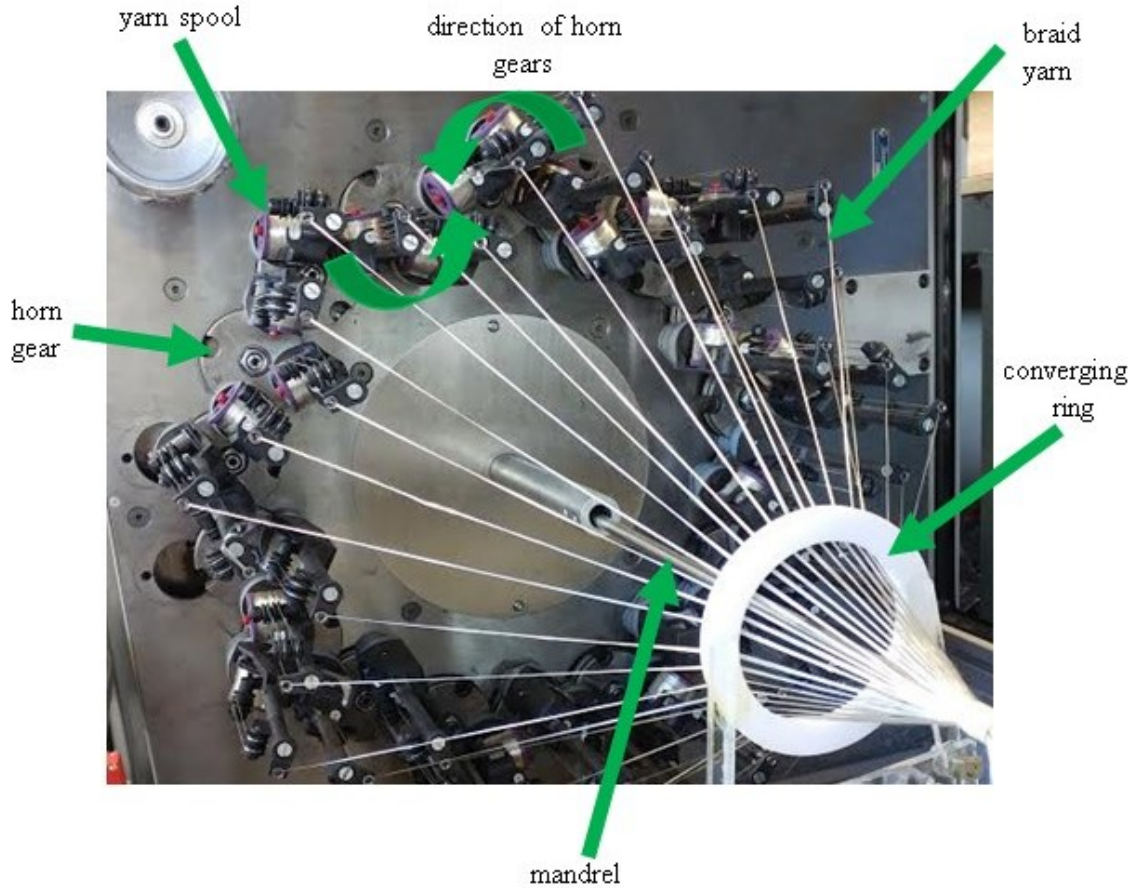


Figure 2-1: Maypole braiding machine. Two different systems of carriers are attached two horn gears which move along the perimeter in opposite directions, interlacing strands over and under each other to create a tubular braided preform around the mandrel.

As the carriers rotate and braid, the mandrel is pulled forward by a pneumatically operated belt system. From this process, there is a resulting hollow tube fiber preform as shown in Figure 2-2. The key variables involved in defining the architecture of the braid are annotated in the image. The properties of braids are highly dependent on these key variables [9]. As a result, braids are highly tailorable in their properties.

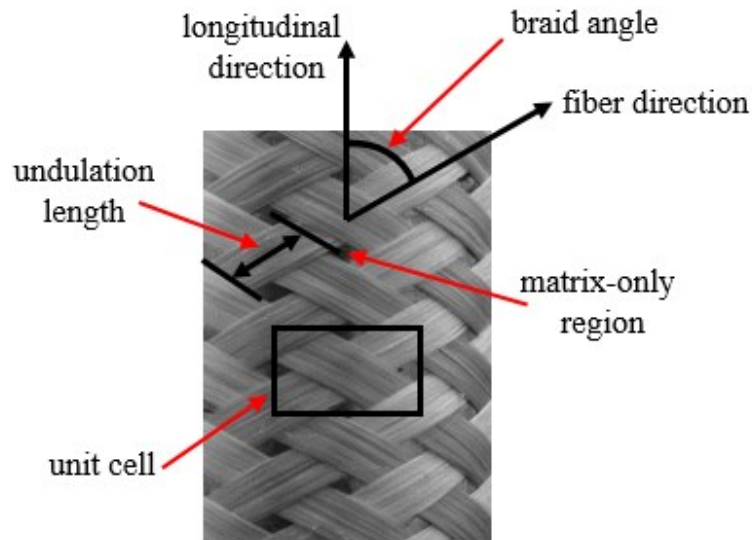


Figure 2-2: Diagram of a preform braid, with annotations to highlight the key variables used in describing the braid geometry.

Following the fabrication of the preform, the braid is impregnated with a resin and heated to the resin's curing temperature. This creates a matrix that contains the fibers in a hardened composite structure. Braiding as one means of making composites allows a high fiber deposition rate, greater strength under torsional loads and enhanced load distribution throughout the structure. Melenka *et al.* [10] examined the tensile and torsional properties of Kevlar tubular braided composites with varying braid angles. Under tensile loading, 40° braids produced a maximum modulus of 11.5 GPa. Under shear loading, samples with 50° braid angles produced a maximum shear modulus of 14 GPa.

Despite its benefits, there has been low adoption of braiding in industry. Adoption faces a few main challenges. Braiding has a high capital cost as the machinery required to braid the yarns are expensive. In addition, the yarn spools must be small enough to travel around the machine, and thus must be often rewound which is time extensive. The mechanical properties and behaviour of braids are not yet extensively developed [11]. Experimental repeatability is an issue since braided composites are very sensitive to changes in the key defining variables [5], and a small variation in braid angle or undulation length can affect the properties of the whole composite considerably.

Finally, due to restrictions from the geometry of the braids, their tensile stiffness and strength properties are generally not as great as unidirectional laminates [11].

2.3 Natural Fiber Polymer Composites (NFPCs)

2.3.1 Definition

In recent years, there has been an increase in awareness of the depletion of the world's natural resources and rise in greenhouse gas emissions. Due to this, there is a push to find ways to lessen our environmental impact. Braided composites that are currently the most commonly used are composed of synthetic materials. Both the fibers and resins are usually petroleum-based and thus composed of non-renewable resources. In addition, reuse or recycling of such materials is a challenge and over 90% of composites end up in landfills at the end of their life [1]. Replacing synthetic composites with “green” or natural-based composites is one way to decrease environmental impact. As another factor, with the fluctuating price of oil, it is also beginning to become economically viable to explore the development of engineering materials comprised of renewable sources. According to Vilaplana *et al.* [12], in order to design a sustainable composite one should consider (i) the use of renewable resources, (ii) processing methods be energy effective, (iii) no hazardous effects to the environment in any stage and (iv) proper waste management. In order to address these considerations, a complete life cycle analysis of the materials from their raw form to disposal should be performed. For this study, green braids will be defined as tubular braided composites that are composed of both natural fibers and a natural-based matrix.

2.3.2 Green Materials

2.3.2.1 Natural Fibers

Natural fibers are either plant-based or protein-based. For the purpose of the green braids examined in this thesis, only plant-based fibers will be investigated as they generally have shown potential for

much higher strength than animal fibers [2]. The use of natural fibers is not a novel concept. However, their applications have been mostly involved in the textile industry, and not often used as reinforcement in composite material structures [3]. While the main advantage of the use of natural fibers is the sustainability aspect of the resource, using them as reinforcements in fiber composites may offer some other benefits [13]. These fibers are abundantly available in nature, which makes them easier and less expensive to obtain than synthetic fibers. There are many different types of natural fibers that could be used as reinforcement in braided composites. All plant-based fibers are composed of differing combinations of cellulose, hemicellulose and lignin molecules. These fibers are collected from one of three different main groups; the bast surrounding the stem, the leaves, or the seed-hair of the plant. [14] The natural fibers that are most readily available for use in composites include flax, hemp, jute, kenaf, sisal, cotton, bamboo, or wood. [3]

The structure of all plant based fibers is based on the cellulose compound, which provides the majority of their strength [15]. It is also possible to extract and process the cellulose molecules to create high-strength 100% cellulosic continuous fibers [16]. There are approximately 1.5×10^{12} tons of cellulose created on earth each year [17], therefore it is abundantly available and being investigated heavily for use in composite materials.

Cellulose fibers are more ductile than glass fibers, as they have shown to have greater elongation at fracture [18]. The mechanical properties of natural fibers are typically less than most synthetic fibers [19], however, they are also lower in density [13]. Thus, their specific properties are in a similar range of glass fibers [19]. However, some natural fibers such as flax and hemp can range from a moduli of 27.6-70 GPa and 6-70 GPa [14] respectively, while commonly used E-glass fibers have a modulus of 72 GPa [9]. Thus if the full strength and stiffness potential of natural fiber composites are obtained, they should be able to replace glass fiber composite applications.

Another important consideration is that natural fibers may not be completely harmless to the environment. Since they are made from renewable resources and are biodegradable after their useful life, they have some exceptional environmental benefits. However, it is important to look at their entire impact during fabrication. Often these fibers require extensive processing in order to be converted to a usable continuous form for reinforcement. The processing step requires additional energy consumption.

2.3.2.2 Natural Resins

Both thermosets and thermoplastics may be used as the matrix material in braided composites. Synthetic resins usually used in tubular braided composites are typically thermosets as they have a low viscosity which allows easier impregnation [9]. However, resins that are naturally based are thermoplastics. These resins may still be used but they have a high processing viscosities [20], making impregnation of natural fibers a challenge. There is research that shows promising properties with natural fibers embedded in synthetic thermoset matrices [19]; however, there is very little literature that has examined the behavior of natural fibers embedded in natural thermoplastic matrices [3].

Producing useful natural based resins is one of the greatest challenges faced in developing green composites because resins composed of plant oils rarely have valuable properties [21]. However, many different modified natural materials have been explored as a replacement for current synthetic plastics and resins. Bio-based resins for composite matrix applications can be derived from many different natural sources. Polylactic acid (PLA) [22], soy [1,21], and starch [23] are the main natural polymer matrices that have been tested in natural composites.

The majority of composites that are reinforced with natural fibers still contain a synthetic matrix, such as polypropylene (PP). Oksman *et al.* [24] tested compression molded composites composed

of flax fibers and a PLA matrix and compared the results to composites made of flax fibers and a PP matrix. It was found that the pure PLA matrix composites had a modulus of 3.4 GPa while the pure PP matrix had a modulus of 1.3 GPa, showing that there is potential in PLA matrix composites. PLA is currently one of the leading matrix materials for bio-based composites and has been used in a vast number of other studies [22,25–27].

Resins derived from vegetable-oil sources especially have shown significant promise in several different studies. Huang *et al.* [1] examined the use of a resin made of a natural soy protein concentrate (SPC) that was modified with agar and Nano clay to improve its mechanical properties. The stiffness of unidirectional composites made with the modified cellulose fibers-reinforced SPC was 13.7 GPa, which shows potential from modified soy-based resins. Taylor *et al.* [21] showed that newly developed bio-resin made from epoxidized sucrose soyate (ESS) were shown to have the potential to produce properties equivalent to petrochemical epoxy resins. Pultruded composites composed of ESS reinforced with treated flax fibers produced stiffness values of up to 29.2 GPa. Currently, only a handful of partially bio-based resins are commercially available including GreenPoxy 56, an epoxy resin containing 56% plant-based ingredients, [28] Supersap, an epoxy resin containing 30% bio-based ingredients [29], and Ecopoxy, an epoxy resin containing 25% natural ingredients [30].

2.3.3 Challenges Faced by Green Braids

The progression of braided composites made of natural fibers and natural resins has been limited due to several barriers. As mentioned earlier, braided composites face some key challenges when compared to other manufacturing methods. Green based composites provide additional challenges, and thus green braids have been extremely limited in their development in the composite industry. In theory, natural fibers should be able to provide reinforcement in braided composites in the same

manner as commonly used synthetic fibers [2]. However, several factors prevent them from doing so.

One of the greatest challenges of green braids is the unpredictability of plant-based fibers. Natural fibers are not as consistent in their characteristics as manufactured synthetic fibers are. There is no control over the growing phase of plants that the natural fibers are derived from. The properties depend on many different factors such as the growing conditions, type of plant, climate, age of plant and method used to fabricate the fiber from the plant [19]. As a result, every single fiber can vary in its chemical composition, crystallinity, surface properties, diameter, cross-sectional shape, length, strength, and stiffness [2]. The result is a large degree of variability in mechanical properties depending on the fiber sample. However, since continuous regenerated cellulose fibers are refined, processed and spun similar to synthetic fibers, they are capable of achieving more consistent mechanical properties [31].

The durability of natural fibers due to factors such as moisture, heat and UV radiation are another major concern with the development of these types of materials. Natural fibers may have high moisture absorption, as they are hydrophilic [2]. This is a challenge because any trace of moisture exposition could affect the integrity of the fibers and consequently the strength of the entire composite [14]. Espert *et al.* [32] found a decrease in elastic modulus with water absorption in cellulose-polypropylene composites. The decrease in elastic modulus was also more significant in composites with a greater fiber volume fraction.

The effect of UV radiation on the integrity of natural fibers has also been addressed in several studies. Yan *et al.* [33] studied the effects of both UV radiation on the mechanical properties of flax reinforced epoxy composite woven laminates. When the samples were exposed to UV light in an accelerated weathering chamber for 1500 hours, the tensile strength decreased by 30%. However,

other studies have shown that synthetic fibers also show degradation with UV exposure [34, 35], including up to 29% reduction in tensile strength with carbon/epoxy composites [36].

An additional concern about natural fibers is their increased flammability in comparison to synthetic materials [37]. The flammability of natural fibers has especially been shown to increase with the content of cellulose present in the composition [38]. There are fire retardant treatments available, however they require further research and development as they have generally shown to adversely affect the mechanical properties of the composite by weakening the interfacial bond of the fibers and matrix [39].

Aside from durability issues, what is possibly the most critical challenge is the bond between the fibers and matrix. While natural fibers are generally hydrophilic in nature, natural resins are generally hydrophobic; therefore, the outcome is poor matrix-fiber bonding with natural based composites. [40]. In addition, natural resins are typically thermoplastics with a high viscosity [20], which makes it difficult to impregnate the natural fibers because the fibers and matrix repel each other, preventing strong interfacial bonding. A good coupling between the fibers and matrix is essential to the overall strength of the braid; this is thus a critical challenge to overcome for the use of natural based composites to be viable. Braided composites in general face complications in the matrix-fiber bond due to the voids created in the manual impregnation and curing process [7].

Therefore, it likely that green braided composites may be especially difficult to impregnate.

2.3.4 Advances in Literature

To reiterate, the main reasons preventing the advancement of green composites in industry are the large variation in properties, moisture absorption and poor fiber-matrix adhesion. However, there are certain modifications that may be made to the surface of natural fibers in order to improve overall fiber-matrix coupling. Good bonding requires mechanical anchoring, molecular attractive

forces, and chemical bonds between the fiber and resins. [19] There are many types of physical and chemical modifications that are used to improve the fiber-matrix interface. [41] Depending on the type of surface modification, this could improve the coupling between the two surfaces, aid with impregnation of the resin, and/or reduce the fiber's sensitivity to moisture. [40]

2.3.4.1 Green Braids

Very few pieces of literature have looked into the potential of green braided composites in particular. Current braiding machines were designed for the use of synthetic fibers, which are denser and stronger than natural fibers. Due to this, Huber *et al.* [42] examined whether the process of braided processed cellulose fibers in a 3D braiding machine affected the integrity and strength of the fibers. It was determined that there was no significant damage to the fibers and therefore braiding is an acceptable method for manufacturing natural fiber reinforced composites.

Qamhia *et al.* [43] looked at the experimental and analytical properties of triaxially braided composites composed of cellulose fibers and a high-bio-content epoxy matrix. The longitudinal elastic moduli from the model and experiments were very similar at 11.67 GPa and 11.22 GPa respectively. Therefore, analytical models that are used to represent synthetic braids should be able to accurately predict green braids as well.

Despite the lack of research available on green braids, there has been a significant amount of research invested in green laminates and other types of composites.

2.3.4.2 Green Laminates

The majority of bio-based composites that are currently on the market are manufactured by moulding, extrusion or layup methods [12]. Faruk *et al.* [41] did a review of all biocomposites reinforced with natural fibers between 2000 and 2010. They identified bonding between the fiber

and matrix to be the main challenge faced by biocomposites and highlighted different surface treatment methods to overcome these issues. It was concluded that biocomposites were already showing a lot of promise in the automotive industry and with certain modifications to assist with issues such as property variability and moisture absorption, could be used for load bearing applications to replace conventional composites.

Surface modifications in order to improve the mechanical properties have gained the interest of many researchers to make successful green composites. Kabir *et al.* [44], found that the effects of different chemical treatments on cellulose fibers significantly improved the matrix-fiber bond, increasing the mechanical strength of the composite. Shikamoto *et al.* [20] used a shellac resin treatment on the surface of jute spun fibers to improve the interfacial properties of a weaved preform impregnated with a PLA resin by compression molding. It was found that the shellac treatment did improve the bonding, but too great a concentration did not allow impregnation of the bundles with the PLA resin as the fibers were bound to the shellac. Therefore, there was an optimal concentration of the treatment of 2.0 wt%. Yan *et al.* [45] examined the properties of flax fibers alone and in different thermoplastic, thermoset and biodegradable composites. It was determined that the fiber properties varied greatly among different samples and bonding between the fiber and matrix was a challenge. An alkali treatment on the fibers breaks them into small fibrils, creating a larger surface area for the matrix to surround [19]. Mwaikambo [17] looked at the tensile properties of jute fibers that were treated with an alkali substance to improve the surface topography and other inconsistencies in the fibers. Chemical modifications to the fibers with a duralin treatment have also proven to aid in fiber-matrix interfacial bonding. [45] Thus, while poor fiber-matrix bonding in natural composites is problematic, there is research to support that surface treatments can improve bonding to deliver promising mechanical properties.

Aside from surface modifications, there are other methods that have been successful in improving the challenges faced by green composites. Lebrun *et al.* [19] attempted to improve the variability in properties of both hemp and flax based fiber unidirectional composites by inserting thin layers of paper on either side of the natural fiber laminae preforms. It was found that the paper helped to improve cohesion of the fibers and reduce imperfections and greatly reduced the variability in strength amongst different samples. Ameri *et al.* [29] then optimized the flax/paper/epoxy composite parameters and was able to obtain a composite with a greater specific stiffness than E-glass/epoxy composites. Couture *et al.* [30] then created flax/paper/PLA composites and was able to obtain tensile properties similar to E-glass/epoxy composites with the biodegradable PLA matrix. Therefore, stacking thin paper among natural fiber laminae seems to be a solid method to optimize the mechanical properties.

Soykeabkaew *et al.* [48] looked at 100% cellulose composite laminates that were manufactured by partial dissolution of aligned cellulose fibers in a chemical solvent. The partial dissolution created a cellulose matrix surrounding the fibers. Since the composite is comprised completely of cellulose, the fibers and matrix showed good bonding and promising mechanical properties. As mentioned earlier, the incompatibility between hydrophilic natural fibers and hydrophobic matrices that are typically used is a large problem faced by green composites, but using the same chemical structure for the fiber and matrix solves this problem. In addition to excellent mechanical properties, all-cellulose composites exhibit very good biodegradability. Mass losses of up to 73% were found after samples were placed in soil for a duration of 70 days [49]. Due to these benefits, there are many other studies that have looked at similar dissolution methods to successfully create a binding matrix for cellulose composites [50-52].

2.4 Conclusions

At this time, there is no literature found that has investigated tubular braided composites composed of both natural-based fibers and natural-based matrix. However, there have been successes in other types of composites composed of natural sources. Many different types of plant-based fibers have shown potential to be valuable resources for fiber-reinforced composites. While fibers derived directly from plants have high moisture sensitivity and inconsistent properties, as well as poor fiber-matrix bonding, surface treatments are available to drastically improve on these weaknesses. In addition, regenerated cellulose fibers are able to achieve more consistent and predictable mechanical properties, similar to synthetics. The abundance of commercially available natural resins with sufficient properties, however, is still a large gap in the industry that requires further development. Due to the lack of literature available, a full feasibility analysis must be performed on tubular braided composites that are composed of natural fibers and matrix. As a preliminary feasibility analysis, the microstructure should be investigated to examine the impregnation of different resins or curing types and tensile tests should be performed in order to determine the elastic properties that may be achieved. Based on the results of such undertakings, a recommendation could be made on whether or not the concept of green braiding is in fact a viable idea to further explore.

2.5 References

- [1] D. Gay, S. Hoa, and S. Tsai, *Composite Materials: Design and Applications*. CRC Press, 2002.
- [2] H. Lilholt and J. M. Lawther, "1.10 - Natural Organic Fibers A2 - Kelly, Anthony," in *Comprehensive Composite Materials*, C. Zweben, Ed. Oxford: Pergamon, 2000, pp. 303–325.
- [3] C. Ayranci and J. Carey, "2D braided composites: A review for stiffness critical applications," *Compos. Struct.*, vol. 85, no. 1, pp. 43–58, Sep. 2008.

- [4] D. S. Mazumdar, D. Karthikeyan, D. Pichler, M. Benevento, and R. Frassine, "Composites Industry Report for 2017," *Composites Manufacturing Magazine*, 02-Jan-2017. [Online]. Available: <http://compositesmanufacturingmagazine.com/2017/01/composites-industry-report-2017/>. [Accessed: 26-Apr-2017].
- [5] Y. Wang, J. Li, and P. B. Do, "Properties of Composite Laminates Reinforced with E-Glass Multiaxial Non-Crimp Fabrics," *J. Compos. Mater.*, vol. 29, no. 17, pp. 2317–2333, Nov. 1995.
- [6] V. Çeçen, M. Sarikanat, H. Yildiz, and I. H. Tavman, "Comparison of mechanical properties of epoxy composites reinforced with stitched glass and carbon fabrics: Characterization of mechanical anisotropy in composites and investigation on the interaction between fiber and epoxy matrix," *Polym. Compos.*, vol. 29, no. 8, pp. 840–853, Aug. 2008.
- [7] J. P. Carey, *Handbook of Advances in Braided Composite Materials: Theory, Production, Testing and Applications*, Woodhead Publishing, 2016.
- [8] G. W. Melenka and J. P. Carey, "Experimental analysis of diamond and regular tubular braided composites using three-dimensional digital image correlation," *J. Compos. Mater.*, pp. 3887-3907, Jan. 2017.
- [9] A. P. Mouritz, M. K. Bannister, P. J. Falzon, and K. H. Leong, "Review of applications for advanced three-dimensional fibre textile composites," *Compos. Part Appl. Sci. Manuf.*, vol. 30, no. 12, pp. 1445–1461, Dec. 1999.
- [10] X. Huang and A. N. Netravali, "Environment-Friendly 'Green' Resins and Advanced Green Composites," in *Cellulose Based Composites*, J. P. Hinestroza and A. N. Netravali, Eds. Wiley-VCH Verlag GmbH & Co. KGaA, 2014, pp. 137–155.
- [11] F. Vilaplana, E. Strömberg, and S. Karlsson, "Environmental and resource aspects of sustainable biocomposites," *Polym. Degrad. Stab.*, vol. 95, no. 11, pp. 2147–2161, Nov. 2010.
- [12] K. L. Pickering, M. G. A. Efendy, and T. M. Le, "A review of recent developments in natural fibre composites and their mechanical performance," *Compos. Part Appl. Sci. Manuf.*, vol. 83, pp. 98–112, Apr. 2016.
- [13] P. L. Menezes, P. K. Rohatgi, and M. R. Lovell, *Tribology of Natural Fiber Reinforced Polymer Composites*, pp. 341–343, Jan. 2011.
- [14] R. Dunne, D. Desai, R. Sadiku, and J. Jayaramudu, "A review of natural fibres, their sustainability and automotive applications," *J. Reinf. Plast. Compos.*, vol. 35, no. 13, pp. 1041–1050, Jul. 2016.
- [15] L. Mwaikambo, "Tensile properties of alkalisated jute fibres," *Materials Science and Technology*, vol. 25, pp. 1289-1295, Jul 2009.
- [16] A. K. Bledzki and J. Gassan, "Composites reinforced with cellulose based fibres," *Prog. Polym. Sci.*, vol. 24, no. 2, pp. 221–274, May 1999.
- [17] T. Huber, J. Müssig, O. Curnow, S. Pang, S. Bickerton, and M. P. Staiger, "A critical review of all-cellulose composites," *J. Mater. Sci.*, vol. 47, no. 3, pp. 1171–1186, 2012.

- [18] J.-C. Zarges, C. Kaufhold, M. Feldmann, and H.-P. Heim, “Single fiber pull-out test of regenerated cellulose fibers in polypropylene: An energetic evaluation,” *Compos. Part Appl. Sci. Manuf.*, vol. 105, pp. 19–27, Feb. 2018.
- [19] A. Mohanty, M. Misra, and L. Drzal, Eds., *Natural Fibers, Biopolymers, and Biocomposites*. CRC Press, 2005.
- [20] N. Shikamoto, P. Wongsriraksa, A Ohtani, L Y Wei and A Nakai. “Processing and mechanical properties of biodegradable composites.” *The 9th International Conference on Flow Processes in Composite Materials*, Jul 2008.
- [21] C. Taylor, A. Amiri, A. Paramarta, C. Ulven, and D. Webster, “Development and weatherability of bio-based composites of structural quality using flax fiber and epoxidized sucrose soyate,” *Mater. Des.*, vol. 113, pp. 17–26, 2017.
- [22] A. Couture, G. Lebrun, and L. Laperrière, “Mechanical properties of polylactic acid (PLA) composites reinforced with unidirectional flax and flax-paper layers,” *Compos. Struct.*, vol. 154, pp. 286–295, 2016.
- [23] W. Li, Y. Zheng, L. Zhang, Z. Ou, and J. Zhou, “Preparation and characterization of nano-SiO₂/lignin-phenol-starch composite resin,” *Polymeric Mater. Sci. Eng.*, vol. 32, no. 5, pp. 23–27, 2016.
- [24] K. Oksman, M. Skrifvars, and J.-F. Selin, “Natural fibres as reinforcement in polylactic acid (PLA) composites,” *Compos. Sci. Technol.*, vol. 63, no. 9, pp. 1317–1324, Jul. 2003.
- [25] R. Aurus, L. Lim, S. Selke, H. Tsuji, *Poly (Lactic Acid): Synthesis, Structures, Properties, Processing, and Applications*, John Wiley and Sons, 2010.
- [26] P. Uawongsuwan et al., *Mechanical properties of poly (Lactic acid) based biocomposites: Comparison of different reinforcements*, vol. 2. 2013.
- [27] A. K. Bledzki, A. Jaszkiwicz, and D. Scherzer, “Mechanical properties of PLA composites with man-made cellulose and abaca fibres,” *Compos. Part Appl. Sci. Manuf.*, vol. 40, no. 4, pp. 404–412, Apr. 2009.
- [28] Sicomin Epoxy Systems, *SR GreenPoxxy 56 Clear Epoxy Resin Technical Datasheet*, Sicomin, 2015.
- [29] One High Bio-Content Resin, *Super Sap One System Technical Data Sheet*, Entropy Resins, 2015.
- [30] Ecopoxy, *Ecopoxy Resin and Clear Hardener Technical Data Sheet*, Ecopoxy, 2016.
- [31] M. Feldmann and A. K. Bledzki, “Bio-based polyamides reinforced with cellulosic fibres – Processing and properties,” *Compos. Sci. Technol.*, vol. 100, pp. 113–120, Aug. 2014.
- [32] A. Espert, F. Vilaplana, and S. Karlsson, “Comparison of water absorption in natural cellulosic fibres from wood and one-year crops in polypropylene composites and its influence on

their mechanical properties,” *Compos. Part Appl. Sci. Manuf.*, vol. 35, no. 11, pp. 1267–1276, Nov. 2004.

[33] L. Yan, N. Chouw, and K. Jayaraman, “Effect of UV and water spraying on the mechanical properties of flax fabric reinforced polymer composites used for civil engineering applications,” *Mater. Des.*, vol. 71, pp. 17–25, Apr. 2015.

[34] C. S. Korach and F.-P. Chiang, “Characterization of carbon fiber-vinylester composites exposed to combined uv radiation and salt spray,” *ECCM 2012 - Compos. Venice Proc. 15th Eur. Conf. Compos. Mater.*, Jan. 2012.

[35] J. Sousa, J. R. Correia, S. Cabral-Fonseca, “Durability of Glass Fibre Reinforced Polymer Pultruded Profiles: Comparison Between QUV Accelerated Exposure and Natural Weathering in a Mediterranean Climate,” *Experimental Techniques*, February 2016.

[36] B. G. Kumar, R. P. Singh, and T. Nakamura, “Degradation of Carbon Fiber-Reinforced Epoxy Composites by Ultraviolet Radiation and Condensation,” *J. Compos. Mater.*, vol. 36, no. 24, pp. 2713–2733, Dec. 2002.

[37] A. U. R. Shah, M. N. Prabhakar, and J.-I. Song, “Current advances in the fire retardancy of natural fiber and bio-based composites – A review,” *Int. J. Precis. Eng. Manuf. - Green Technol.*, vol. 4, no. 2, pp. 247–262, 2017.

[38] K. A. Salmeia et al., “Flammability of Cellulose-Based Fibers and the Effect of Structure of Phosphorus Compounds on Their Flame Retardancy,” *Polymers*, vol. 8, no. 8, p. 293, Aug. 2016.

[39] N. K. Kim, S. Dutta, and D. Bhattacharyya, “A review of flammability of natural fibre reinforced polymeric composites,” *Compos. Sci. Technol.*, vol. 162, pp. 64–78, Jul. 2018.

[40] M. Kamaya, A. Nakai, E. Fukui, and H. Hamada, “Micro-braided yarn as intermediate material system for continuous fiber reinforced thermoplastic composite,” *13th International Conference on Composite Materials*, August 2001.

[41] O. Faruk, A. K. Bledzki, H.-P. Fink, and M. Sain, “Biocomposites reinforced with natural fibers: 2000–2010,” *Prog. Polym. Sci.*, vol. 37, no. 11, pp. 1552–1596, Nov. 2012.

[42] T. Huber et al., “Three-dimensional braiding of continuous regenerated cellulose fibres,” *J. Ind. Text.*, vol. 45, no. 5, pp. 707–715, 2016.

[43] I. I. Qamhia, S. S. Shams, and R. F. El-Hajjar, “Quasi-Isotropic Triaxially Braided Cellulose-Reinforced Composites,” *Mech. Adv. Mater. Struct.*, vol. 22, no. 12, pp. 988–995, Dec. 2015.

[44] M. M. Kabir, H. Wang, K. T. Lau, and F. Cardona, “Chemical treatments on plant-based natural fibre reinforced polymer composites: An overview,” *Compos. Part B Eng.*, vol. 43, no. 7, pp. 2883–2892, Oct. 2012.

[45] L. Yan, N. Chouw, and K. Jayaraman, “Flax fibre and its composites – A review,” *Compos. Part B Eng.*, vol. 56, pp. 296–317, Jan. 2014.

- [46] G. Lebrun, A. Couture, and L. Laperrière, “Tensile and impregnation behavior of unidirectional hemp/paper/epoxy and flax/paper/epoxy composites,” *Compos. Struct.*, vol. 103, pp. 151–160, 2013.
- [47] E. Ameri, L. Laperrière, and G. Lebrun, “Mechanical characterization and optimization of a new unidirectional flax/paper/epoxy composite,” *Compos. Part B Eng.*, vol. 97, pp. 282–291, 2016.
- [48] N. Soykeabkaew, N. Arimoto, T. Nishino, and T. Peijs, “All-cellulose composites by surface selective dissolution of aligned ligno-cellulosic fibres,” *Compos. Sci. Technol.*, vol. 68, no. 10–11, pp. 2201–2207, Aug. 2008.
- [49] S. Kalka, T. Huber, J. Steinberg, K. Baronian, J. Müssig, and M. P. Staiger, “Biodegradability of all-cellulose composite laminates,” *Compos. Part Appl. Sci. Manuf.*, vol. 59, pp. 37–44, 2014.
- [50] J. W. Dormanns, J. Schuermann, J. Müssig, B. J. C. Duchemin, and M. P. Staiger, “Solvent infusion processing of all-cellulose composite laminates using an aqueous NaOH/urea solvent system,” *Compos. Part Appl. Sci. Manuf.*, vol. 82, pp. 130–140, Mar. 2016.
- [51] X. Chen, J. Chen, T. You, K. Wang, and F. Xu, “Effects of polymorphs on dissolution of cellulose in NaOH/urea aqueous solution,” *Carbohydr. Polym.*, vol. 125, pp. 85–91, Jul. 2015.
- [52] T. Nishino, I. Matsuda, and K. Hirao, “All-cellulose composite,” *Macromolecules*, vol. 37, no. 20, pp. 7683–7687, 2004.

Chapter 3 Sample Preparation and Quality Control Evaluation of Natural Fiber and Bio-Matrix Braided Composites

A version of this chapter has been submitted for publishing to *Composite Structures* as: Bruni-Bossio, B. M., Melenka, G. W., Ayranci C., and Carey, J. P., “Micro-Computed Tomography Analysis of Natural Fiber and Bio-Matrix Tubular Braided Composites.”

3.1 Introduction

Many different types of naturally occurring, plant based, fibers such as hemp, flax, jute, etc. have been studied and tested as reinforcing fibers [1–3]. Fibers derived directly from plants often have a large variability in mechanical properties. Bio-based fiber performance is dependent on many different factors, such as the growth process, region of the crop, time of harvest [4] Additionally, the same type of plant may have differing amounts of its constituents such as cellulose and lignin, sulfur content, ash content, and the like [2]. In recent years, the growing demand from the composites industry forced the producers of these fibers to increase their quality and consistency. This allowed an increase in the research that is conducted using them as constituents in composite materials. Among these fibers, cellulosic fibers carry a particular importance as they can be produced in long and continuous forms so that they can to be used in automated preform forming technologies such as braiding and filament winding.

Unlike the natural fibers, the number of bio-based resins that are available for commercial purchase is still limited [5]. Currently, only a handful of partially bio-based resins are commercially available including GreenPoxy 56, an epoxy resin containing 56% plant-based ingredients, [6] Supersap, an epoxy resin containing 30% bio-based ingredients [7], and Ecopoxy, an epoxy resin containing 25% natural ingredients [8].

For small batch production, braided composites are typically fabricated by first manufacturing the braided preform with dry fibers and then manually applying a resin to impregnate/wet the preforms. Depending on the resin type, braided composites may be cured at room temperature in open atmosphere, or with the assistance of an oven, an autoclave, or vacuum bags [9]. This study examines the manufacturing of cellulose fiber reinforced bio-based braided composites with manual impregnation, both with and without the vacuum bagging. Vacuum bagging is used in fabrication to create a pressure differential between the composite and surrounding atmosphere, allowing atmospheric pressure to help consolidate the composite and eliminate air bubbles [10].

Due to the complex geometry of braided composite materials, it can be difficult to ensure uniform impregnation of the resin into the fibers. In production of composite materials, it is crucial to establish a quality wetting of the fibers to minimize the voids in the composite and to promote good adhesion between the fibers and matrix. The studies that investigated the properties of composites manufactured with natural fibers and a bio-based matrix have identified issues with the interfacial strength between the yarns and matrix [10]. A poor bond between fiber and matrix also reduces wettability of the fibers, increasing the likelihood of imperfections/voids in the composite. The presence of voids has been shown to affect the strength of the overall composite [11].

Characterization of the post-production geometry and porosity of braided composite samples comprised of natural based materials is a critical step to ensure their future viability. In this study, high-resolution micro-computed tomography (μ CT) imaging was used to both visually observe the ability of the resin to impregnate the fibers and utilize image segmentation methods to numerically determine the fiber volume fraction and void content [12].

Both void content and fiber volume fraction are critical parameters in defining the micromechanics of composite materials [13]. There are several other methods used to observe void characterization

in composite materials, such as matrix burn-off, acid digestion and SEM (Scanning Electron Microscopy). However, burn-off and digestion methods do not provide information on void shape or distribution, and SEM methods only provide the characteristics at a particular location. Little *et al.* [14] compared different void characterization techniques, and found μ CT imaging to be the most precise and reliable method for composite materials. μ CT imaging methods have been used in other studies to accurately determine the content of porosity [14-18], and fiber volume fraction [19] of conventional composite materials.

The aim of this work is to study the volume and distribution of imperfections of tubular braided composites made of cellulose yarns and bio-based resin. This study is the first to examine the effect of braid angle, type of resin and curing method on the porosity of natural fiber/bio-based braided composites.

3.2 Methods

3.2.1 Materials

In this study, two different braided composite materials were produced. In each case, the reinforcement used was a continuous 100% cellulose fiber yarn (BioMid®, 1650 Denier, Shank Consulting, ENC International Corporation, Seoul, Korea) composed of by-products from the lumber industry. BioMid® is derived by separating the cellulose molecules, dissolving into a pulp and pumping the cellulose through a spinneret to produce a continuous fiber [6]. Due to this processing method of separating and aligning the cellulose fibrils to create a yarn, BioMid® provides consistent mechanical properties similar to those of synthetic yarns. In addition, since they are produced from lumber waste, they do not require additional water/fertilizer for the plant growth. According to Shank Consulting, BioMid® only generates 0.88 kg of CO₂ emissions per metric ton

of fiber produced, in comparison to glass fibers which generates 500-600 kg per metric ton of fiber produced [20].

Two different bio-based resins were used to prepare the braided composites to examine the effect of resin type on the void content. The first resin was a commercial epoxy that is 25% based of natural ingredients such as eggshells and soybeans (Ecopoxy Resin & Clear Hardener, Ecopoxy, Morris, MB). The second resin was hemp-based, derived by a lipids research group at the University of Alberta (Lipid Chemistry Group, University of Alberta). The hemp resin was derived from epoxidized hemp oil (EHO), using Trimellitic anhydride (TMA) as a curing agent [21], [22].

3.2.2 Sample Preparation

To prepare the samples, the yarns were first braided into tubular preforms using a Maypole braiding machine (K80-72, Steeger USA, Inman, South Carolina, USA) shown in Figure 3-1.

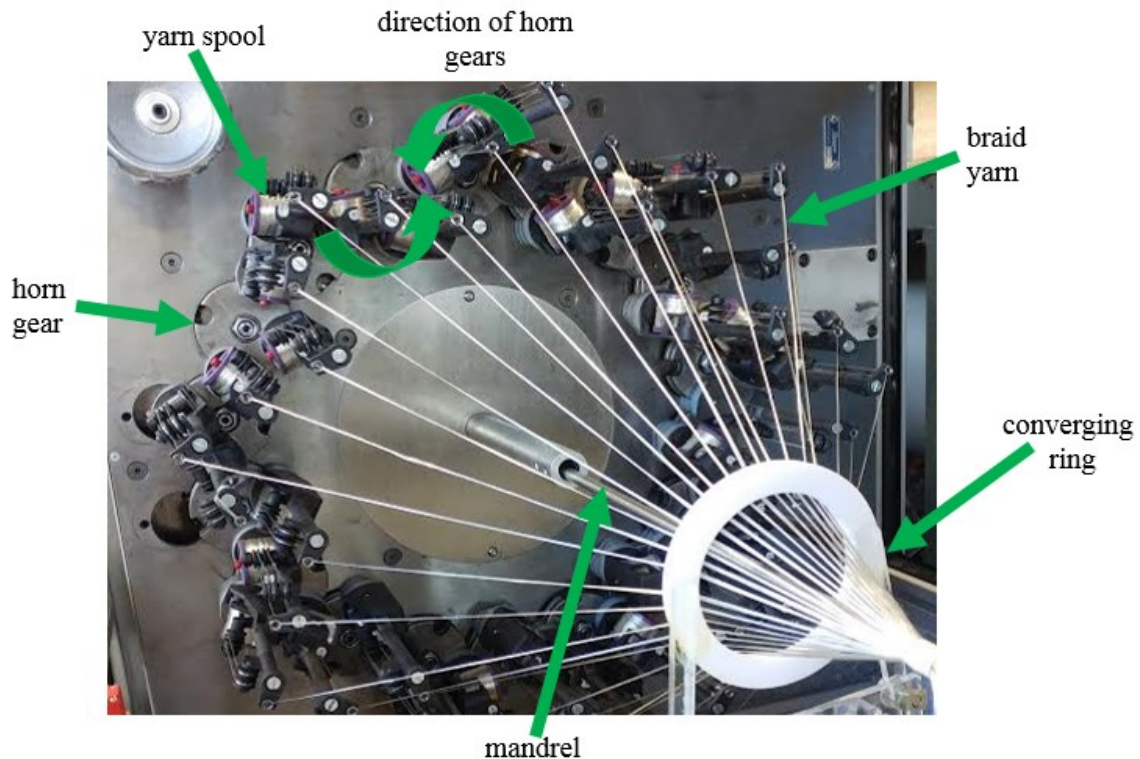


Figure 3-1. Maypole braiding machine and components

The machine operates with loaded yarns attached to horn gears which braid around the tubular mandrel. As the carriers rotate and braid, the mandrel is pulled forward by a pneumatically operated belt system. An overview of this operation can be seen in Figure 3-2.

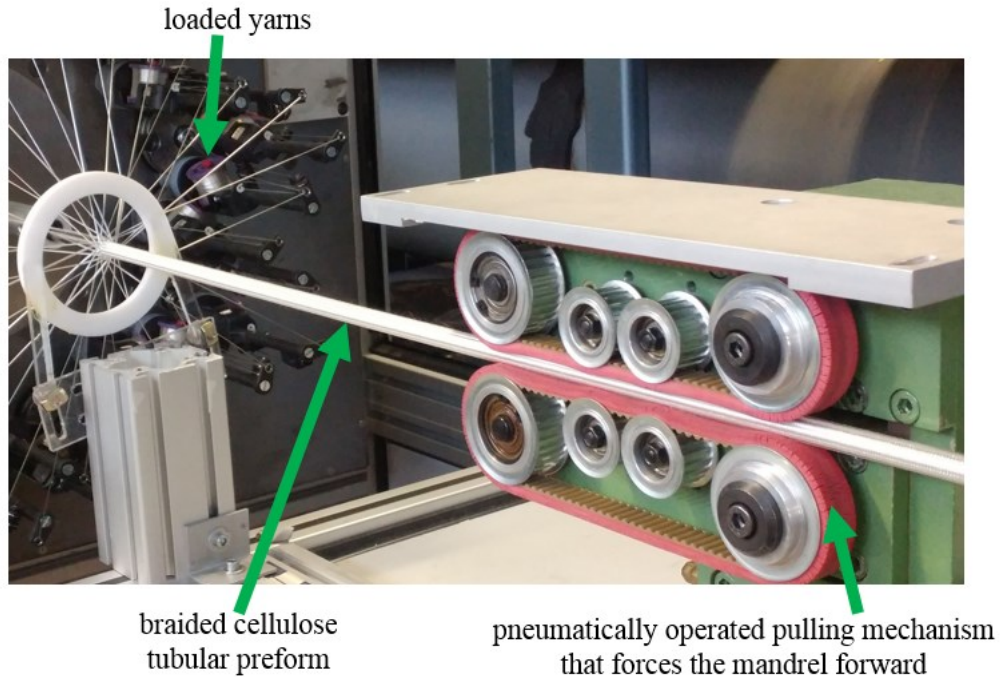


Figure 3-2. Braiding head and take-up mechanisms used to manufacture the tubular braided preform

There are several key parameters that are used to define the architecture of the braided composite, which are illustrated in Figure 3-3. The braid angle (θ) is the angle between the yarn direction and longitudinal axis, the inner diameter (ID) is the diameter of the inside of the tube, and the outer diameter (OD) is the diameter of the outside of the tube. The unit cell is defined as the smallest unit that repeats over the entire structure [23].

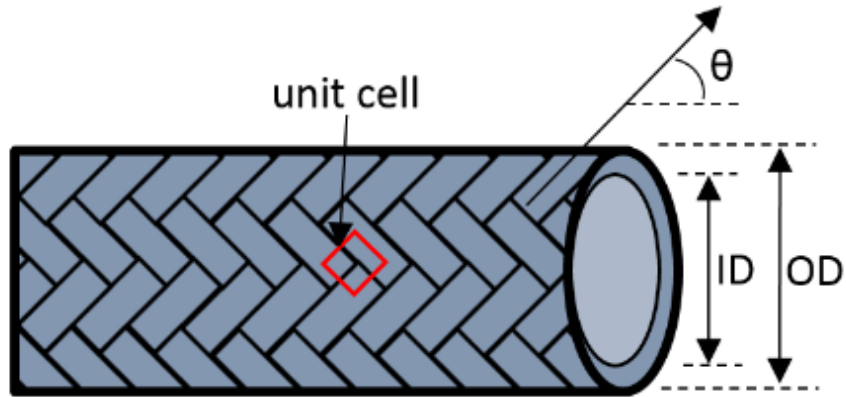


Figure 3-3. Illustration of a regular braid with key parameters used to define its architecture

Modifying the above parameters effects the mechanical properties of the braids [24]. Altering braid angle in particular can significantly change the braid's mechanical properties [25]. Therefore, braided composites were prepared at three varying braid angles, as shown in Figure 3-4, to evaluate the effect of braid angle on the void volume and distribution.

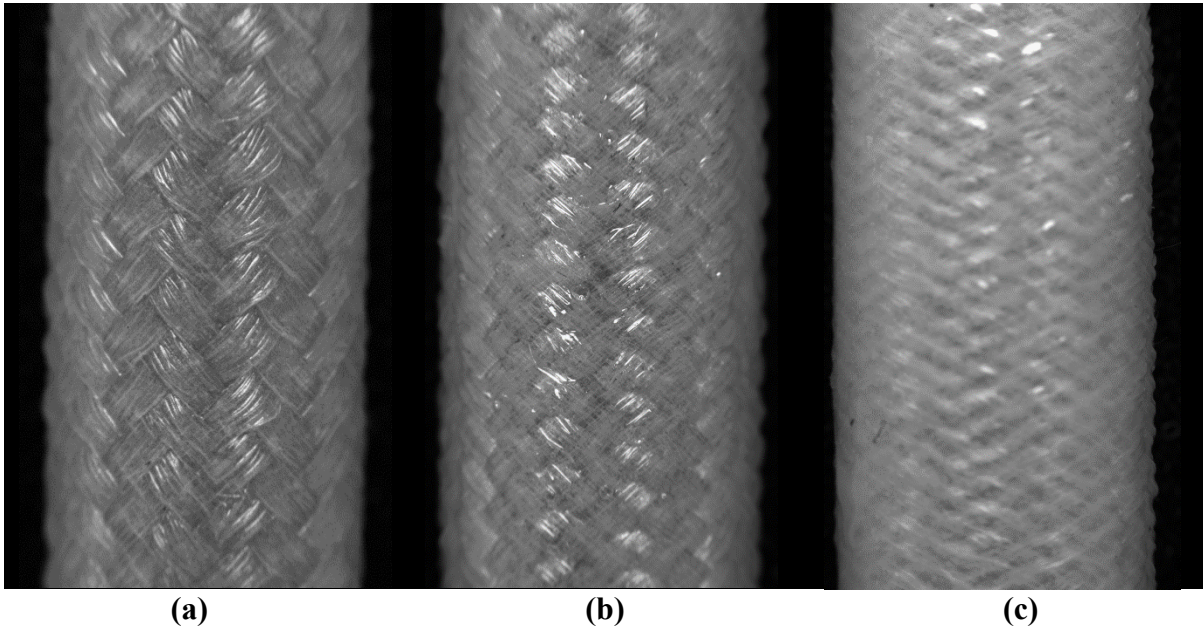


Figure 3-4. Regular cured braids at three braid angles (a) 40°, (b) 50°, and (c) 60°, all cured without vacuum bagging with Ecopoxy resin

This was achieved by modifying the speed of the take-up mechanism that advances the mandrel forward as the carriers braid the yarns. The calculation to determine the settings required on the Maypole braiding machine to manufacture the braids at the desired angles is shown in Appendix A.

The braided preforms were placed over a polytetrafluoroethylene (PTFE) mandrel and impregnated with resin using a hand lay-up method. As per the manufacturer's specifications, the braids coated in Ecopoxy resin were fully cured at room temperature for 48 hours. To examine the effect of vacuum bagging on the porosity, the Ecopoxy samples were cured both within a vacuum system and in the open atmosphere. For the vacuum system, the braid samples were coated in resin and cured within the vacuum bagging system illustrated in Figure 3-5. The vacuum bag (Econolon, Airtech International Inc., Huntington Beach, California) was held air tight with sealant tape (AT-200Y, Airtech International Inc., Huntington Beach, California) and attached to the vacuum pump (Series 212-160, Airtech International Inc, Huntington Beach, California) with a series of hoses and vacuum connections. Infusion mesh (Greenflow 75, Airtech International Inc., Huntington Beach, California) was placed within the vacuum bag to distribute the pressure and breather fabric (Dahlar® Release Bag 125, Airtech International Inc., Huntington Beach, California) was wrapped around the braid sample to prevent the resin from adhering to the infusion mesh.

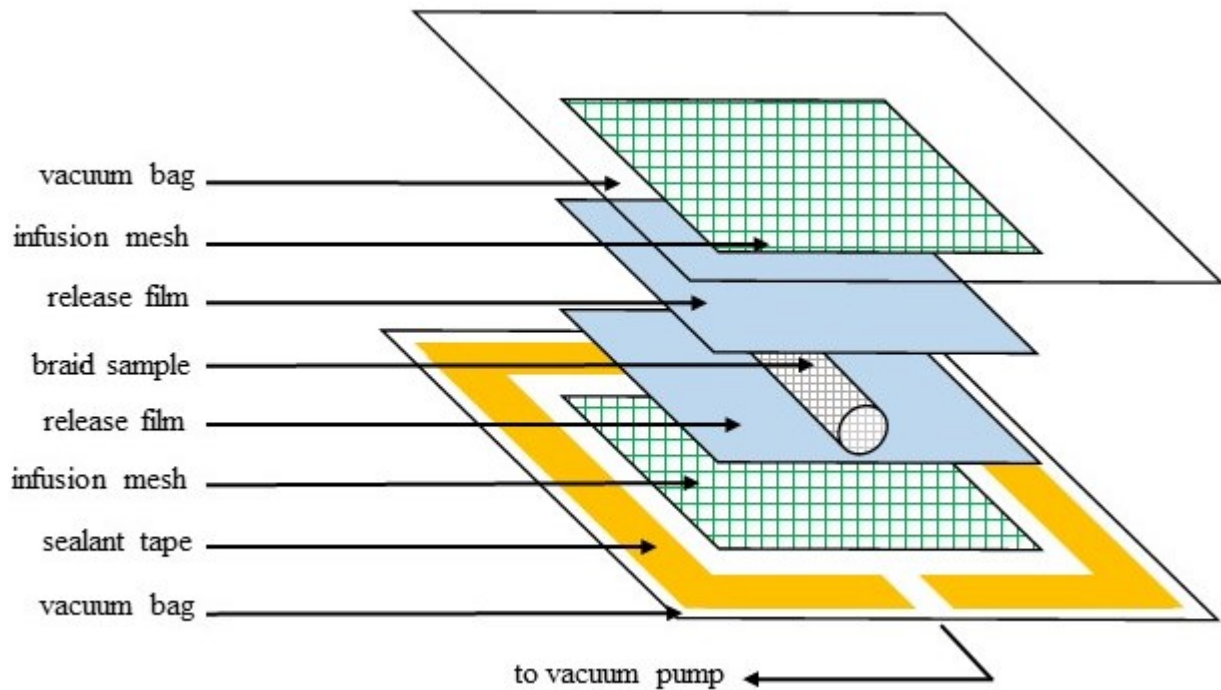


Figure 3-5. Schematic describing system used to cure Ecopoxy samples within a vacuum

By modifying the braid angle, resin type and curing method (ie. vacuum bag or no vacuum bag), nine samples were produced, as described in Table 3-1. With these nine samples, the effect of curing methodology, type of resin, and braid angle on the braid geometry and microstructure could be investigated.

Table 3-1. Description of 9 scanned samples

Sample #	Desired Braid Angle (°)	Resin Type	Vacuum Bag (Y/N)
1	40	Ecopoxy	N
2	40	Ecopoxy	Y
3	40	Hemp Resin	N
4	50	Ecopoxy	N
5	50	Ecopoxy	Y
6	50	Hemp Resin	N
7	60	Ecopoxy	N
8	60	Ecopoxy	Y
9	60	Hemp Resin	N

3.2.3 Geometry Evaluation

The multiple steps required in the manufacturing process create opportunities for the yarns to shift before curing. As a result, precise control of the geometry, specifically braiding angle, can be difficult. Therefore, it was necessary to evaluate the final geometry of the braids to compare with the ideal braid geometry and evaluate the consistency of the braiding process. The reconstructed cross-sections were used to measure the inner and outer diameter of the samples. A micrometer (3732XFL-1 Electronic Micrometer, Starrett, Massachusetts) was also used to measure the outer diameter (OD) of the samples and a telescoping gauge (8–12.7mm Telescopic Gauge, Moore and Wright, Sheffield, England) along with the micrometer was used to measure the inner braid diameter (ID) to compare with the imaging results. The braid angle was measured from the radiograph images using ImageJ software. The samples were measured in diameter and braid angle in five locations along each braid to ensure validity in the measurement results.

3.2.4 μ CT Imaging

3.2.4.1 Scanning

To examine the microstructural characterization of the braids, all samples were scanned under a high-resolution μ CT machine (SkyScan 1272 Microtomograph, Bruker-MicroCT, Kontich, Belgium) as shown in Figure 3-6. For each of the nine samples, a 3-inch sample was positioned in the scanning chamber and rotated 180° to obtain radiographs of the braid samples. The parameters used to scan the nine samples are described in

Table 3-2.

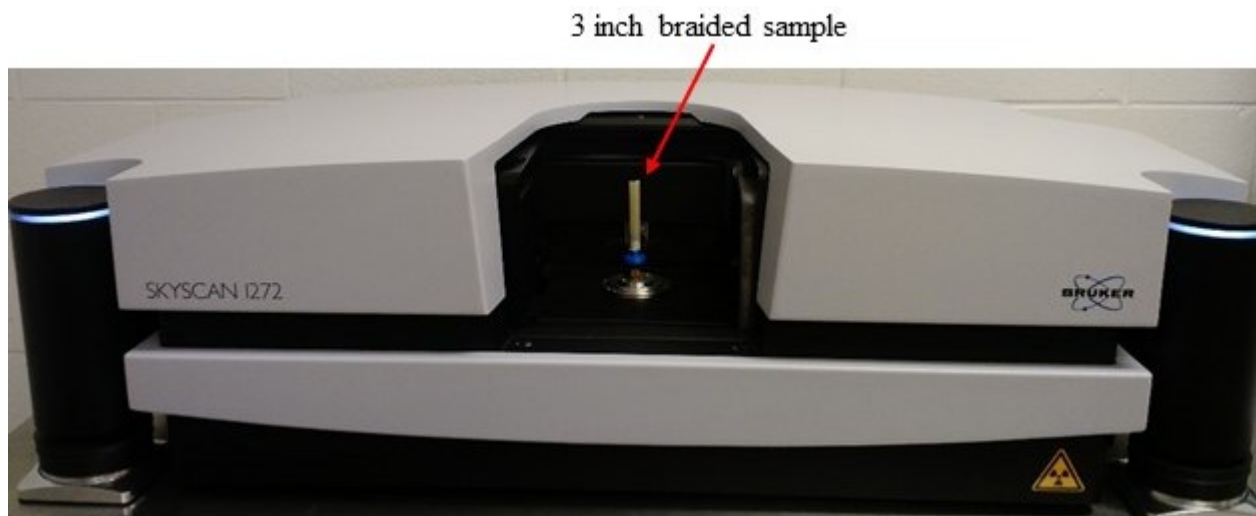


Figure 3-6. Experimental setup of u-CT scanner with braided sample inside

Table 3-2. Settings used in u-CT scan

Parameter	Value
X-ray voltage	40 kV
X-ray current	200 μ A
Scan resolution	5.4 μ m
Rotation	180°
Rotation steps	0.3°
Filters used	none
Frame averaging	2

The settings shown in Table 2 were chosen to optimize contrast in the final braid cross-sectional images. Decreasing the X-ray energy could allow for greater absorption and clearer distinction between features; but would also introduce noise into the image. Increasing the X-ray energy could reduce noise, but result in a saturated image making it difficult to observe sample features. A smaller rotation step would increase image resolution but would also increase data set size and scan time. A 52% partial width scan was utilized to reduce the collected image data. This reduced the collected braid image size from 4904x3280 pixels to 2550x3280 pixels. The scan time for each sample was approximately 45 minutes, resulting in approximately 600 radiograph images for each braid sample

3.2.4.2 Reconstruction

The radiograph images were loaded into reconstruction software (NRECON 1.7.1.0, Bruker, Belgium) to obtain a series of cross-sectional images of the braided composite. The cross-sectional images reconstructed from the radiograph are perpendicular to one another [26]. For each sample, cross-sectional images were generated for a length containing five braid unit cells to ensure accurate representation of the full braid sample while minimizing the size of collected data, resulting in around 1500 images for each sample. All cross-sectional images were exported as 8-bit bitmap (BMP) images with a pixel size of 5.4 μm . An example of a single radiograph image obtained from the μCT scan is shown in Figure 3-7(a) and the reconstructed cross-sectional image at a certain length (at location of the red line) is shown in Figure 3-7(b).

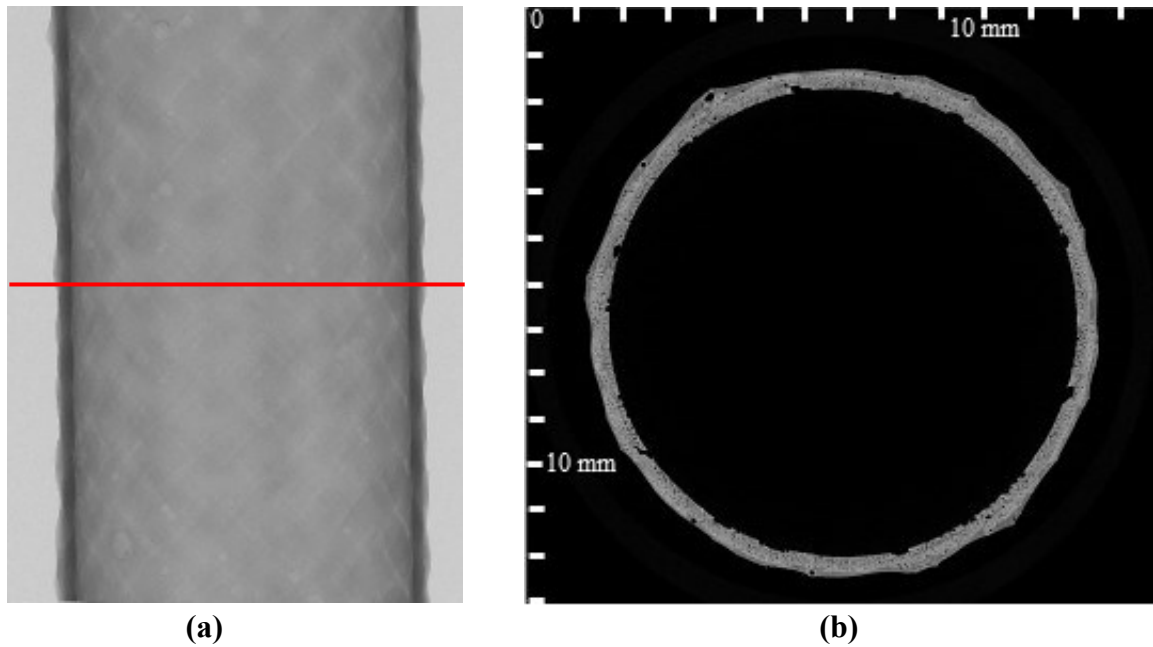
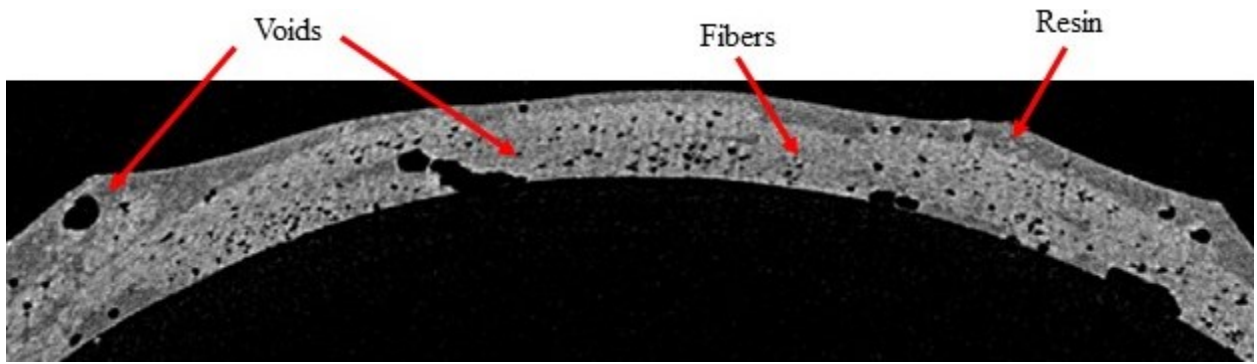


Figure 3-7. (a) Shadow projection image produced from the x-ray scans with red line indicating particular image cross-section location (b) a sample cross sectional image created using reconstruction software with scale to demonstrate size

3.2.4.3 Binary Segmentation

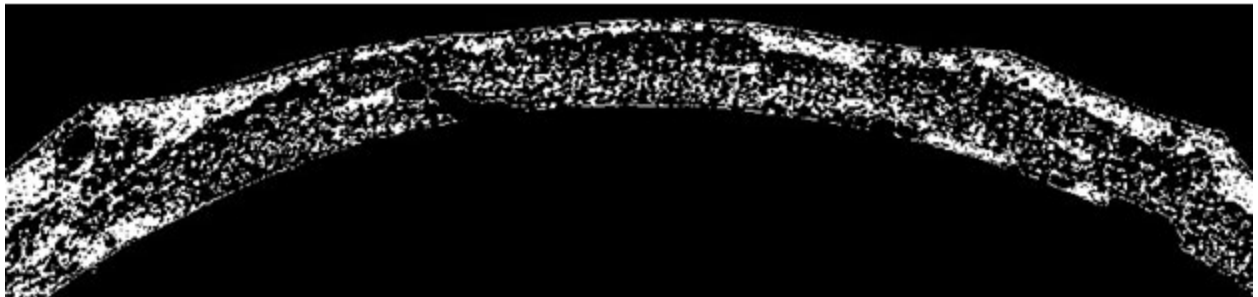
Once the greyscale cross-sectional images were reconstructed, segmentation of the collected braid cross-sectional images was performed using an image analysis and visualization software package (CTan 1.16.90, Bruker microCT, Belgium). Binary segmentation of the greyscale values in the image was used to separate the yarns, fibers and voids present within each cross-section. Figure 3-8 shows a sample portion of a cross-section compared with its segmentation of the fibers, resin and voids. Figure 6 (a) shows the original greyscale image of the reconstructed cross-section, while Figures 6 (b) to (c) show the segmentations of voids, resin and fibers, respectively.



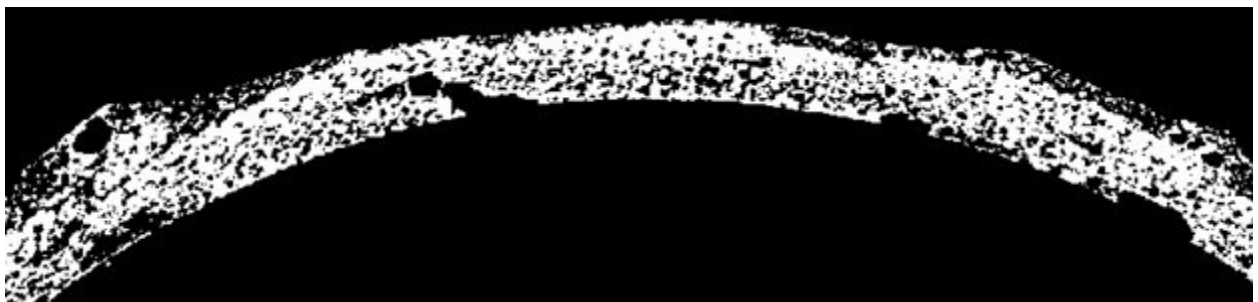
(a)



(b)



(c)



(d)

Figure 3-8. Example braid structure segmentation analysis (a) original braid sample reconstructed cross-section image and the results of segmentation of its (b) voids (c) fibers, and (d) resin

Due to the difference in material densities, a variation in the greyscale values of the fibers and resin rich regions can be observed, allowing segmentation to be possible. A summary of the process used to determine the fiber volume content from the above images is described in Figure 3-9. This process was done separately for all nine samples. Noise in the image can occur due to a low number of photons being present at a certain location [27]. An increase in X-ray energy can decrease the statistical probability of a low photon count, resulting in the reduction of noise. However, as mentioned earlier, this could also decrease the image resolution. Therefore, de-speckle filtering was used to remove unwanted noise in the image. In addition, a morphological erosion procedure was used to remove a thin outer ring that was created along the perimeter of the braid due to the reflectivity of the resin.

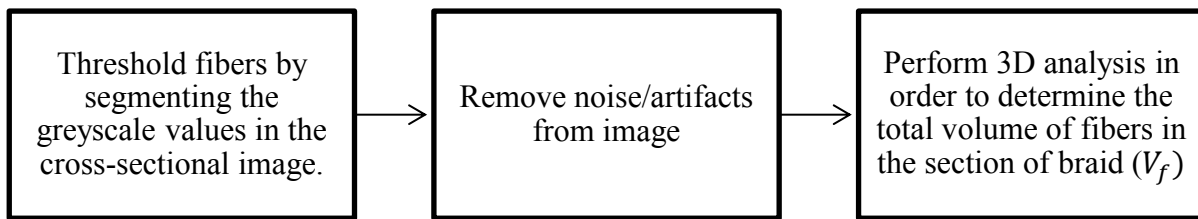


Figure 3-9. Flow chart describing process using binary segmentation to determine the fiber volume content of each braid sample

To determine the resin volume content (V_m), the process shown in Figure 3-9 was repeated for all nine samples by segmenting the range of greyscale values corresponding to the resin range in the image. Since the voids match the surrounding space, additional steps were required to segment only the voids present within the cross-section. A summary of the process used to determine void volume content is shown in Figure 3-10.

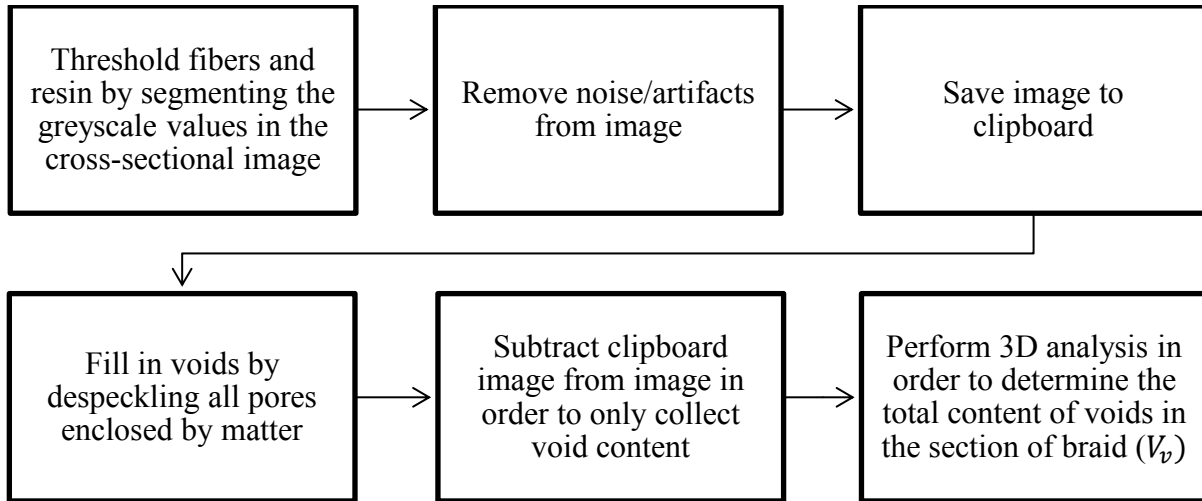


Figure 3-10. Flow chart describing process using binary segmentation to determine void content of braid sample

Once the total volume content of voids (V_v), fibers (V_f) and matrix (V_m), in the total section of scanned braid were determined, the fiber volume fraction (v_f) the matrix volume fraction (v_m) and void content fraction (v_v) of the samples were determined by 3.1, 3.2 and 3.3 respectively [13].

$$v_f = \frac{V_f}{V_m + V_f + V_v} \quad (3.1)$$

$$v_m = \frac{V_m}{V_m + V_f + V_v} \quad (3.2)$$

$$v_v = \frac{V_v}{V_m + V_f + V_v} \quad (3.3)$$

The image segmentation data for each sample was also converted to an STL file for the fibers, resin and voids separately. The STL files were imported in a visualization software (Paraview 5.5.0, Sandia National Laboratories, New Mexico) to visualize the voids in three dimensions and spatially examine their shape, location and distribution.

3.3 Results and Discussion

3.3.1 Geometry Measurement

The results for the measurements of all samples can be seen in Table 4-3 for braid angles and Table 4-4 for diameters. The procedures used for measurement can be seen in Section 3.2 above.

The maximum spread from desired to measured braid angle was 1.55° , corresponding to a 3.80% difference. Chen *et al.* [25] found that the braid angle from this manufacturing technique could be controlled within $\pm 3^\circ$. Therefore, these results are in the realm of what is reasonable achieved with this type of fabrication. The diameter measurements from each method were in close agreement, with the maximum percentage difference being 1.98%. These results demonstrate that μ CT imaging is an accurate method to perform geometry measurements.

Table 3-3. The braid angle measurements for all 9 samples measured from the radiograph images with ImageJ software compared with the desired braid angle.

Sample #	θ , desired ($^\circ$)	θ , measured ($^\circ$)	% Diff.
1	40	41.49 \pm 1.01	3.66
2	40	41.55 \pm 1.05	3.80
3	40	40.11 \pm 2.20	0.27
4	50	51.38 \pm 0.71	2.72
5	50	50.31 \pm 1.69	0.62
6	50	51.14 \pm 1.54	2.25
7	60	59.3 \pm 0.81	1.17
8	60	60.1 \pm 1.37	0.17
9	60	59.69 \pm 1.44	0.52

Table 3-4. The diameter measurements for all 9 sample made both from the cross-sectional images in CTAn and physically with a micrometer.

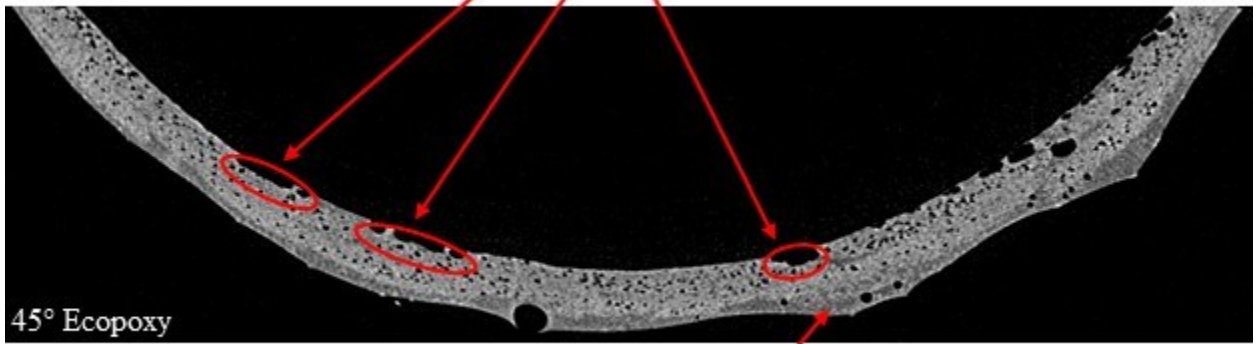
Sample #	ID (mm)			OD (mm)		
	CTAn	Physical	% Diff.	CTAn	Physical	% Diff.
1	10.01±0.05	10.18±0.05	1.68	11.25±0.07	11.22±0.07	0.23
2	10.08±0.06	10.11±0.06	0.31	11.23±0.02	11.01±0.11	1.98
3	9.97±0.04	10.06±0.13	0.91	10.99±0.04	11±0.13	0.13
4	10.09±0.06	10.12±0.06	0.33	11.10±0.06	11±0.09	0.88
5	10.13±0.06	10.18±0.03	0.41	11.22±0.08	11.16±0.07	0.58
6	9.92±0.02	9.98±0.08	0.62	11.12±0.06	11.08±0.11	0.37
7	9.71±0.05	9.68±0.03	0.33	10.84±0.09	10.92±0.05	0.70
8	10.01±0.04	9.97±0.06	0.43	11.11±0.07	11.04±0.10	0.57
9	10.04±0.04	9.98±0.11	0.51	11.1±0.05	11.22±0.10	1.13

From these results, it is possible to create consistently sized inner and outer diameters. Ensuring consistent braid angles seemed to be more challenging. It is likely that the braid angles shift when transferring the preforms from the braiding mandrel to the curing mandrel, producing some uncertainty in the final braid angle. However, Chen *et al.* [28] found that braid angle from this manufacturing technique could be controlled within $\pm 3^\circ$ and therefore the accuracy of braid angle is within the realm of what is expected for this type of fabrication.

3.3.2 Braid micro-structure

The nine samples were compared both visually and quantitatively using the cross-sections produced by the μ CT data. An image comparison of the cross-section for 50° BioMid® preforms cured under the three different methods can be seen in Figure 3-11. Inner pores can be seen along the inside diameter of the braid in Figure 9(a) and (b) for the non-vacuum bagged Ecopoxy and Hemp resin samples. By contrast, fewer open pores were observed for the vacuum-bagged sample shown in Figure 9 (c).

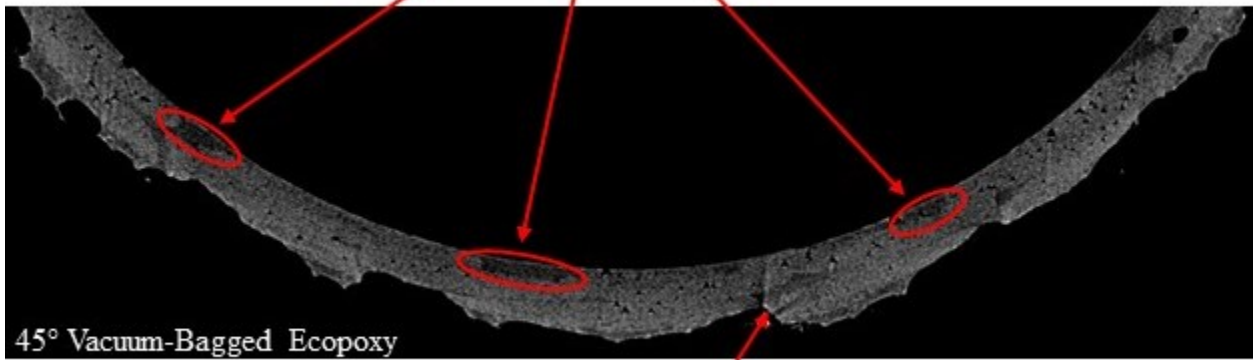
Empty locations along inner diameter where no resin was impregnated



Visible layer of resin sitting on outer diameter

(a)

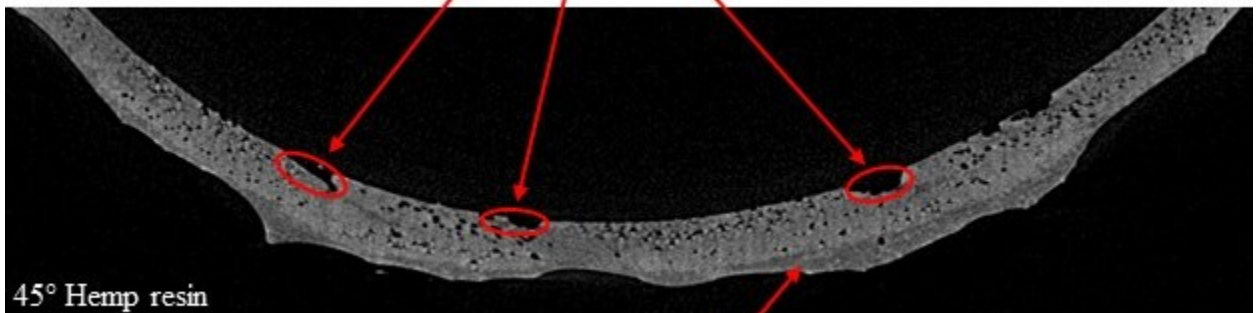
Resin impregnated into inner diameter



Thin layer of resin sitting on outer diameter

(b)

Empty locations along inner diameter where no resin was impregnated



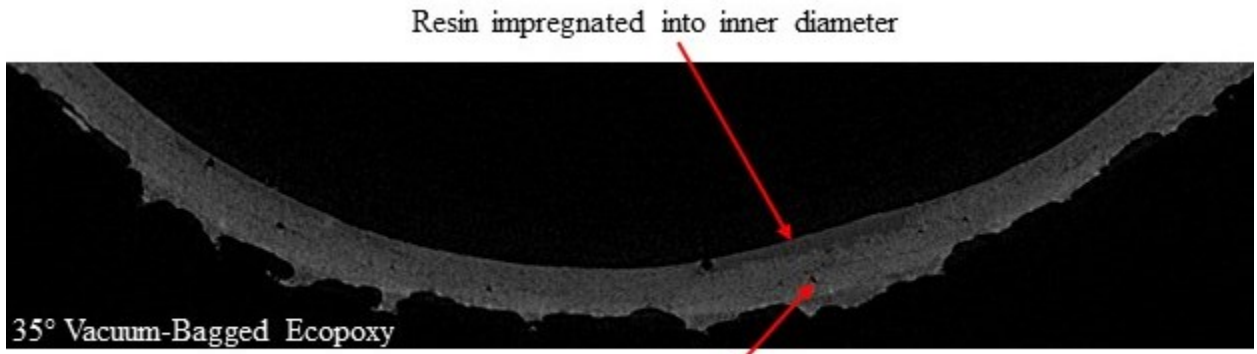
Visible layer of resin sitting on outer diameter

(c)

Figure 3-11. Visual comparison of the impregnation of resin in 50° preform samples under 3 different curing methods (a) hemp resin cured without vacuum bagging (b) Ecopoxy resin cured without vacuum bagging and (c) Ecopoxy resin cured with vacuum bagging

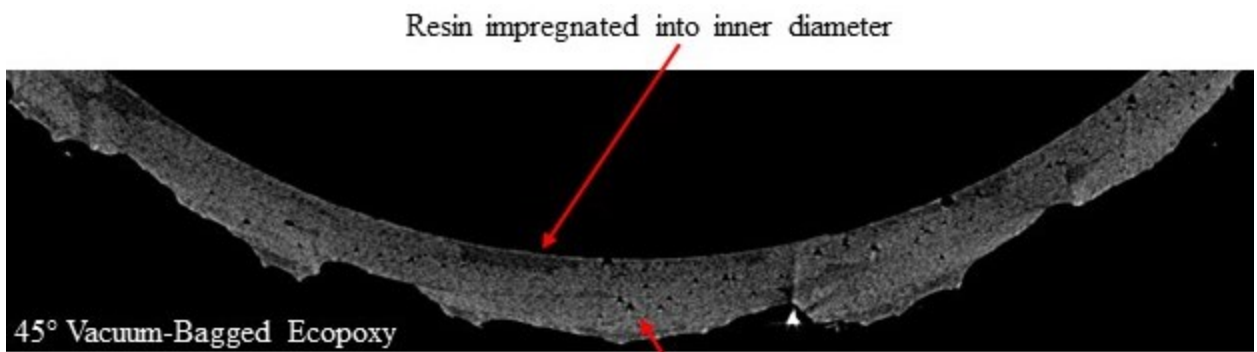
Comparing the cross-sections, it is clear that vacuum bagging did improve the resin's impregnation into the yarns as the entire cross section was covered in yarn or resin and there were fewer large voids. In addition, yarn compaction was improved, suggesting that vacuum bagging helps to consolidate the composite structure. It appears that the hemp and Ecopoxy resin cured without vacuum bagging did not impregnate the yarns as well since there is a large layer of resin along the outer perimeter of the braid. As well, large gaps along the inner diameter where resin was not able to penetrate can be seen.

An image comparison of the BioMid® preforms cured with Ecopoxy under the vacuum-bagging can be seen in Figure 3-12. A portion of a cross-section for the 40° vacuum-bagged sample is shown in Figure 3-12(a), for the 50° vacuum-bagged sample is shown in Figure 3-12(b), and for the 60° vacuum-bagged sample is shown in Figure 3-12(c). It appears that the vacuum bagging improved resin infusion as resin was able to impregnate the braids into the inner diameter for all three braid angles. There are fewer voids in the 40° braid compared to the 50° and 60° braids. This occurs because at larger braid angles the yarns are more compact, making it more difficult for the viscous resin to impregnate the fibers.



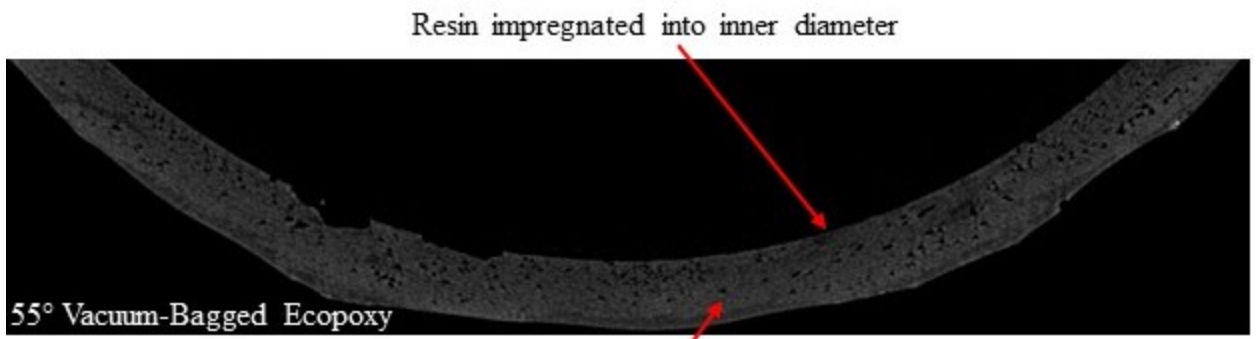
Few visible voids present

(a)



Increase in visible voids present from 35° sample

(b)



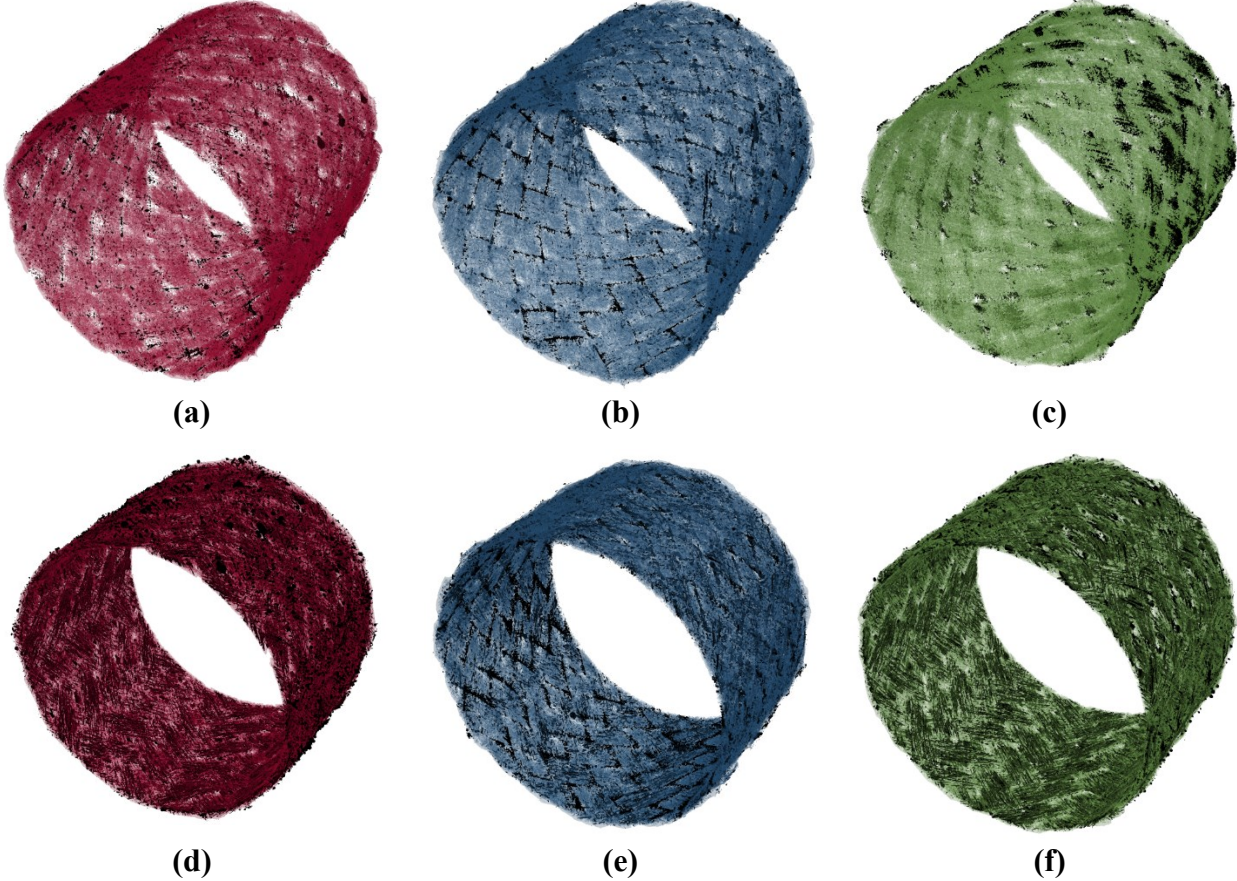
Increase in visible voids present from 35° and 45° braid angle

(c)

Figure 3-12. Visual comparison of the impregnation of Ecopoxy resin cured under vacuum bags for (a) 40° (b) 50° (c) 60°

The results from the segmentation of the yarns and voids as a solid model can be seen for all nine samples in Figure 3-13. Voids are shown in black and the different curing methods are indicated by colour according to the legend. Braid angle is labelled below each sample. A length containing five unit cells was selected to reduce file size while allowing an adequate representation of the entire braid structure. The fibers are shown at 30% transparency so that the inner voids can be more clearly visualized.

■ Voids ■ Ecopoxy ■ Vacuum-Bagged Ecopoxy ■ Hemp Resin



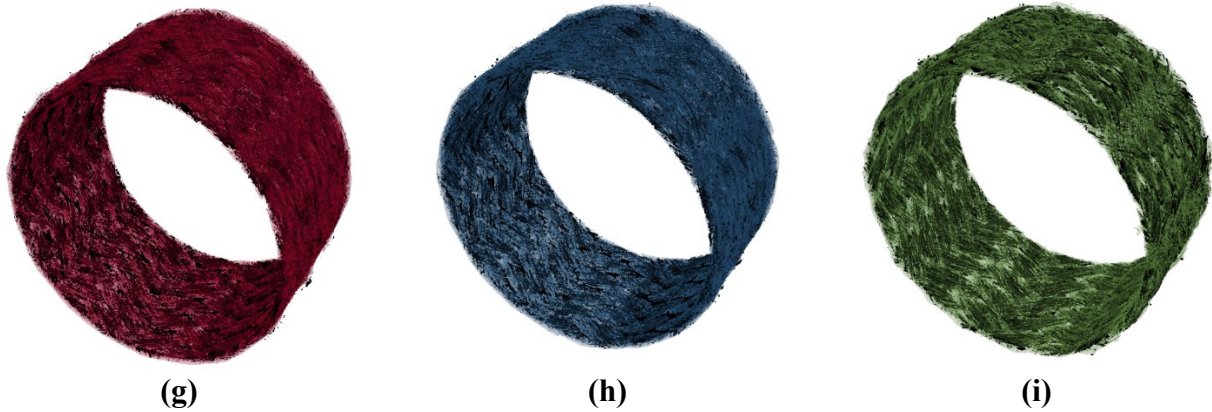


Figure 3-13. Solid models showing segmentation results for samples 1 to 9: (a) 40° Ecopoxy, (b) 40° Vacuum-Bagged Ecopoxy, (c) 40° hemp resin, (d) 50° Ecopoxy, (e) 50° Vacuum-Bagged Ecopoxy, (f) 50° hemp resin, (g) 60° Ecopoxy, (h) 60° Vacuum-Bagged Ecopoxy, and (i) 60° hemp resin. Voids are shown in black and fibers are shown in legend colours at 30% transparency. Resin is omitted for clarity.

The void location is significant when comparing between the nine samples in Figure 3-13. By examining the 40° braid samples, the voids in the hemp sample Figure 3-13 (a) are both more abundant and larger than the two braids cured with Ecopoxy Figure 3-13 [(b) and (c)]. In addition, at all three braid angles, the voids in the hemp samples [(a), (d) and (g)] seem to largely be located close to the outer perimeter of the braid which indicates that the hemp resin may not have impregnated the braids as well as the Ecopoxy resin. Inspecting the vacuum-bagged samples [(c), (f) and (i)], the voids are less sporadic and mainly located at the locations of yarn crossover. Therefore, vacuum bagging helped to control consistency of curing and reduce void content. Vacuum bagging also minimized void size. A section view of the voids in each sample is shown in Figure 3-14 in order to visualize the void pattern, shape and distribution more clearly. For the 40° braids, there are significantly fewer voids, and present voids are mostly circular and small. For the 50° and 60° braids, the total number of voids appear greater, and the voids are more rod-like in shape.

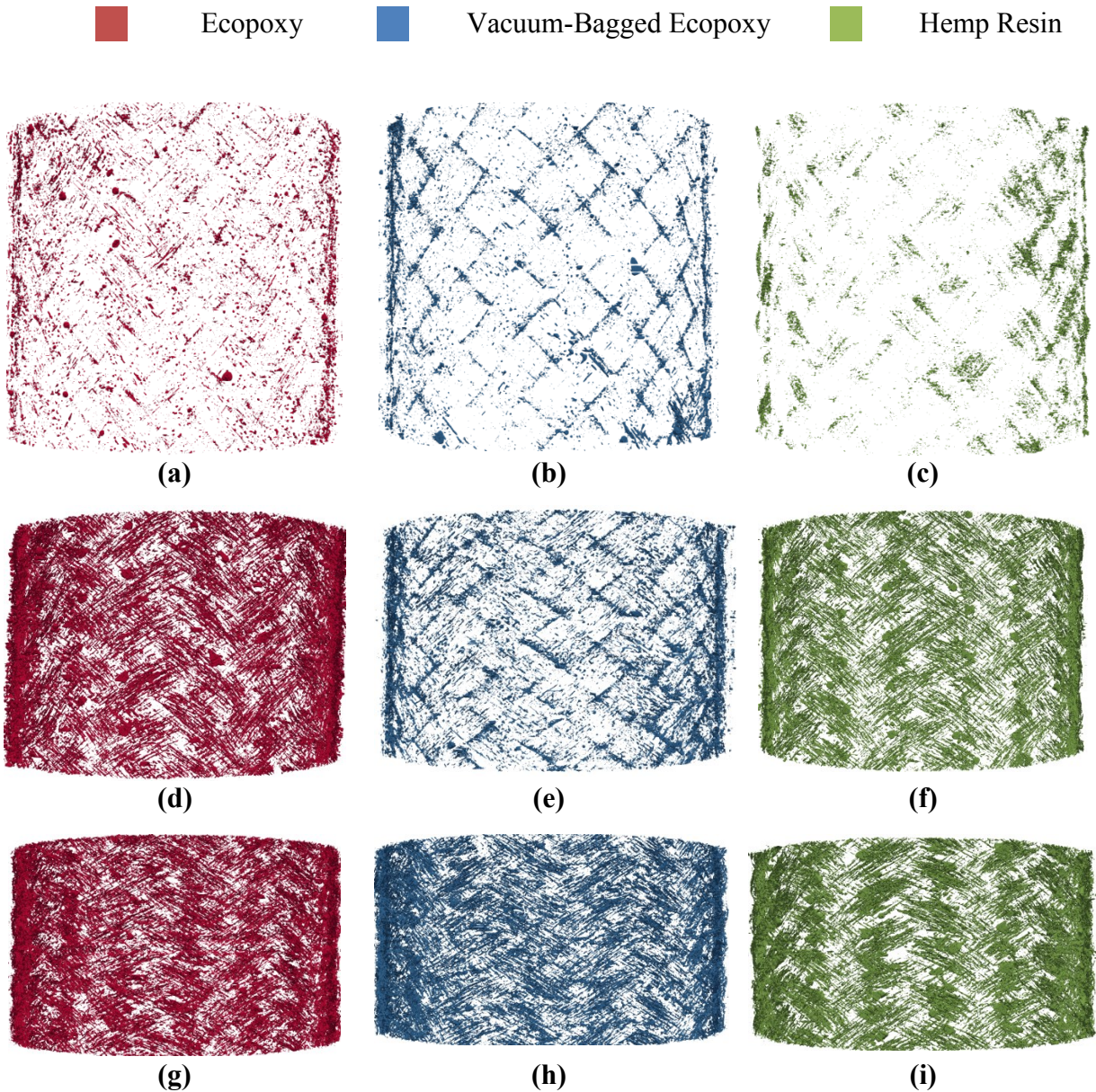


Figure 3-14. A sliced view of voids present in samples 1 to 9 respectively. (a) 40° hemp, (b) 40° Ecopoxy, (c) 40° Ecopoxy vacuum-bagged, (d) 50° hemp, (e) 50° Ecopoxy, (f) 50° Ecopoxy vacuum-bagged, (g) 60° hemp, (h) 60° Ecopoxy, (i) and 60° Ecopoxy vacuum-bagged.

The numerical values for the fiber volume fraction, matrix volume fraction, void volume content, and total number of enclosed voids are shown in the illustrated in the bar charts in Figure 3-15 and Figure 3-16. As shown in Figure 3-15, the fiber volume fraction ranged between 56% and 67% at the 50° braid angle. It would be expected that this value would be more consistent at each braid angle and increase as the braid angle is increased. However, the discrepancy in fiber volume

fraction was largely due to the difficulty in accurately applying consistent resin with hand lay-up. As seen in Figure 3-16, the values for the matrix fiber volume ranged between 28% and 45%.

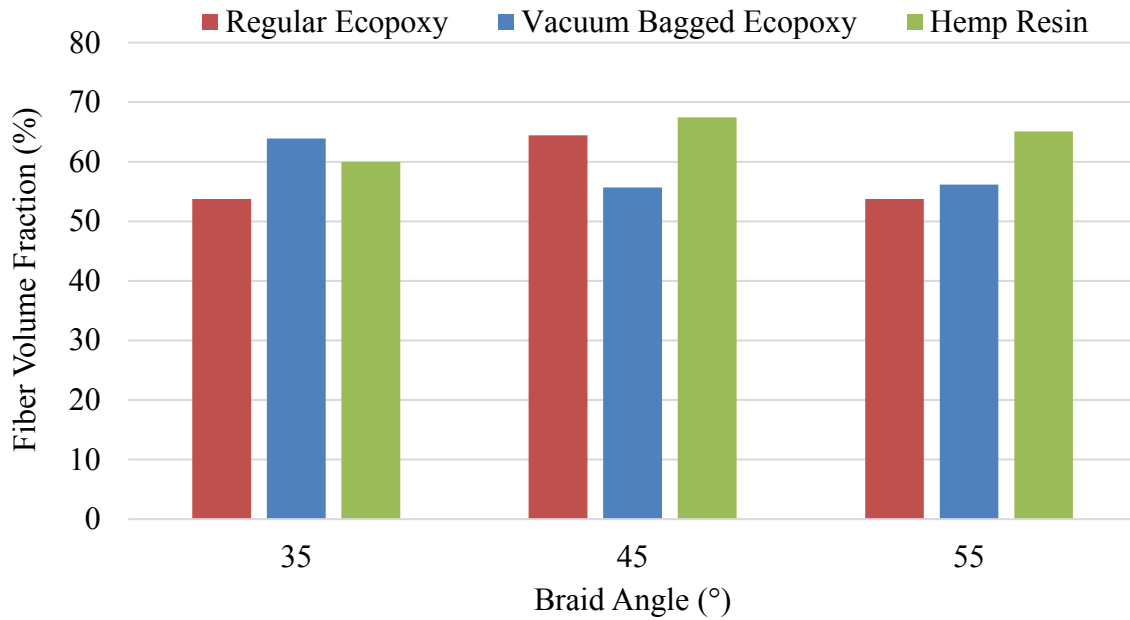


Figure 3-15. Fiber volume fraction for each sample calculated from μ CT results

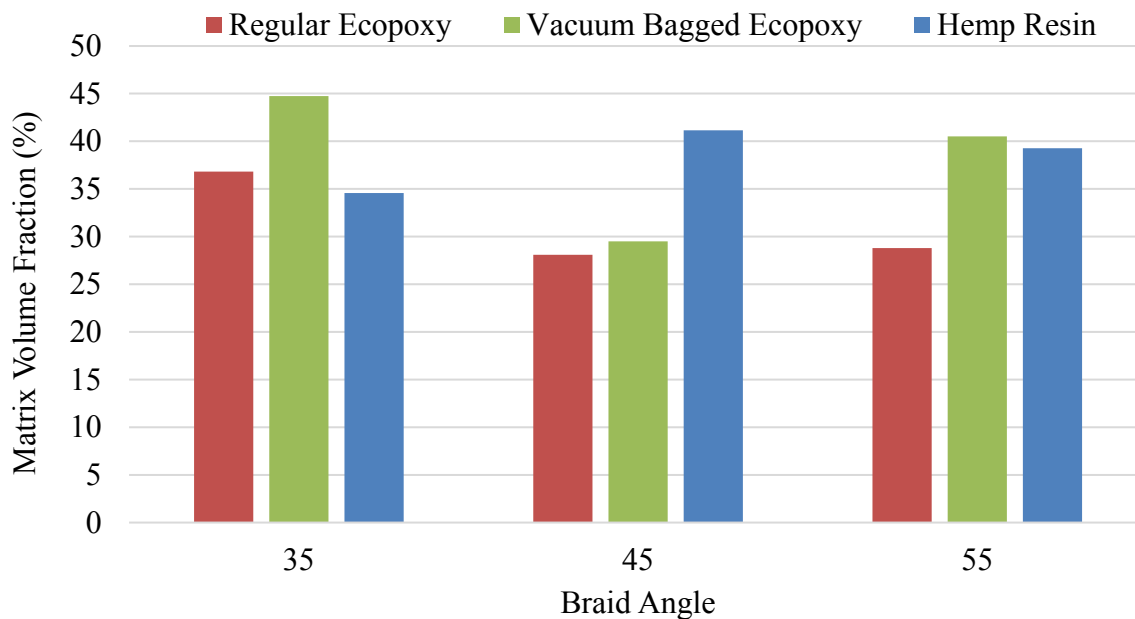


Figure 3-16. Matrix volume fraction for each sample calculated from μ CT results

The average values for fiber and matrix content per mm length of the sample can be seen in Table 3-5. The fiber content increases with braid angle as would be expected. However, the matrix content varies with greater deviation. A more precise resin measurement method is required during manufacturing to ensure consistent and uniform application.

Table 3-5. Average and deviation of fiber and matrix content per unit mm of sample length

	40°	50°	60°
Fiber Content (mm³/mm)	5.81±0.23	6.23±0.46	6.37±0.24
Matrix Content (mm³/mm)	3.83±0.57	3.29±0.61	3.99±0.74

The numerical values for the void volume content, and total number of enclosed voids are illustrated in the bar charts in Figure 3-17 and Figure 3-18. As seen in Figure 3-17, the values for void volume fraction demonstrate a clear increase with the increase of braid angle for all curing methods, except for the 60° regular epoxy sample, which decreased. Examining the void content alone, there was not a substantial difference comparing the hemp and regular Ecopoly samples. However, by studying the total number of voids the hemp samples had significantly less voids than the Ecopoly samples, meaning that the voids that were contained in the hemp samples were larger in size. The vacuum-bagged Epoxy samples contained less void content at all braid angles, verifying that vacuum bagging does assist to consolidate the composite and reduce porosity.

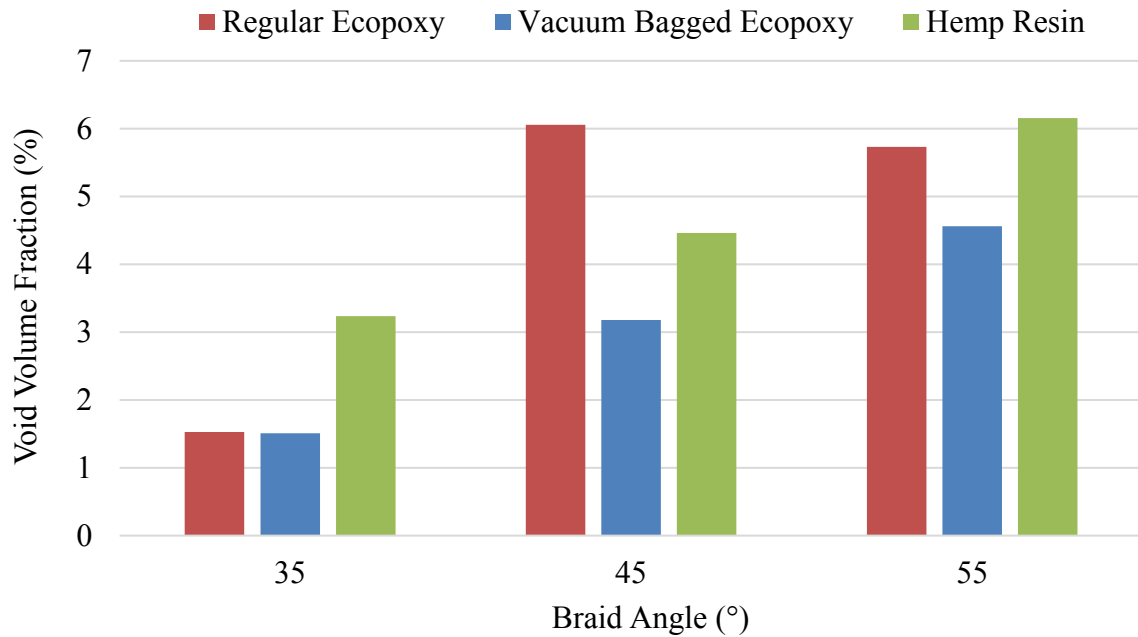


Figure 3-17. Void volume fraction for each sample calculated from μ CT results

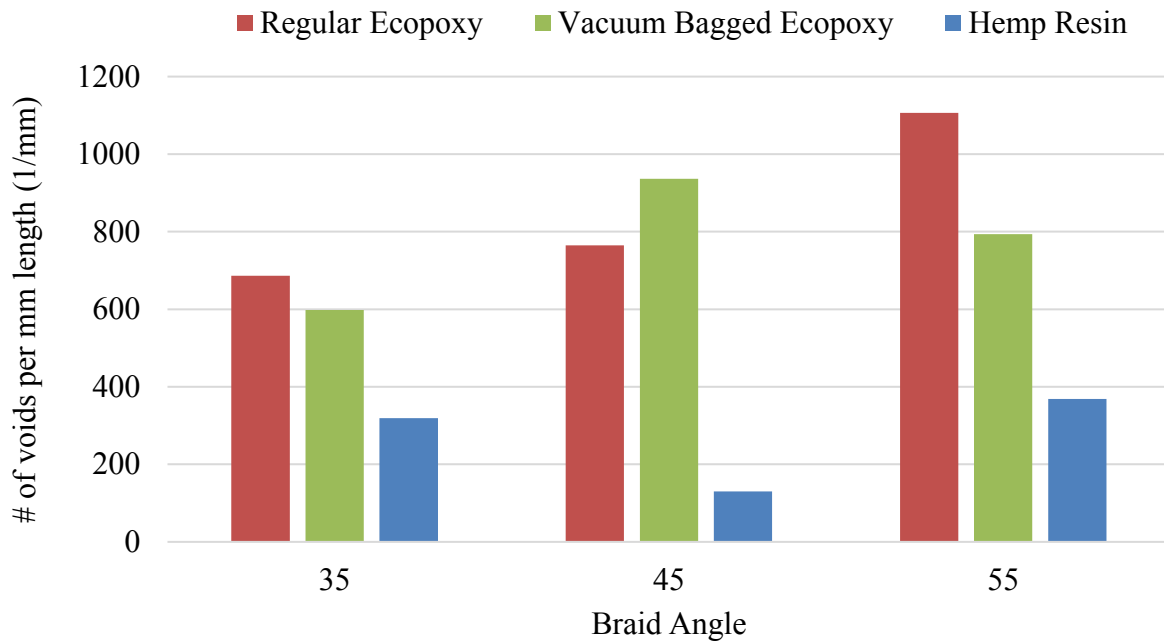
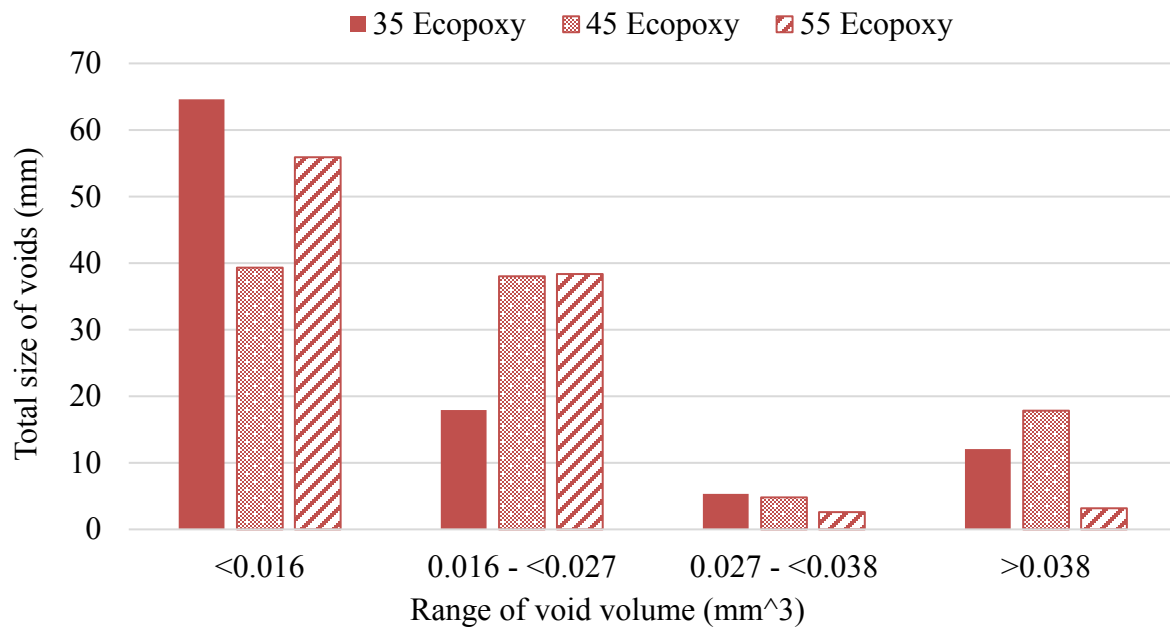


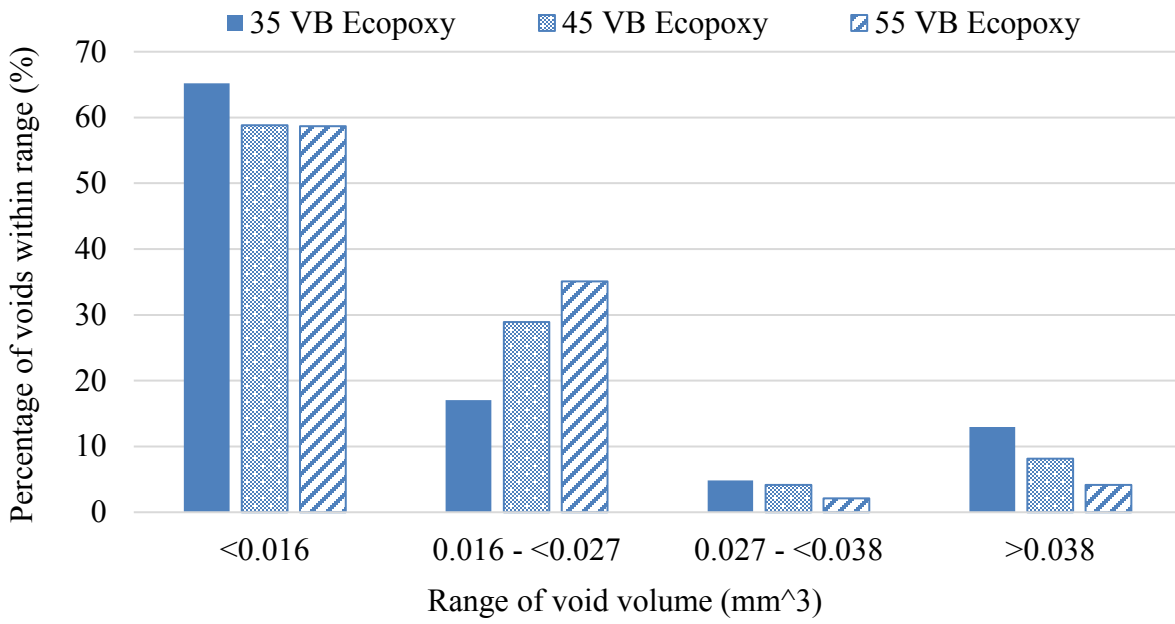
Figure 3-18. Total number of voids present in each sample calculated from μ CT results

The void distribution was also investigated since there was a large variation in the size of voids present within each sample. The results for the distribution of void volume in four different void size ranges for the nine samples are shown in Figure 3-19(a) for the Ecopoxy samples, Figure

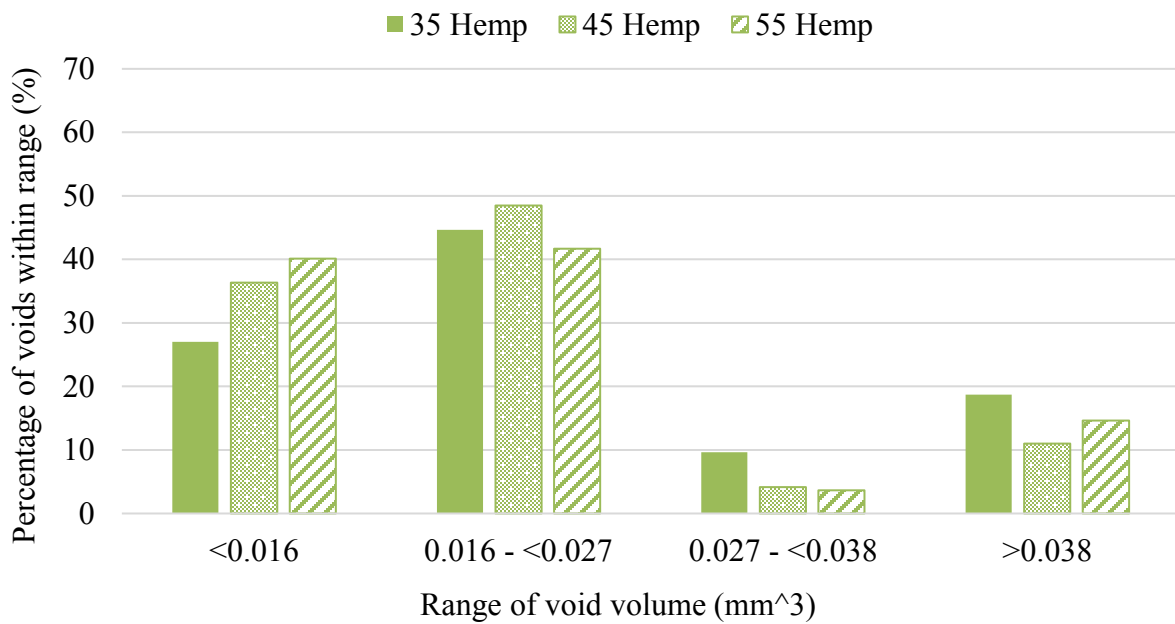
3-19(b) for the vacuum-bagged Ecopoxy samples and Figure 3-19(c) for the hemp resin samples. From the distribution results, it can be observed that the majority of voids in the Ecopoxy samples were in the range less than 0.016 mm³ for both regular and vacuum bagged. For the hemp samples however, the greatest percentage of voids were in the larger size range of 0.016-0.027 mm³. This can also be seen by comparing Figure 3-14(a) and Figure 3-14(c) as the voids are clearly larger the hemp sample than the Ecopoxy. Greater void size may be more likely to cause a greater propagation of failure, further reducing the tensile strength of the material. Therefore, it is concluded that the Ecopoxy resin serves as a more reliable matrix than the hemp resin when used with the BioMid® fibers.



(a)



(b)



(c)

Figure 3-19. Void distribution at 40°, 50° and 60° braid angles for (a) Ecopoxy samples (b) Vacuum-Bagged Ecopoxy samples and (c) hemp samples

The sample with the lowest void volume fraction was the 40° vacuum-bagged BioMid®-Ecopoxy sample, which contained 1.5% void content. A similar study that examined enclosed voids within a

Kevlar-epoxy tubular braided composite found an enclosed void volume fraction of 1.04% in a 39° braid angle [16]. The sample with the highest void volume fraction was the 60° BioMid®-hemp sample, which contained 6.2% void content. The ASTM standard for determining void content in reinforced plastics [30] claims that a high-quality composite may have a void content of 1% or less. However, it is possible that due to the load sharing of the braided structure, a greater void content has a smaller effect than it does on unidirectional reinforced composites. Dong *et al.* [29] found that porosity of 3% or less did not significantly affect the properties of three-dimensional braided composites, but an increase from 0 to 5% reduced the tensile strength by 3.9%. Therefore, for all of the 40° samples and the 50° vacuum-bagged BioMid®-Ecopoxy samples, the porosity was less than 3.2% and could be considered acceptable. For all other five samples, the porosity was greater than 4.7% and likely to cause a decrease in mechanical properties.

These results show that μ CT imaging methods can be used to determine porosity which will lead to more consistent, high-quality composite braids out of these new, natural-based materials. By applying a vacuum bagging system during curing, it is possible to produce composites that contain minimal voids and may be comparable with conventional engineering materials. However, if the yarns are fully jammed, vacuum bagging will not be sufficient to reduce the content of voids to an acceptable level. To reduce these voids further, additional pressure could be applied during curing with the use of an autoclave.

An additional consideration is the sensitivity of these results to the multiple steps in the processing procedure. In particular, selection of the threshold limits for segmenting the fibers, resin and voids is a subjective process, as the user must determine the limits visually in comparing with the original image. Due to imperfections in the images and similarity in density between the resin and fibers, image segmentation can be user dependant. A sensitivity test was performed to determine the effect

of modifying the threshold limits for the Figure 3-20. The fiber volume fraction was determined to be 53.7% with the selected threshold limits. Modifying the fiber threshold by selecting an upper limit that is 1% greater, the fiber volume fraction was determined as 48.9%. Therefore, these values are sensitive to the limits selected and manipulation of the μ CT scanner settings or the use of opaque penetrants such as zinc iodide [31] could be used to increase contrast and improve the repeatability of the image segmentation process.

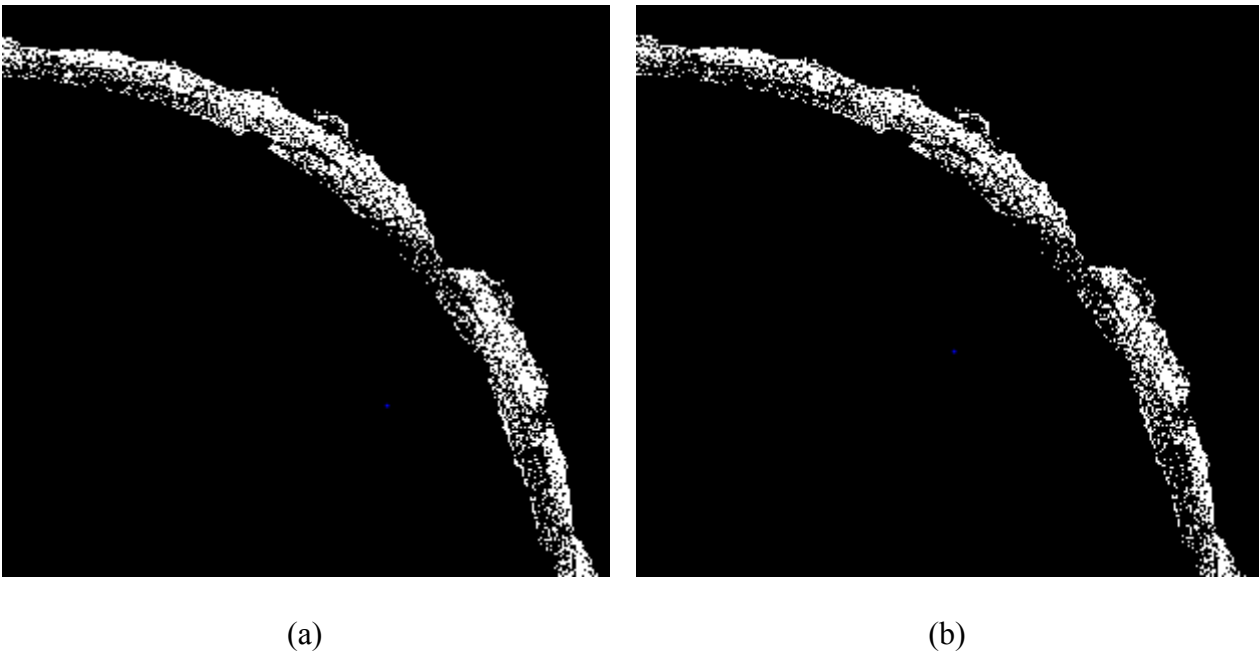


Figure 3-20. Sensitivity analysis on fiber and resin threshold limits; (a) selected threshold for fibers, and (b) a fiber threshold that is 1% greater.

It should also be noted that excessive amounts of data storage and RAM are required for these μ CT imaging methods, causing scanning and processing to be both storage and time intensive. However, the ability to visualize the location, distribution and size of all voids over an entire length of a sample results allow this method to be more versatile than other methods used to determine the fiber volume and void content fraction of composite materials such as acid digestion, matrix burn-off or microscopy.

3.4 Conclusions

The quality control of the preparation of tubular braided composites comprised of cellulose fibers and two different bio-based resins were examined. Due to the novel constituents being used, it was critical to evaluate the ability to fabricate consistent quality braided composites with these materials. This was the first study of its kind to use μ CT imaging to investigate the effect of modifying braid angle, resin type, and curing method on fiber volume fraction, void volume and void distribution. The fiber volume fraction was calculated as 59% for the 40° braids, 63% for the 50° braids and 58% for the 60° braids. It was determined that void content increased with an increase in braid angle, and vacuum bagging reduced the total void content. All of the 40° samples and the 50° vacuum-bagged Ecopoxy samples were considered to be in the range of acceptable porosity for negligible impact on mechanical properties with approximately 3% or less porosity. However, the hemp and regular Ecopoxy samples at 50° and 60° were all greater than 4.5% porosity, which was considered significant. From the results of this study, it is clear that computed tomography could help to guide the manufacture of natural fiber braided composites. Due to the high-resolution images required in μ CT scanning methods, excessive amounts of data are created and a large amount of storage and computing power is necessary to complete this work. However, these methods are accurate and versatile in comparison to other methods to achieve fiber volume and void content; critical parameters used in the modelling of composite materials. It was determined that these methods are valuable in investigating the interaction between the cellulose yarns and bio-resins and may help to improve consistency and minimize voids in order to create more accurate and reliable natural fiber braided composites.

3.5 References

- [1] X. Huang and A. N. Netravali, “Environment-Friendly ‘Green’ Resins and Advanced Green Composites,” in *Cellulose Based Composites*, J. P. Hinestroza and A. N. Netravali, Eds. Wiley-VCH Verlag GmbH & Co. KGaA, 2014, pp. 137–155.
- [2] H. Lilholt and J. M. Lawther, “1.10 - Natural Organic Fibers A2 - Kelly, Anthony,” in *Comprehensive Composite Materials*, C. Zweben, Ed. Oxford: Pergamon, 2000, pp. 303–325.
- [3] O. Faruk, A. K. Bledzki, H.-P. Fink, and M. Sain, “Biocomposites reinforced with natural fibers: 2000–2010,” *Prog. Polym. Sci.*, vol. 37, no. 11, pp. 1552–1596, Nov. 2012.
- [4] R. Dunne, D. Desai, R. Sadiku, and J. Jayaramudu, “A review of natural fibres, their sustainability and automotive applications,” *J. Reinf. Plast. Compos.*, vol. 35, no. 13, pp. 1041–1050, Jul. 2016.
- [5] D. Ray, *Biocomposites for High-Performance Applications: Current Barriers and Future Needs Towards Industrial Development*. Woodhead Publishing, 2017.
- [6] Sicomin Epoxy Systems, *SR GreenPoxy 56 Clear Epoxy Resin Technical Datasheet*, Sicomin, 2015.
- [7] One High Bio-Content Resin, *Super Sap One System Technical Data Sheet*, Entropy Resins, 2015.
- [8] Ecopoxy, *Ecopoxy Resin and Clear Hardener Technical Data Sheet*, Ecopoxy, 2016.
- [9] D. Gay, S. Hoa, and S. Tsai, *Composite Materials: Design and Applications*. CRC Press, 2002.
- [10] K. L. Pickering, M. G. A. Efendy, and T. M. Le, “A review of recent developments in natural fibre composites and their mechanical performance,” *Compos. Part Appl. Sci. Manuf.*, vol. 83, pp. 98–112, Apr. 2016.
- [11] Y. A. Gowayed, “The Effect of Voids on the Elastic Properties of Textile Reinforced Composites,” *J. Compos. Technol. Res.*, vol. 19, no. 3, pp. 168–173, 1997.
- [12] “Manual for Bruker-microCT CT-Analyser v. 1.13,” vol. 1, p. 139, 2013.
- [13] K. K. Chawla, “Micromechanics of Composites,” in *Composite Materials*, Springer, New York, NY, 2012, pp. 337–385.
- [14] J. E. Little, X. Yuan, and M. I. Jones, “Characterisation of voids in fibre reinforced composite materials,” *NDT E Int.*, vol. 46, no. 1, pp. 122–127, 2012.
- [15] J. S. U. Schell, M. Renggli, G. H. van Lenthe, R. Müller, and P. Ermanni, “Micro-computed tomography determination of glass fibre reinforced polymer meso-structure,” *Compos. Sci. Technol.*, vol. 66, no. 13, pp. 2016–2022, Oct. 2006.
- [16] G. W. Melenka, E. Lepp, B. K. O. Cheung, and J. P. Carey, “Micro-computed tomography analysis of tubular braided composites,” *Compos. Struct.*, vol. 131, no. Supplement C, pp. 384–396, Nov. 2015.

- [17] D. Zhang, D. Heider, and J. John W Gillespie, "Void reduction of high-performance thermoplastic composites via oven vacuum bag processing," *J. Compos. Mater.*, vol. 51, no. 30, pp. 4219–4230, Dec. 2017.
- [18] D. Zhang, D. Heider, and J. W. Gillespie, "Determination of void statistics and statistical representative volume elements in carbon fiber-reinforced thermoplastic prepregs," *J. Thermoplast. Compos. Mater.*, vol. 30, no. 8, pp. 1103–1119, Aug. 2017.
- [19] I. Straumit, S. V. Lomov, N. Q. Nguen, and M. Wevers, "From a micro-CT image to models of the internal geometry, defects, micromechanics and permeability of textile composites - VoxTex software," *ECCM 2016 - Proceeding of the 17th European Conference on Composite Materials*, 2016.
- [20] Composites World, "New cellulose-based fiber," Oct. 2012. [Online]. Available: <http://www.compositesworld.com/products/new-cellulose-based-fiber>. [Accessed: 12-Sep-2017].
- [21] T. S. Omonov, E. Kharraz, and J. M. Curtis, "The epoxidation of canola oil and its derivatives," *RSC Adv.*, vol. 6, no. 95, pp. 92874–92886, Sep. 2016.
- [22] T. Omonov and J. Curtis, "Aldehyde Free Thermoset Bioresins and Biocomposites," U.S. Patent, 14/442458, July 28 2016.
- [23] J. P. Carey, *Handbook of Advances in Braided Composite Materials: Theory, Production, Testing and Applications*. Woodhead Publishing, 2016.
- [24] G. W. Melenka and J. P. Carey, "Experimental analysis of diamond and regular tubular braided composites using three-dimensional digital image correlation," *J. Compos. Mater.*, pp. 3887-3907, Jan. 2017.
- [25] G. W. Melenka and J. P. Carey, "Development of a generalized analytical model for tubular braided-architecture composites," *J. Compos. Mater.*, pp. 3861-3875, Jan. 2017.
- [26] J. Hsieh, *Computed Tomography: Principles, Design, Artifacts, and Recent Advances*, 3rd Edition, Spie Press, Oct. 2015.
- [27] F. E. Boas and D. Fleischmann, "CT artifacts: Causes and reduction techniques," *Imaging Med.*, vol. 4, no. 2, pp. 229–240, 2012.
- [28] J. Chen, T.M. McBride, S.B. Sanchez, "Sensitivity of Mechanical Properties to Braid Misalignment in Triaxial Braid Composite Panels," *Journal of Composites Science and Technology*, vol. 20, pp. 13-17, Jan. 1998.
- [29] J. Dong and Y. Gong, "Influence of void defects on progressive tensile damage of three-dimensional braided composites," *J. Compos. Mater.*, pp. 2033-2045, Oct. 2017.
- [30] ASTM Standard D2734, Standard Test Methods for Void Content of Reinforced Plastics, ASTM International, West Conshohocken, PA, 2016.
- [31] J. Summerscales, *Non-Destructive Testing of Fibre-Reinforced Plastics Composites*. Springer Science & Business Media, 1987.

Chapter 4 Mechanical Testing of Cellulose Braided Composites

A version of this chapter will be submitted for publishing to *Composite Science and Technology* as a target journal.

4.1 Introduction

Many different types of naturally occurring fibres, such as hemp, flax, jute, etc., have been investigated for use as reinforcing fibres in composites [1–3]. Fibres derived directly from plants often have a large variability in mechanical properties, since their performance is dependent on many different factors in the growth process [4]. Processing 100% cellulose into regenerated yarns has shown potential to produce more consistent mechanical properties [5]. Cellulose is the compound that provides the majority of strength in plants [4] making it capable of producing high-strength natural fibre yarns.

Biopolymer-based resins are also rapidly developing as a means of replacing petrochemical based products; however, the number of these resins commercially available for purchase are still limited. There are still a number of challenges that must be overcome for these products to be relatively available for purchase; poor bonding to fibres, brittleness, and poor durability to name a few [6]. One main challenge that has inhibited the adoption of naturally-derived composite materials are lower stiffness and strength properties than conventional synthetic materials. Information on the mechanical properties of tubular braided composites composed of a naturally derived matrix with natural fibre reinforcement is not currently readily available in literature. Therefore, the purpose of this study was to produce two-dimensional (2D) braided tubular composites from 100% cellulose fibres and a bio-derived resin and determine their tensile elastic properties. This work is one aspect of a larger study investigating if “green” braids can be adequate for further research and development.

4.2 Experimental Methods

4.2.1 Sample Preparation

The samples for this study were manufactured with a continuous 100% cellulose fibre yarns (BioMid®, 1650 Denier, Shank Consulting, ENC International Corporation, Seoul, Korea) and Ecopoxy bio-resin (Ecopoxy Resin & Clear Hardener, Ecopoxy, Morris, MB). For mechanical testing, three different braid angles were manufactured in order to investigate the effect of braid angle on the elastic properties of the BioMid®-Ecopoxy braids. Five samples per test condition were used as per ASTM 3039 [7]. Figure 4-1 shows cured braids for the three different braid angles that were tested.

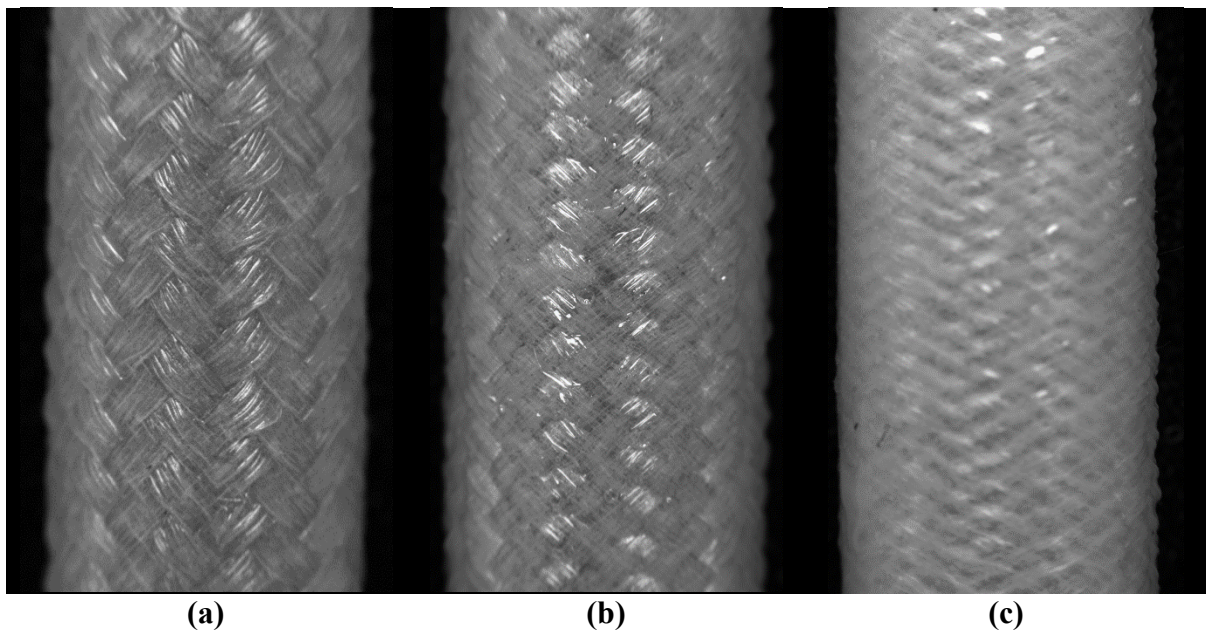


Figure 4-1. Image of cured samples at 3 different braid angles (a) 40°, (b) 50°, and (c) 60°

To allow for accurate correspondence tracking between images [8], a high contrast random speckle pattern was applied to the braid. Black matte paint (Acrylic Enamel Black, VHT Quick Coat, Cleveland, OH) was used to cover the entire braid surface, and white paint (5212 Opaque White,

Createx Airbrush Colors, Createx Colors, East Granby CT) was attached to an airbrush (Paasche H Series, Paasche Air Brush Co., Chicago, IL) to apply random speckling overtop as shown in Figure 4-2.

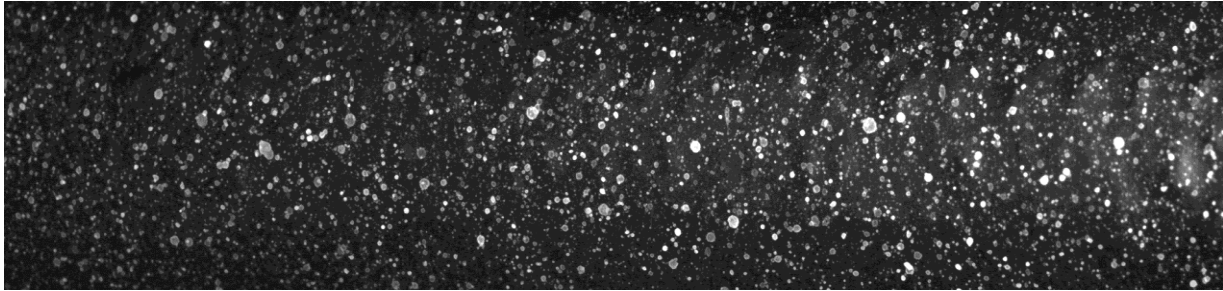


Figure 4-2. Image of a braid sample with high-contrast speckle pattern applied

4.2.2 Stereo-Digital Image Correlation (DIC)

Digital image correlation (DIC) is an optical technique used to measure the deformation of solids under an applied load. DIC is advantageous over other strain measurement techniques for the fact that it is non-invasive to the sample [8]. In addition, it allows for a representation of strain over the entire field of view of the camera as opposed to the discrete sensor locations as with the use of strain gauges or extensometers [9]. Two-dimensional DIC uses a single camera to track the 2D deformation that occurs in the plane of the camera sensor, but does not measure displacement that occurs out-of-plane. In three-dimensional DIC, multiple cameras may be used to account for out-of-plane motion and measure the full 3D displacement. Since the surface of the braid is cylindrical, some out-of-plane deformation will occur along the curvature of the braid [10], therefore 3D DIC was used for this study.

Figure 4-3 shows the resulting strain field over an entire section of a braid using DIC. It can be seen that the deformation varies greatly over the entire braid surface. Therefore it would be difficult to

acquire accurate average strain with the use of strain gauges as there could be error associated with where the sensors are placed.

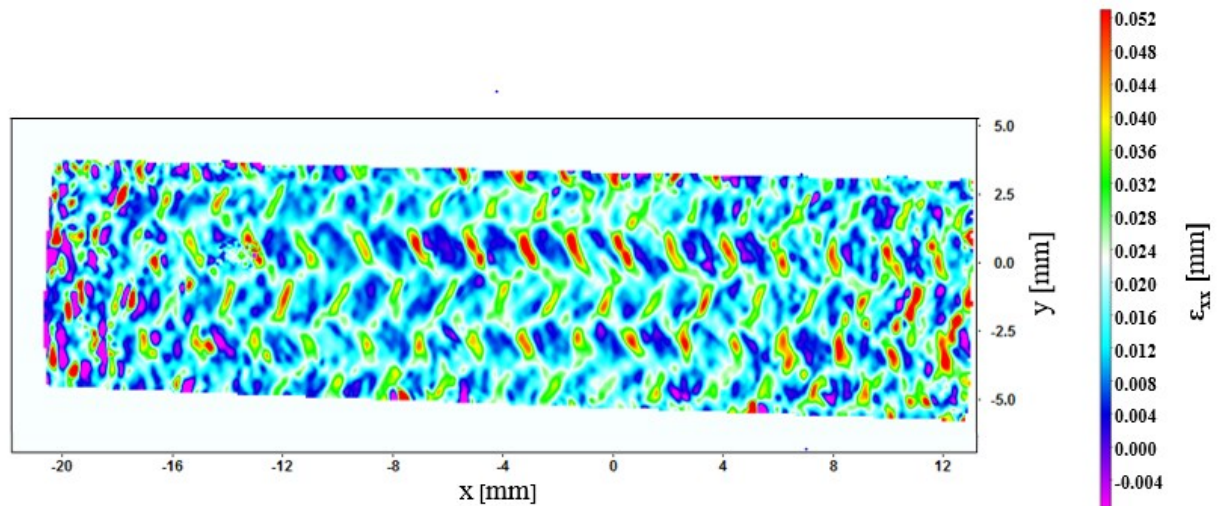


Figure 4-3. Illustration of DIC strain field on a composite braid

4.2.3 Calibration

Prior to performing the test, the load cell was calibrated by recording the load vs time for both 0 kg load and a 1 kg load attached to the tensile machine. In addition, the stereo-imaging system was calibrated with a custom-made 3D target with uniformly spaced dots. A drawing of the calibration target dimensions can be seen in Figure 4-4.

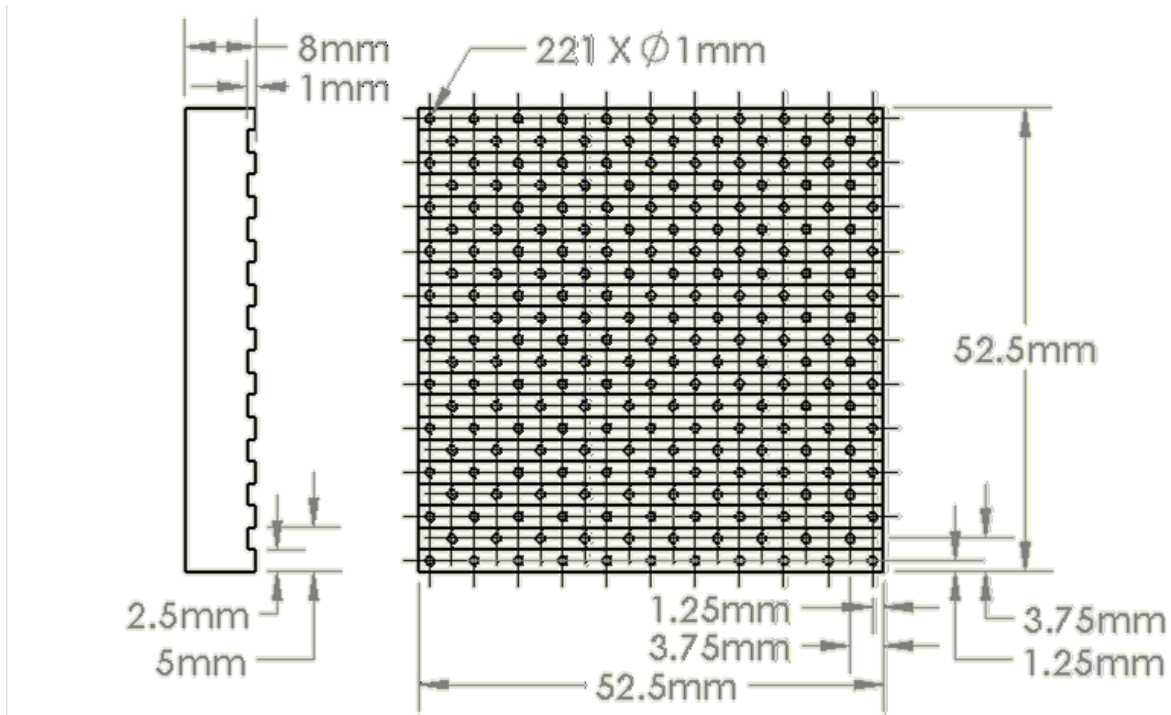


Figure 4-4. Schematic with dimensions of stereo-calibration target

The calibration target was used to convert the pixel dimensions into physical dimensions, remove image distortion, and map the two-dimensional pixel coordinates from each of the cameras into three-dimensional coordinates based on the pinhole camera model [8].

4.2.4 Testing

Tensile tests were performed with a stereo-DIC measurement system to determine the elastic properties of the cellulose fibre samples. The experimental procedure followed was based on previous stereo-DIC methods used to evaluate the properties of tubular braided composites [11].

To prepare the sample for testing, end tabs were bonded to the inner diameter of the tubular sample with an adhesive (Loctite E-20HP; Hysol, Henkel, Rocky Hill, Co.) and the sample was placed into a uniaxial testing machine (Instron 1000, Instruments and Systems for Advanced Materials Testing, Canton, Massachusetts) with a 500 N load cell. The imaging system consisted of two high-speed stereo cameras (AVT GT3400, Allied Vision Technologies, Stadtroda, Germany) attached to a lens

(LM35SC, Kowa Optical Projects Co., Tokyo, Japan and a 5 mm extension tube (CML5, Thor Labs, Newton, NJ) in order to achieve the desired field of view. An LED light source was used to illuminate the sample surface. The full stereo-DIC experimental setup is shown in Figure 4-5.

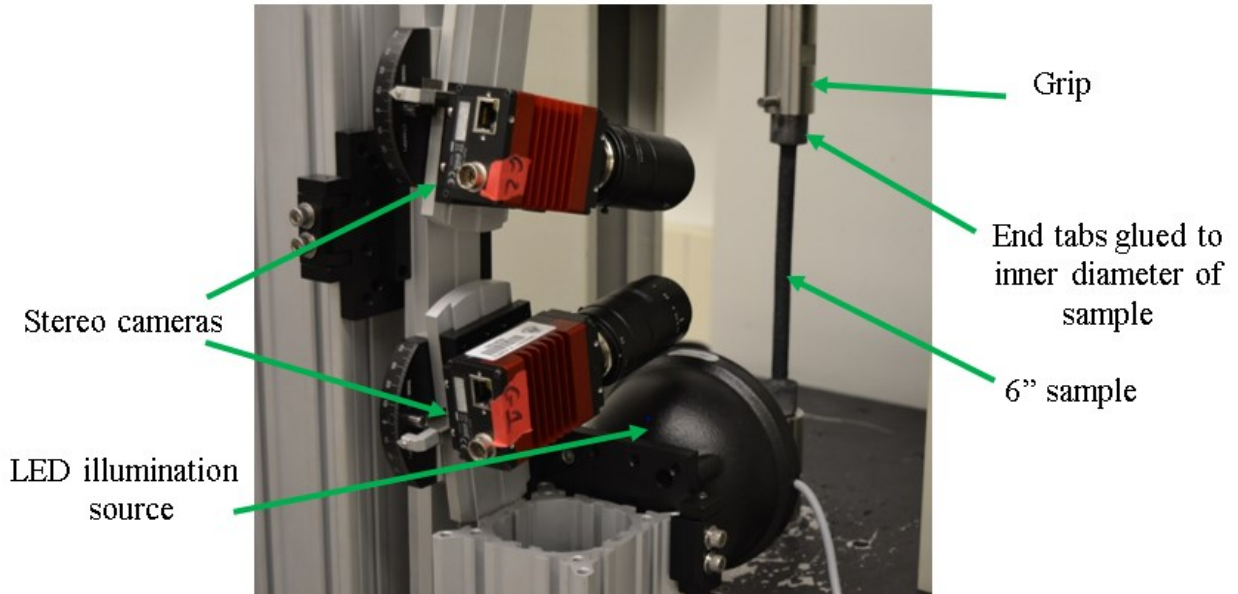


Figure 4-5. Schematic of experimental setup for tensile tests

The cameras were placed to allow for the field of view to contain a minimum of 10 total unit cells lengthwise. Since the response of a single unit cell of a tubular braid is considered to be representative of the response of the entire braid [12], 10 unit cells in the field of view was considered to allow for accurate statistical measurement. An image of the selected field of view can be seen in Figure 4-6.

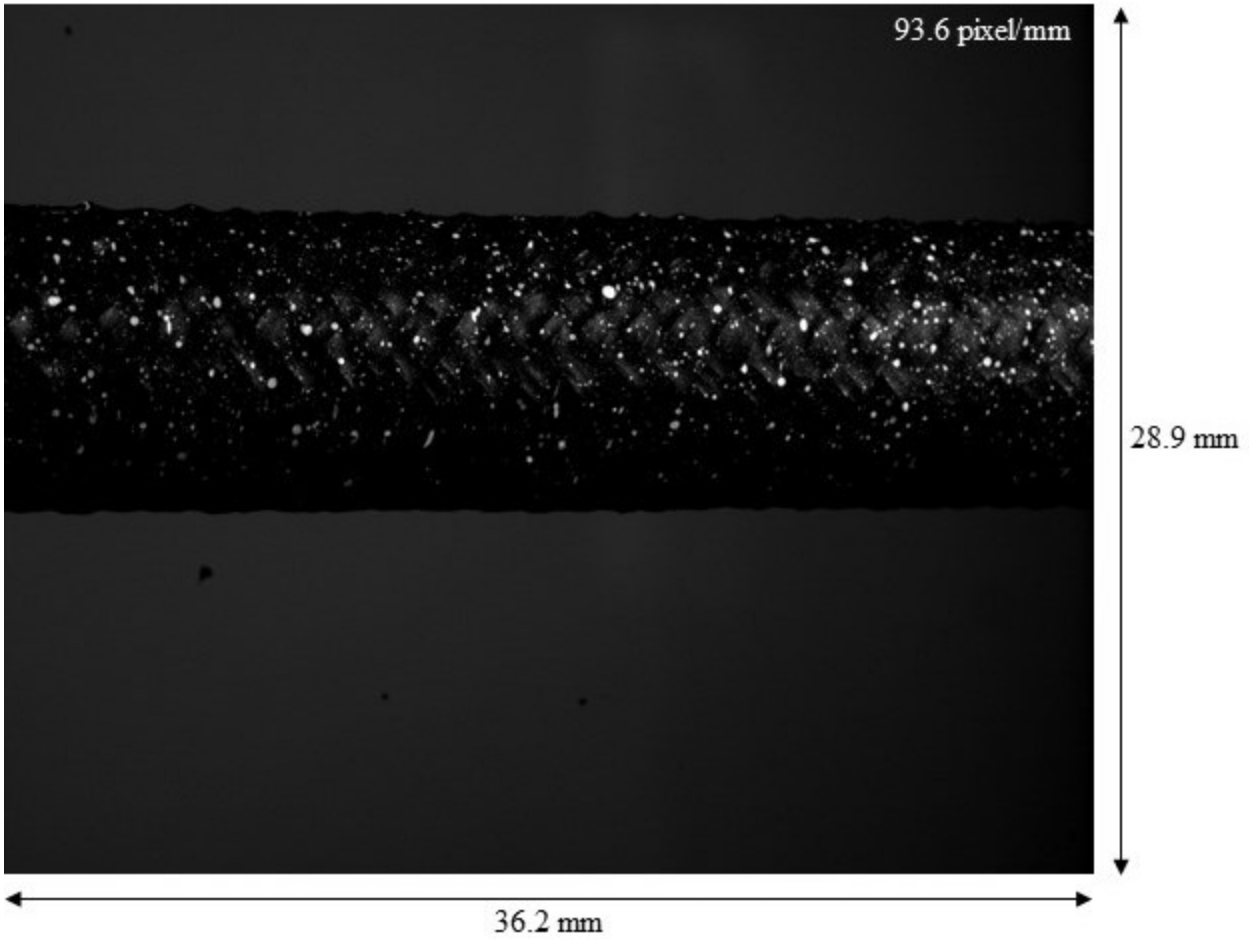


Figure 4-6. Field of view for image capture during tensile test

The test was performed using stroke control. According to the ASTM D3039 [7] the sample should be loaded such that it remains in a nearly constant strain rate that induces failure within 1 to 10 minutes of testing. To achieve this, a test was run at a crosshead speed of 0.5 mm/min, 1 mm/min and 2 mm/min and to determine which speed achieved failure in the required zone. A crosshead speed setting of 1 mm/min was determined to be adequate. During the test, images of the sample were captured with both cameras every 2 seconds. Simultaneously, load data was recorded with a data acquisition device (NI-USB 6211 DAQ, National Instruments, Austin, TX) at a frequency of 100 Hz.

4.2.5 Image Processing and Correlation

The images obtained from each camera were imported into commercial imaging software (DaVis version 8.2.0 StrainMaster 3D, LaVision GmbH, Gottingen, Germany) to process the image frames into strain maps representative of the sample's deformation during the entire tensile test. The methods followed for image processing were adapted from LA VISION StrainMaster Product Manual for DIC measurement [13].

Once the images were imported into DaVis, pre-processing was performed to enhance the images for cross-correlation. The two images were merged into a multi-frame image and camera attributes were added to each frame. A subtract sliding average filter was used to remove noise and increase contrast. A mask was applied to include only the speckled portion of the image for cross-correlation. An illustration of the original image and pre-processed image is shown in Figure 4-7.

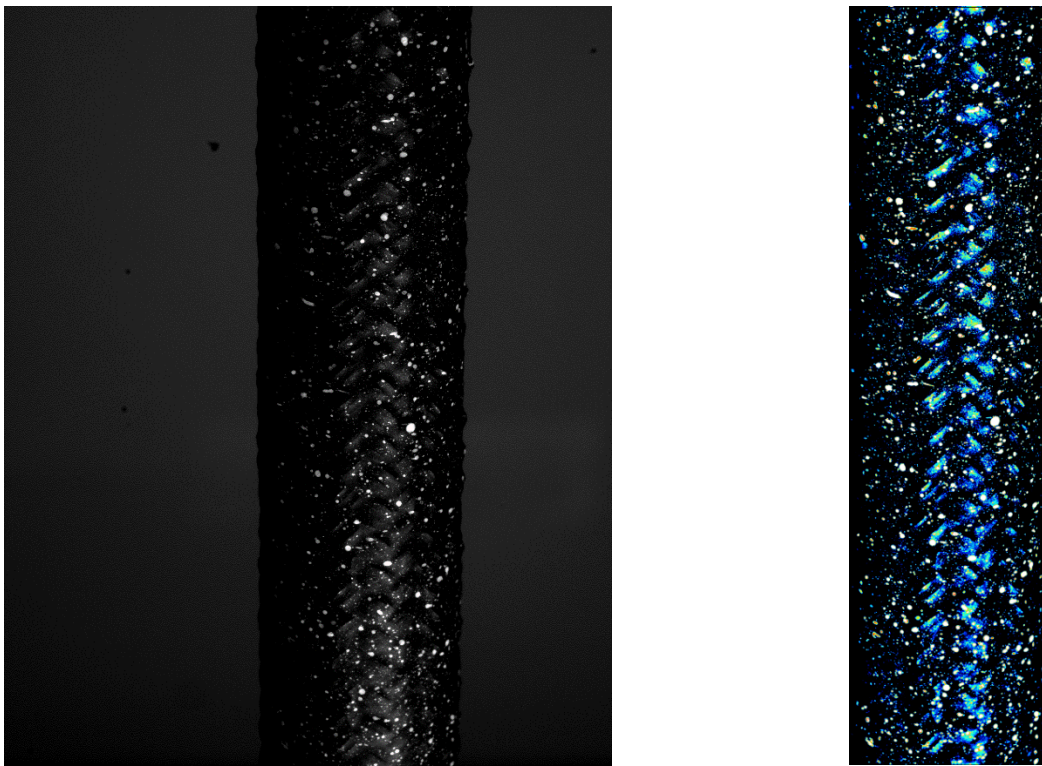
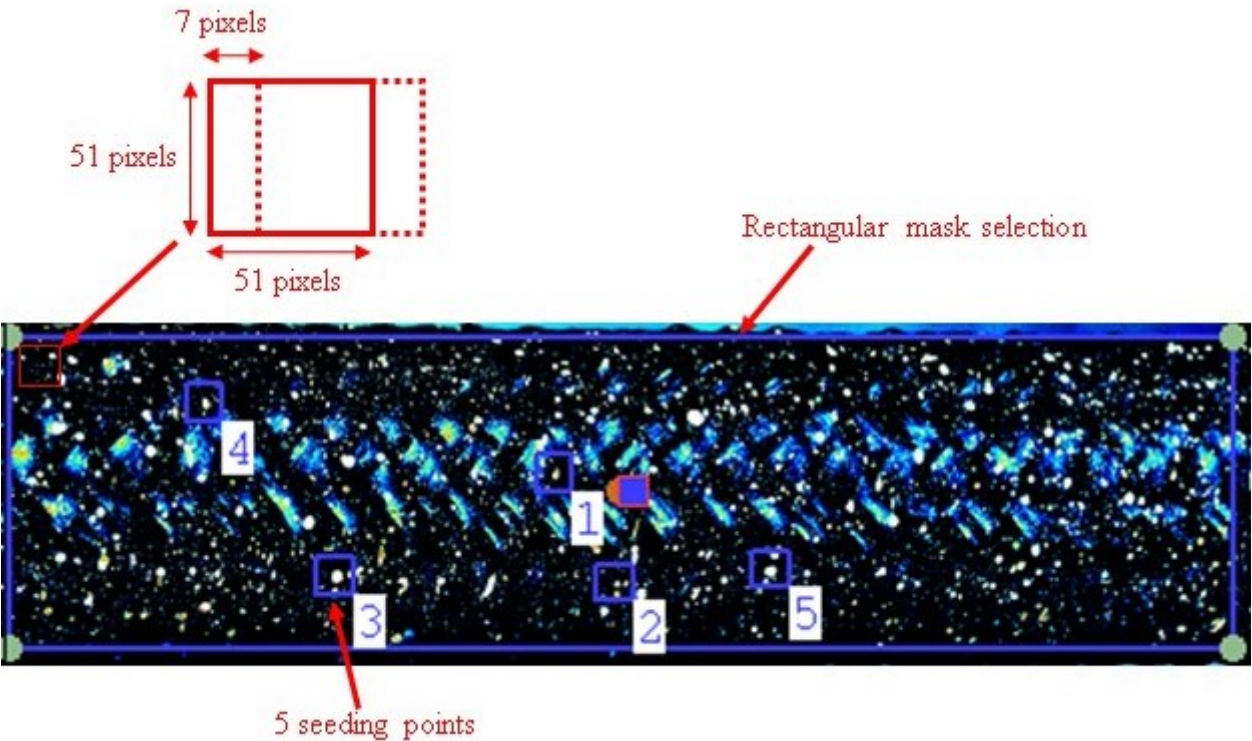
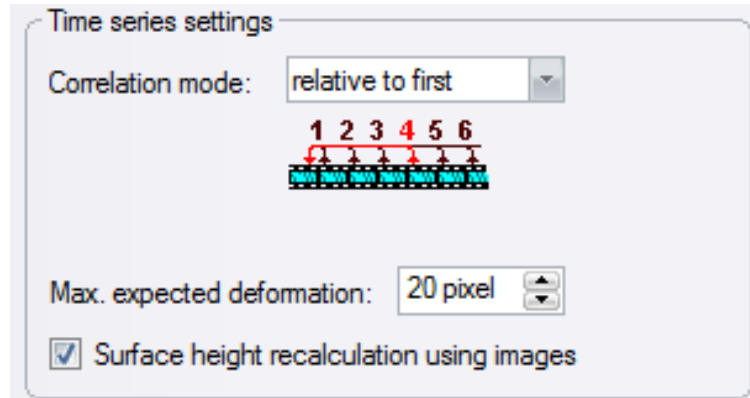


Figure 4-7. Illustration of original image compared with processed image

Once the images were pre-processed, the deformation vectors were calculated by performing the correlation algorithm. There are several important parameters the user must input to configure the correlation as illustrated in Figure 4-8. A rectangular mask was selected to only correlate the portion of the image containing the speckled sample. 5 seeding points were selected as a starting point for the DaVis algorithm to begin correlating the subsets within each consecutive image set [13]. The subset size and step size were chosen as 51 pixels and 7 pixels, respectively. To ensure reasonably accurate displacement measurements from DIC, Sutton *et al.* [8] defined a rule that image subset size should contain at least 3 x 3 speckles. Image correlation was performed relative to the first image in the sequence as opposed to the adjacent image so the error was not summed throughout the correlation process. The total expected deformation between images was set as 20 pixels to decrease computation time.



(a)



(b)

Figure 4-8. Correlation algorithm configuration steps. (a) Define image mask, seeding points and subset size; and, (b) define correlation mode and expected deformation.

The correlation algorithm was then performed with the user input steps. An overview of the correlation process performed by DaVis is illustrated in Figure 4-9. Each subset was cross-correlated between each image (the deformed image) and the first image (the reference image), creating a displacement vector in each subset within each 2D image. Translation and rotation coefficients were applied by the system as determined from the calibration to convert the 2D displacements into a 3D vector. The displacements vectors were then converted into a strain colour map representative of the full field of view.

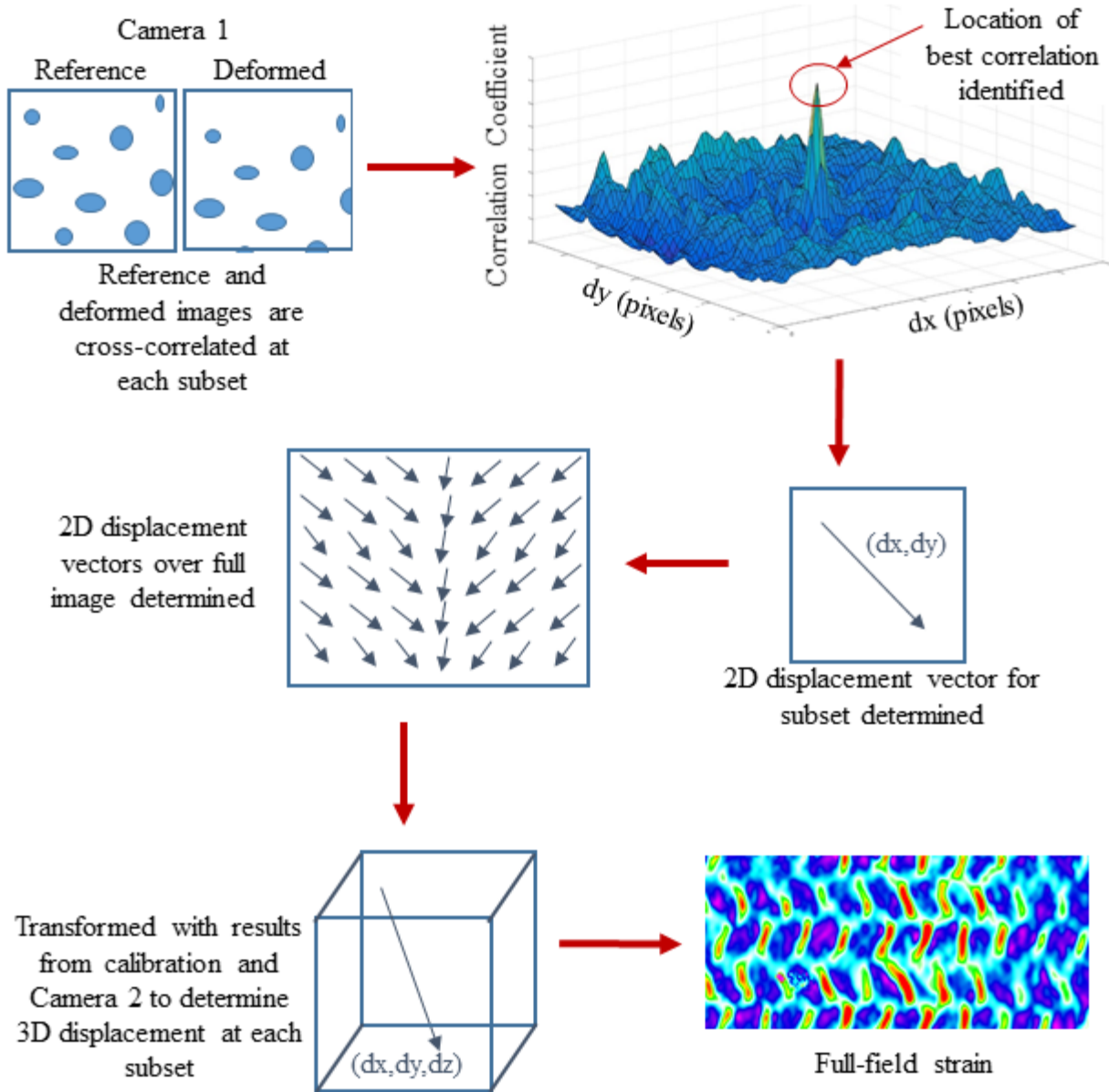


Figure 4-9. Overview of correlation process

4.2.6 Tensile Elastic Properties

The elastic modulus for each sample was determined from the numerical stress-strain data by the method of least squares according to ASTM Standard E111 [14]. This method was used as opposed to graphical methods so that the variability in the elastic modulus value could be determined statistically. The elastic modulus (E) was determined by 4.1, where X and Y are the applied axial

stress and corresponding strain values and K is the number of X,Y data pairs [14]. The goodness of the fit was determined by calculating the coefficient of determination, r^2 , and the variation in slope was determined by calculating the coefficient of variation, V_1 , from 4.2 and 4.3 respectively [14].

$$E = \frac{\sum XY - \frac{\sum X \sum Y}{K}}{\sum X^2 - \frac{(\sum X)^2}{K}} \quad 4.1$$

$$r^2 = \frac{\left[\sum XY - \frac{\sum X \sum Y}{K} \right]^2}{\left[\sum X^2 - \frac{(\sum X)^2}{K} \right] \left[\sum Y^2 - \frac{(\sum Y)^2}{K} \right]} \quad 4.2$$

$$V_1 = 100 \sqrt{\frac{\frac{1}{r^2} - 1}{K - 2}} \quad 4.3$$

4.3 Results and Discussion

4.3.1 Measurements

The geometry measurements for each of the samples is summarized in Table 4-1. The inner and outer diameters were measured with a micrometer at five locations along the braid to ensure accuracy and consistency. The braid angle was measured with an imaging software [14]. It can be seen that there was fairly large variation present in the braid angle measurements. This is likely due to both errors in the imaging measurement software as well as shifts in the yarns between initial deposit from the braider to the final cured state. Similar deviations of up to $\pm 2^\circ$ in braid angle have been documented in studies by Ayranci *et al.* [15] and Leung *et al.* [16] who manufactured tubular braided composites with the same manual fabrication procedure. Furthermore, Chen *et al.* [25] found that the braid angle from this manufacturing technique could be controlled within $\pm 3^\circ$. The majority of the samples were in this range but some had greater deviation. This could be attributed

to the fact that a smaller denier yarn was used, which increased difficulty in preventing shifts in the braid angle geometry.

Table 4-1. Results for the geometry measurements of all samples used in this study

Sample #	Designed Braid Angle (°)	Measured Braid Angle (°)	Outer Diameter (mm)	Inner Diameter (mm)
1	40	41.47 ± 0.10	11.05 ± 0.06	10.03 ± 0.06
2	40	39.35 ± 1.13	11.13 ± 0.07	10.03 ± 0.06
3	40	40.74 ± 2.60	11.03 ± 0.09	10.05 ± 0.06
4	40	42.07 ± 1.30	11.20 ± 0.03	10.02 ± 0.07
5	40	38.69 ± 1.08	10.96 ± 0.12	10.08 ± 0.02
6	50	45.23 ± 1.76	10.83 ± 0.15	9.86 ± 0.20
7	50	49.50 ± 0.63	11.11 ± 0.06	10.03 ± 0.12
8	50	50.02 ± 1.70	11.15 ± 0.02	10.10 ± 0.13
9	50	50.55 ± 0.17	11.10 ± 0.05	10.07 ± 0.03
10	50	52.97 ± 1.03	11.16 ± 0.05	10.06 ± 0.09
11	60	62.42 ± 0.87	11.26 ± 0.11	10.06 ± 0.04
12	60	60.15 ± 1.29	11.28 ± 0.13	9.99 ± 0.07
13	60	63.75 ± 1.00	11.34 ± 0.11	9.98 ± 0.05
14	60	63.16 ± 0.39	11.24 ± 0.05	10.00 ± 0.06
15	60	60.60 ± 0.60	10.90 ± 0.04	9.60 ± 0.04

4.3.2 Calibration

The results from the pinhole calibration defining the scale and transformation between cameras can be seen in Table 4-2. These values are calculated by DaVis from the known dimensions of the calibration target and then applied to the frames of each camera for the images of the sample to map the 2D pixel displacements in the image to a single 3D displacement in each frame.

Table 4-2. Pinhole calibration parameter results

Parameter	Camera 1	Camera 2
Focal length (mm)	48.45	44.15
Scale (pixel/mm)	90.39	90.39
Tx (mm)	-2.15	1.25
Ty (mm)	-0.83	0.48
Tz (mm)	147.03	136.18
Rx (°)	-5.11	-5.82
Ry (°)	7.88	-10.98
Rz (°)	-0.52	-0.64

4.3.3 Strain Mapping

The full-field strain was computed for each image captured during testing for all samples. Figure 4-10 demonstrates a close-up of a strain field generated in comparison with an image of a braid sample. It can be observed that the regions of high local strain correspond to the locations between the yarns that are resin-rich, and the locations of low local strain correspond to the reinforcement regions, where there is a high volume of reinforcing fibres present.

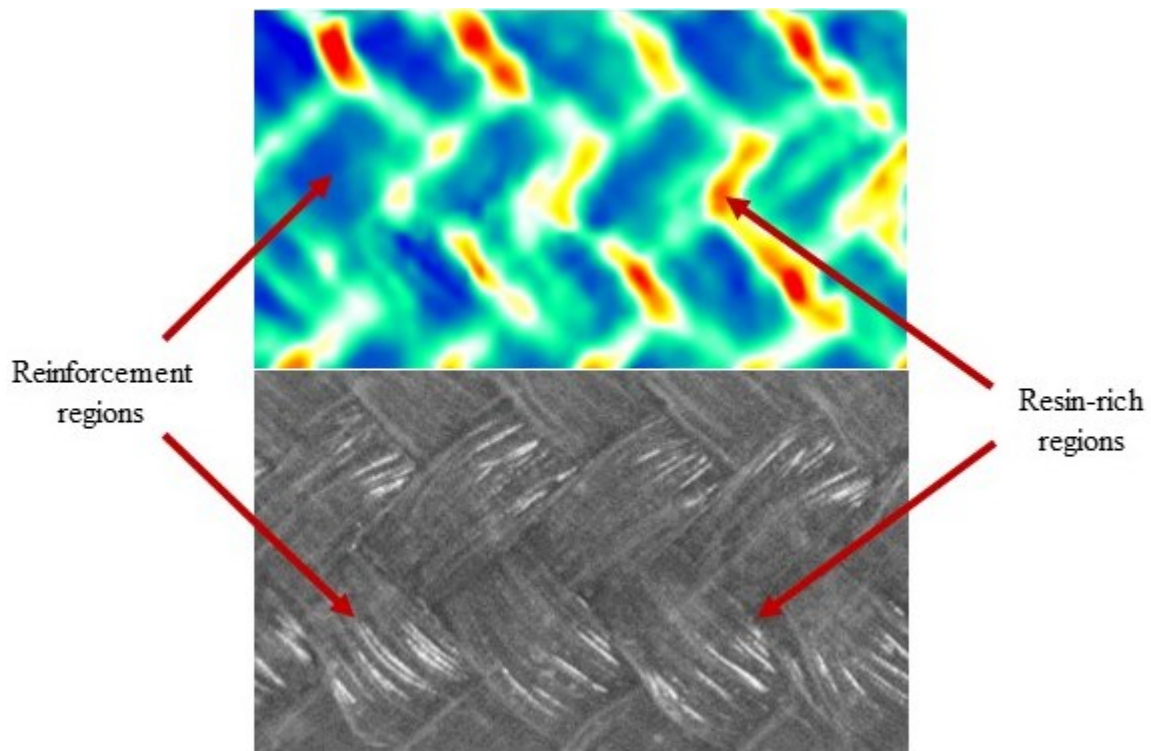
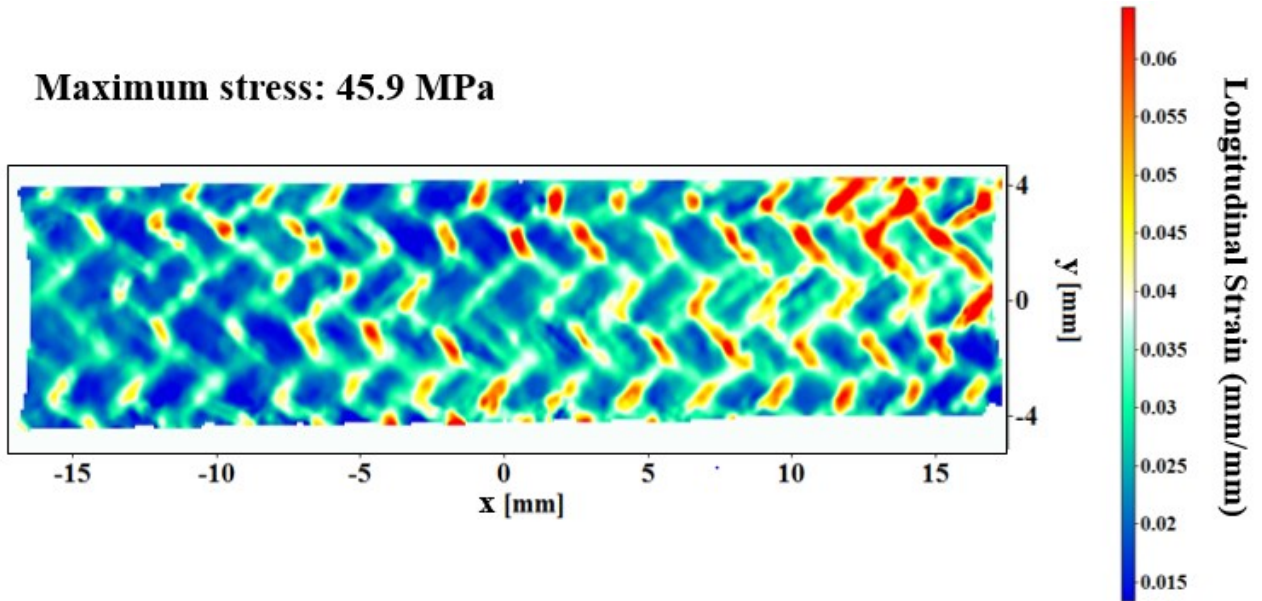


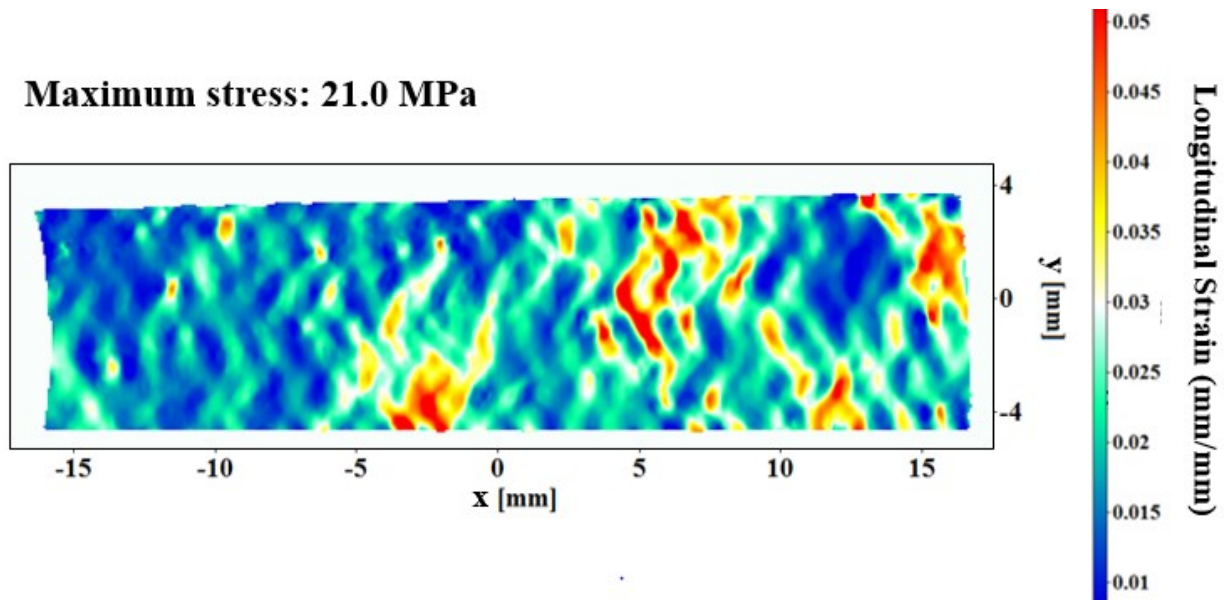
Figure 4-10. Image identifying the reinforcement and resin rich regions

A sample image of a strain field obtained at each braid angle is shown in Figure 4-11. The image frames shown were taken at the time of maximum stress on the stress-strain curve. As can be seen, the maximum stress decreased as the braid angle was increased and the maximum local strain value decreased as the braid angle increased. In the 40° sample, it can be seen that the strain magnitudes in the regions corresponding to the locations of the reinforcing yarns are approximately 0.015

mm/mm compared to 0.06 mm/mm shown in the regions that are resin rich. As the braid angle is increased, the size of the resin rich regions decreases since the yarns are more closely packed, resulting in less distinction in the high strain values in that location.

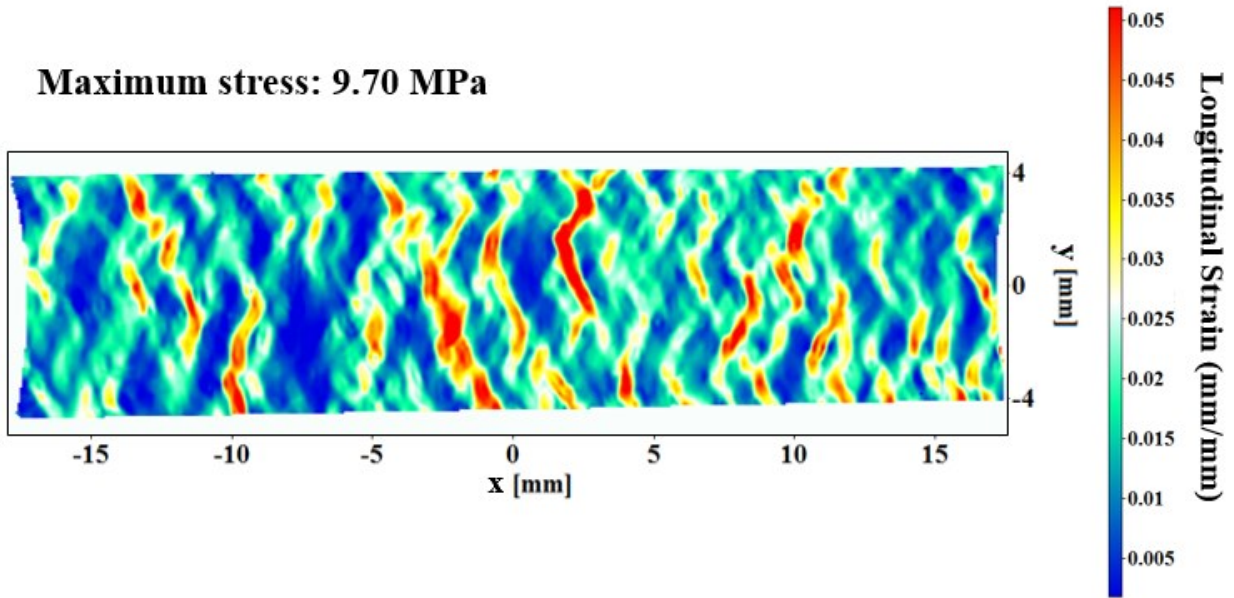


(a)



(b)

Maximum stress: 9.70 MPa



(c)

Figure 4-11. Images of a sample strain field produced at the image of maximum stress for at each braid angle; (a) 40°, (b) 50° and (c) 60°

The average strain in each frame was computed with the use of a strain gauge as shown in Figure 4-12. The strain gauge works as a virtual extensometer by following the two selected points over time to determine the average strain value in each frame.

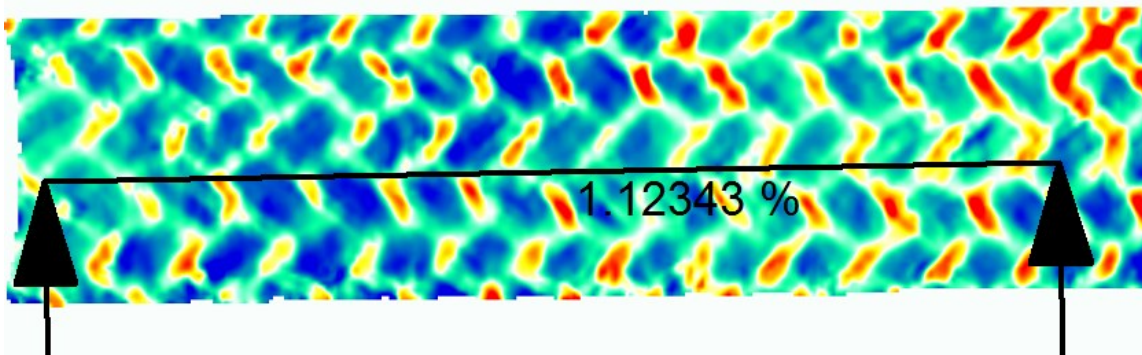
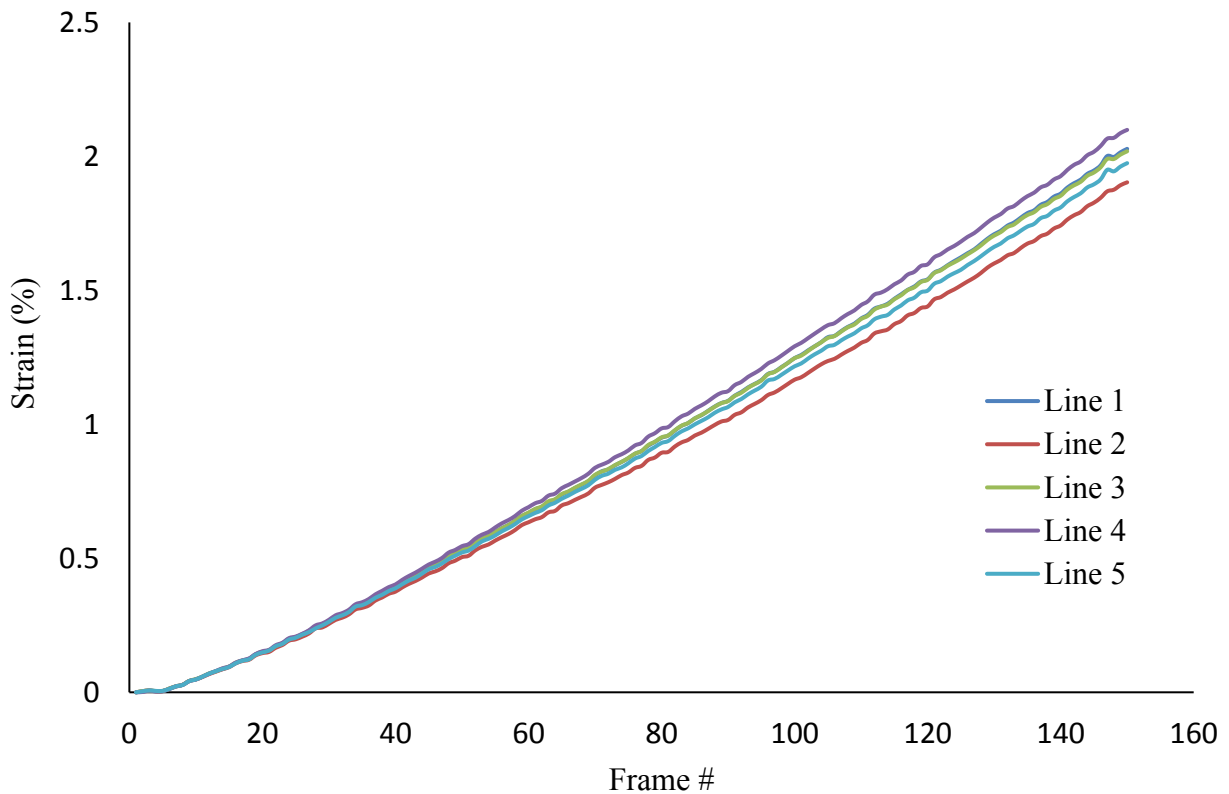


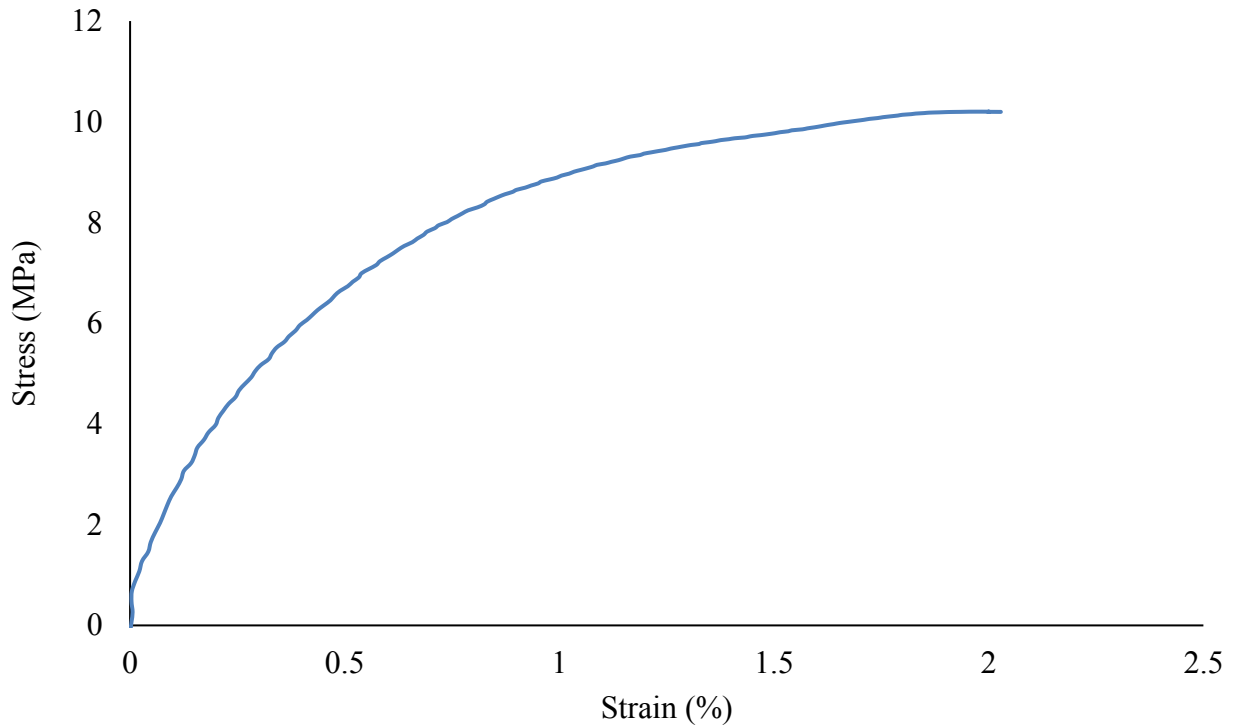
Figure 4-12. Image of the virtual strain gage used to average strain over the field of view for an arbitrary image frame

The sensitivity of the strain results to the points selected on the image were examined by plotting the strain results as a function of images for 5 different sets of points for sample 15. The results

are shown in the plot in Figure 4-13(a). It can be seen that the curves begin united but begin to diverge in later frames as the strain extends into the plastic deformation region. However, as seen Figure 4-13(b), for the stress-strain curve for this particular sample, the yield point occurs at less than 0.5% strain. Looking at the range of the y-axis in Figure 4-14(a), corresponding to 0 to 0.5% strain, the curves are still in very good agreement, and therefore for the purpose of this study, the strain results in the elastic region are not sensitive to strain gauge location. The variation is greater as the deformation moves further into the plastic zone, however, even at the location of the largest range, the strain only deviates 0.2%.



(a)



(b)

Figure 4-13. (a) Graph demonstrating the sensitivity of the location of virtual strain gauge line on the output of strain for five different lines on Sample 15 (b) Stress-strain curve for sample 15 used to demonstrate sensitivity of strain gauge placement

4.3.4 Applied Load and Stress

Phase distortion was removed from the original voltage data obtained from the DAQ by a Matlab function (filtfilt) that performs zero-phase digital filtering to remove the noise collected by the load cell. Standardized weights were used to determine the ratio of voltage output to Newtons to convert the voltage data to load data. The full load cell calibration method can be seen in Appendix A. A plot showing a sample original load vs. time curve and the filtered curve is shown in Figure 4-14. It is likely that signal interference is occurring, such as building vibrations or interfering electrical radiation, causing the fluctuations in noise. It should be noted that it is not possible that the large

transient spikes are actually occurring as tubular braids are not strong in compression and would crush if subjected to compressive loads of up to 600 N.

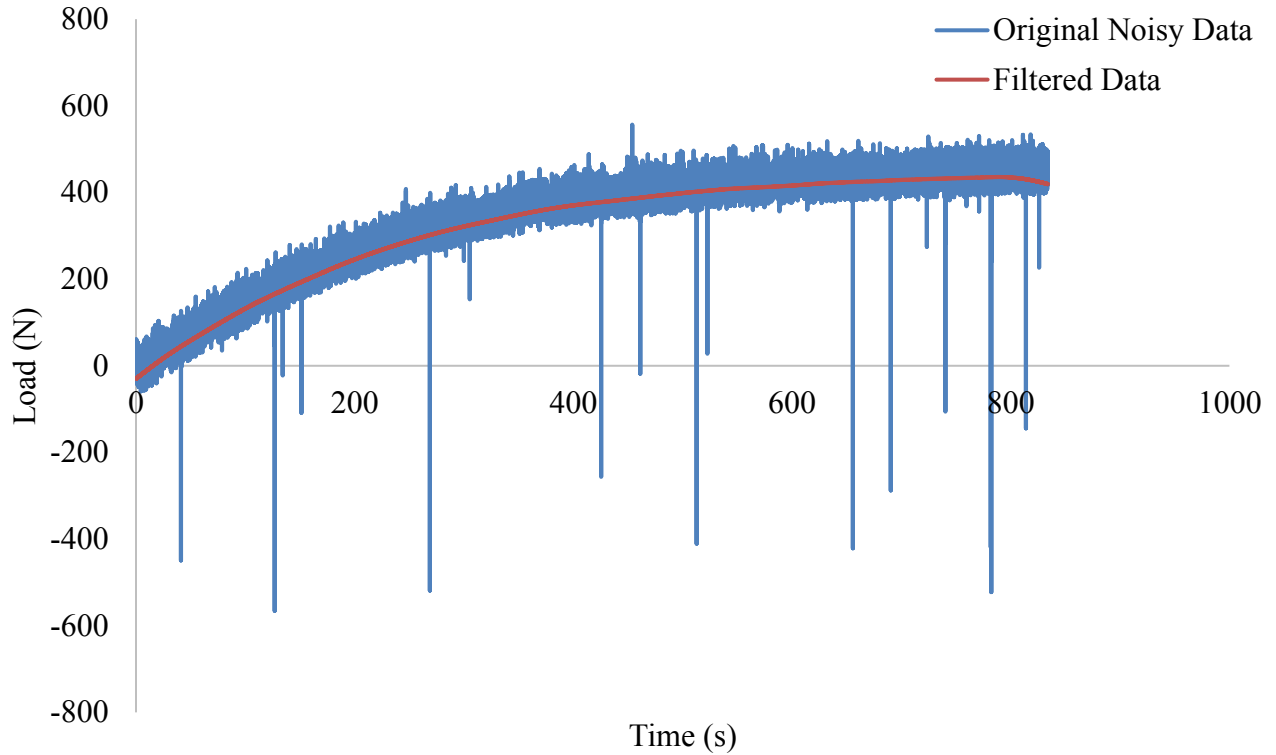


Figure 4-14. Plot of the original noisy voltage data and voltage data with a zero-phase distortion filter as a function of time

The load data was then converted to normal stress by dividing by the original cross-sectional area measured for each specific sample, according to 4.4.

$$\sigma = \frac{P}{A} \quad 4.4$$

4.3.5 Stress-Strain Curves

The stress-strain curves were plotted for all samples. Figure 4-15 shows the stress-strain behaviour for five samples at each of the braid angles. It can be seen that the yield point and ultimate strength decrease as the braid angle is increased; as expected. There are multiple possible sources for the

variation in results. The largest source is the difficulty in ensuring uniform and consistent braid angle for every sample. With the fabrication method used, the yarns are braided into preforms onto the machine braiding mandrel, and then transported onto curing mandrels before being coated in resin and cured. In these steps it is possible for the yarns to shift from the original braid angle before setting. The strength and elastic modulus of braided composites are known to be extremely sensitive to a change in braid angle [11, 12]. Another source of uncertainty is the variation in fibre volume ratio. Since the samples were manufactured by manual impregnation, uniform application of the resin is difficult to ensure across the whole length of the sample. The individual stress-strain curves for all 15 samples can be seen in Appendix B.

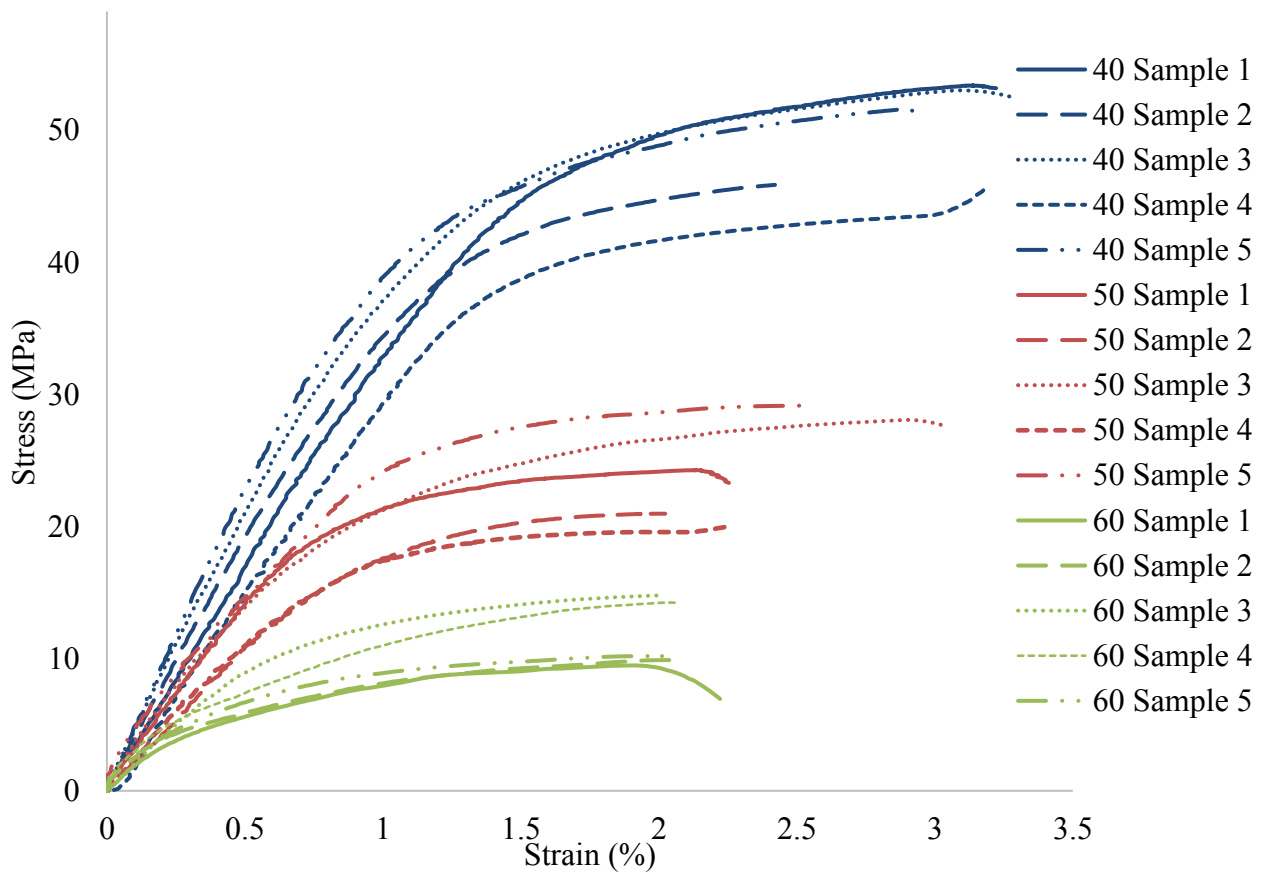


Figure 4-15 Plot showing the stress-strain curves for five samples at each the three sample braid angles

The failure mode also differed with each braid angle as shown in Figure 4-16. The 40° braids failed due to fibre fracture with very little propagation in the matrix. However, the 50° braid showed small failure along the matrix region before fibre failure and the 60° braids exhibited failure in the matrix region along the entire length of the braid before the fibres fully failed at the end tabs. This explains the behaviour of the stress-strain curves in Figure 4-15, as the 40° braids fracture close after reaching their maximum stress in the plastic zone, while the 60° braids plateau once reaching their maximum in the plastic zone until failure. A similar trend was seen in a study by Harte *et al.* [17] where braid angles less than 50° failed due to fracture of the fibres and braid angles greater than 50° exhibited necking prior to failure. At small braid angles, the properties of the braid are dominated greatly by the reinforcement, and therefore the braid reaches catastrophic failure when it fractures completely at the fibers. As the braid angle increases, the reinforcing fibers begin to decrease in dominance while the matrix begins to increase. As a result, failure occurs at lower loads and begins progressive fracture in the matrix along the length of the braid prior to catastrophic failure of the entire composite.

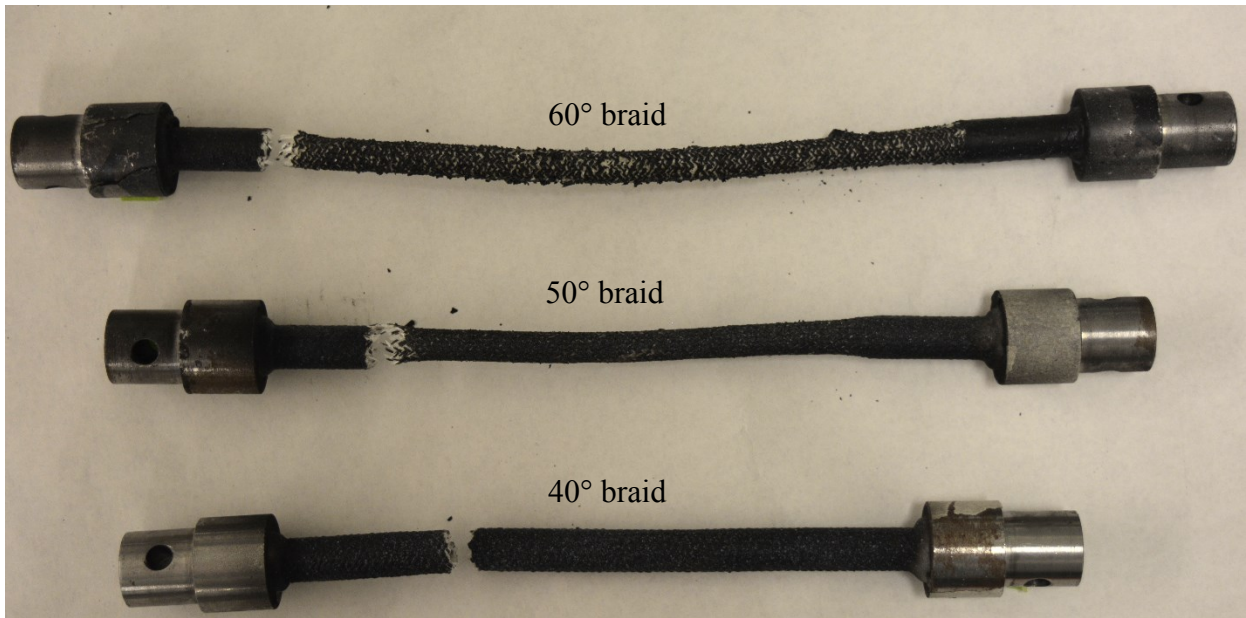


Figure 4-16. Image comparison of the failure modes of the three different braid angles

4.3.6 Tensile Elastic Properties

The results for the elastic modulus calculated for each sample by the least squares regression method are given in Table 4-3. Observing that the coefficient of determination is greater than 99% for 14 of the 15 samples and greater than 98% for the remaining sample, an accurate linear fit has been achieved through the data points. In addition, the coefficient of variation is 2.5% or less for all samples, indicating that there was high precision in the results.

Table 4-3. Elastic modulus and fit parameters calculated for each sample

Sample #	Ideal Braid Angle (°)	Measured Braid Angle (°)	Elastic Modulus, E (GPa)	Coefficient of determination, r^2	Coefficient of variation, V_1 (%)
1	40°	41.47	3.33	0.99933	0.24
2		39.35	3.60	0.99832	0.38
3		40.74	3.74	0.99543	0.64
4		42.07	3.07	0.99832	0.38
5		38.69	4.20	0.99602	0.59
6	50°	45.33	2.50	0.99238	1.01
7		49.50	2.67	0.99777	0.54
8		50.02	2.09	0.99744	0.58
9		50.55	1.94	0.99120	1.08
10		52.97	2.42	0.99339	0.94
11	60°	62.42	1.68	0.99237	1.79
12		60.15	1.99	0.99808	0.86
13		63.75	1.89	0.99102	2.38
14		63.16	2.14	0.99846	0.77
15		60.60	1.40	0.98381	2.52

The resulting elastic modulus for the experimental data was plotted with measured braid angle as shown in Figure 4-17. As shown, these values were compared with results from a model developed by Melenka *et al.* [18] to predict the properties of tubular braided composites based on their constituent properties. Several assumptions were made for the model inputs as there is no data currently available on the transverse properties of cellulose fibers due to the challenge in obtaining these properties with experimental measures. The transverse modulus for jute fiber has been estimated to be one seventh of the longitudinal properties [3]. Since jute is largely comprised of cellulose, this assumption was applied to the BioMid fibers. In addition, the Ecopoxy resin has not been tested mechanically, so the matrix properties used were based on SuperSap resin, another commercially available bio-based resin.

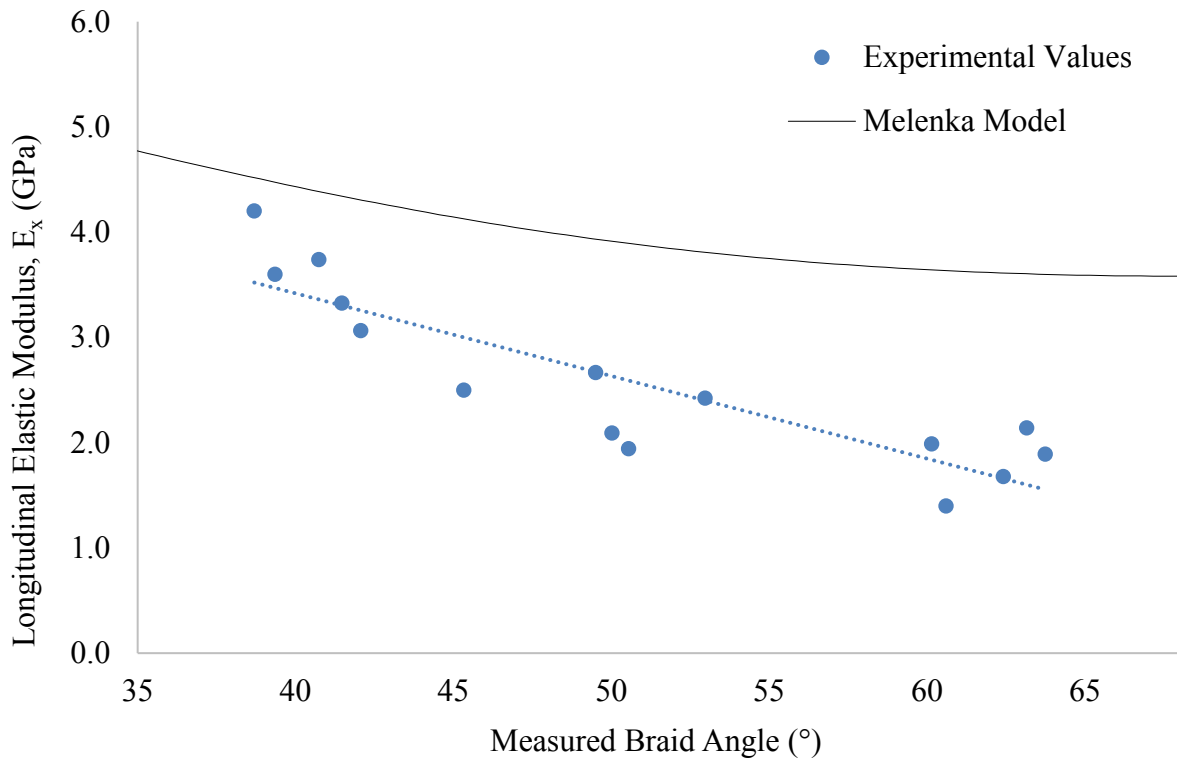


Figure 4-17. Scatterplot showing the experimental results of longitudinal elastic modulus as a function of braid angle compared with values predicted by a model created by Melenka et al. [18]. Experimental results were fitted with a least squares regression line.

It can be seen that the model predictions are higher than the experimental values. However, the BioMid® fibers used in this study had been in storage for several years since acquired from the manufacturer. This raises a question regarding the durability of the fibers, which needs to be addressed. In addition, it is possible that the properties of the Eco epoxy are fairly less than the Supersap used for assumption which would decrease the model predictions. However, the general trend is very similar and shows that an increase in braid angle yields a decrease in elastic modulus. This trend follows other studies that have looked at the behaviour of changing braid angle [11, 14, 19, 20]. When the braid angle is smaller, the fibre reinforcement is aligned closer to the longitudinal direction resulting in greater stiffness in tensile loading. The variation in elastic modulus for each sample manufactured to the desired braid angles (40°, 50° and 60°) is illustrated

in the bar chart in Figure 4-18. It can be seen that the average braid angle decreased with braid angle, however there was variation among all the samples.

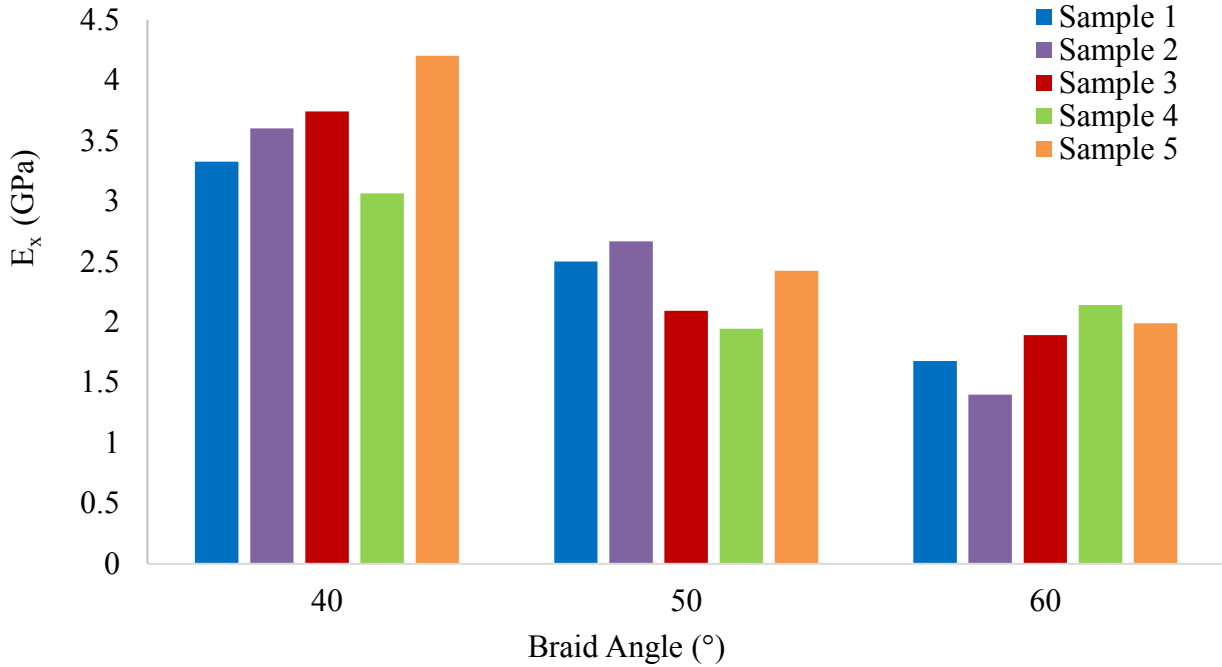


Figure 4-18. Bar graph showing the variation in elastic modulus for each desired braid angle

The largest calculated modulus was determined to be 4.20 GPa for a 39° braid. The values for the average and standard deviation in the measurements for the 5 samples at each braid angle are shown in Table 4-4.

Table 4-4. Variation in measured braid angle and elastic modulus

Desired θ (°)	Measured θ (°)	E (GPa)
40	40.46 ± 1.68	3.59 ± 0.43
50	49.65 ± 2.69	2.33 ± 0.30
60	61.56 ± 2.04	1.82 ± 0.29

As it can be seen there is significantly large variation in the measured braid angle with a standard deviation of up to 2.7°, which is likely the cause of the variation in elastic modulus. This variation

in braid angle is likely due to human error in the manual impregnation procedure. Therefore, in order to obtain more consistent samples, more controlled measures in the manufacturing procedure should be established in order to prevent the yarns from shifting before final cure.

Qamhia et al. [21] looked at triaxially braided composites comprised of BioMid® fibers and found an elastic modulus of 11.22 GPa for a [-60/0/60] ply, approximately 6 times greater than that of the 60° biaxial braids in this study. Triaxial braids allow reinforcement along the axis of tensile loading, and would be expected to be much stiffer than the 2D biaxial braids. For instance, Xu et al [22] compared biaxial and triaxial braids and found the stiffness to be approximately 5 times greater for a triaxial braid at the same braid angle. Therefore, these results are reasonable in comparison with literature available.

4.3.7 Comparison with Conventional Materials

The results are compared with studies done by Carey et al. [23], Melenka et al. [11], Ayranci et al. [10], and Harte et al. [17] on tubular braided composites comprised of conventional materials in Figure 4-19.

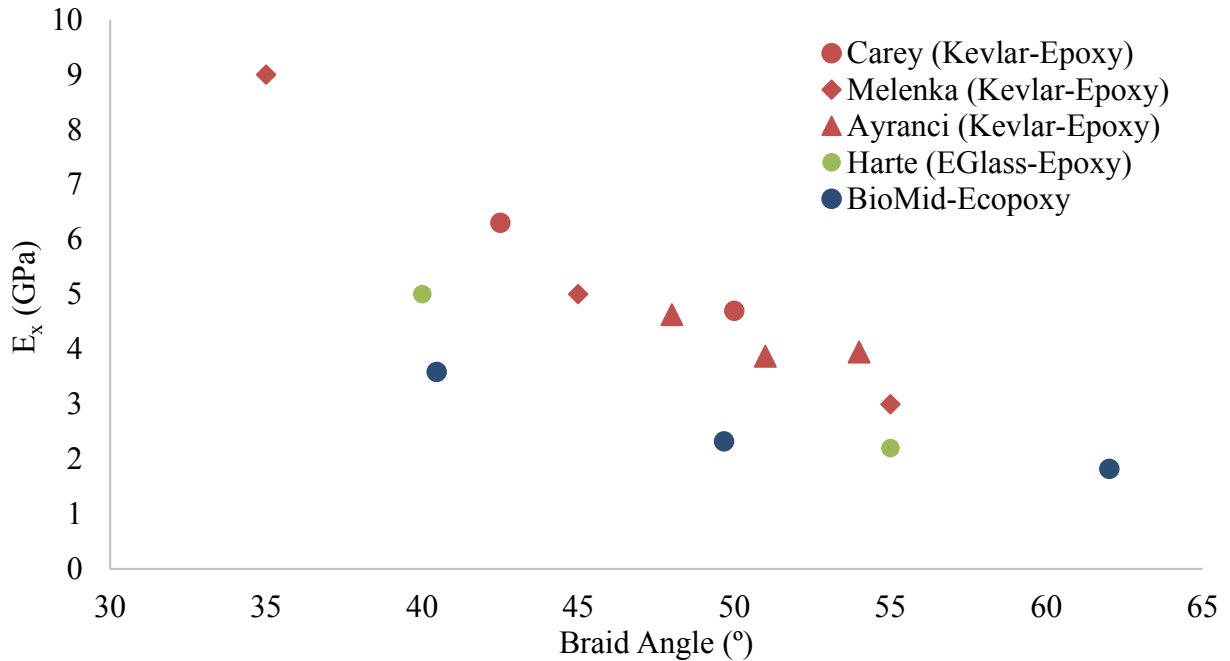


Figure 4-19. Scatter plot showing the comparison of longitudinal elastic moduli of BioMid samples with several other studies on tubular braids comprised of conventional materials

It is observed that the elastic moduli of the BioMid® samples are approximately half that of Kevlar samples and less than the e-glass samples. However, since composites are often used for weight-critical applications, the specific elastic modulus are also important to consider. The values from these studies were also plotted as a ratio of the density of the fiber, ρ_f , in Figure 4-20. Kevlar has a density of 1.44 kg/m^3 , glass has a density of 2.55 kg/m^3 , and BioMid has a density of 1.5 kg/m^3 .

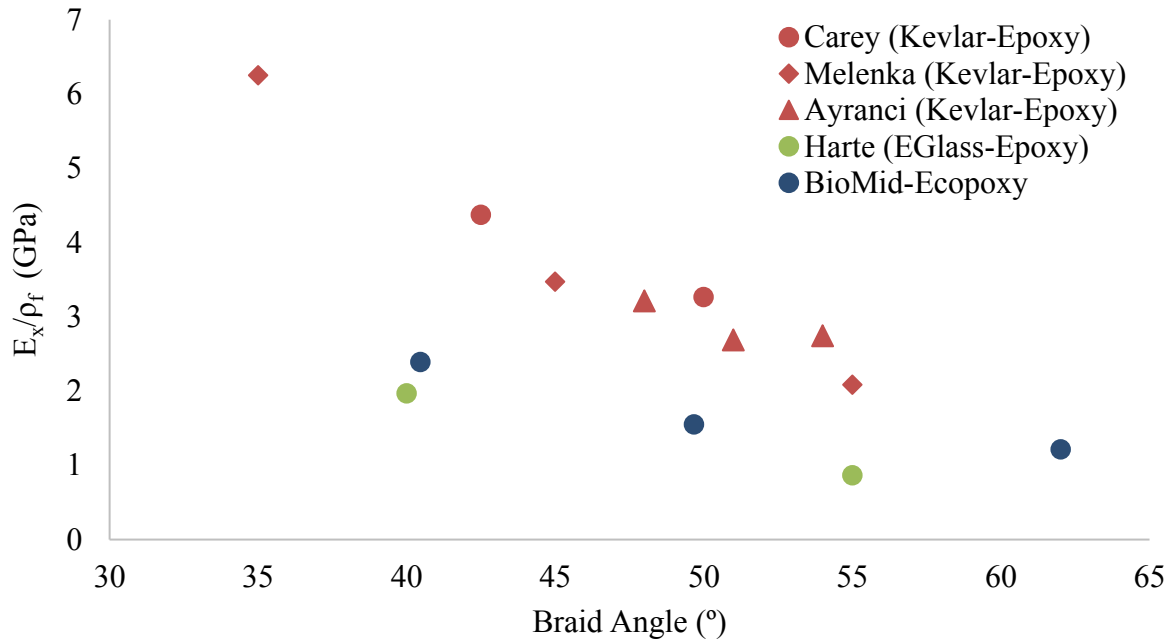


Figure 4-20. Scatterplot showing the comparison of the ratio of longitudinal elastic modulus over density of the reinforcing fiber

Since Kevlar is also very low in density, its specific properties are good. However, e-glass has a density of twice the BioMid® fibres. Therefore, it can be seen that the ratio of modulus over fiber density of BioMid braids is greater than the glass braids. As a result, the BioMid braided samples could be a viable option for e-glass fiber applications that would benefit from a reduction in mass.

4.4 Uncertainty

The sources of error in DIC occur both in the image acquisition stage as well as the image processing stage. During image acquisition, some possible sources of errors include non-uniform illumination of the sample, lens distortion or rigid body motion of the camera setup between calibration and testing [8].

During image processing, the correlation parameters were selected to minimize errors. Selecting a proper subset size is critical for obtaining correct displacement measurements. A subset that is too small may be high in uncertainty, while a subset that is too large may have low spatial resolution

[13]. Therefore, a balance must be achieved to achieve optimal accuracy and resolution. In addition, the correlation was performed relative to the first image, which increased the computation time but decreased the error in displacement measurements as the error was introduced during each cross-correlation separately and not propagated from image to image.

A basic uncertainty analysis was performed in order to estimate the error in the final calculation of elastic modulus. A summary of the methods and results are discussed in this section and the detailed uncertainty analysis is described in full in Appendix C.

The error in stress calculation was determined from estimating the sources of error in the load cell output and micrometer measurements used to determine the inner and outer diameters. The error in strain measurement was determined based on a study by Haddadi *et al.* [24] where rigid body motion was used to evaluate the accuracy of DIC strain measurement. In this study, an image of an undeformed sample was translated by incrementing number of pixels and the resulting image series was cross-correlated in DaVis. The strain in the displaced image should be zero, therefore the error was estimated as the strain output from the artificial displacement results. An error propagation analysis was performed to determine the total uncertainty estimated for calculating the elastic modulus as 1.06%.

4.5 Conclusions

Tubular braided composites were manufactured from 100% cellulose yarns and a high bio-content resin. Several different braid angles (fibre deposition direction) were manufactured to investigate the effect of braid angle on the tensile properties.

The samples were loaded in tension and the strain response was measured with imaging using a stereo digital image correlation setup to visualize the full-field deformation of each sample under testing. DaVis commercial software was used to process the image data into strain data and stress-

strain curves were determined. The elastic modulus was then derived from the numerical stress-strain data using the least squares regression method.

The elastic modulus decreased with an increase in braid angle. This trend would be expected as the smaller the braid angle, the closer the yarns are aligned with the longitudinal direction resulting in greater stiffness in tension. 4.20 GPa was the highest calculated value for elastic modulus for a measured braid angle of 39°, while 2.14 GPa was the smallest calculated value for elastic modulus for a measured braid angle of 59°. Through a high-level uncertainty analysis, the total uncertainty in the calculated values of elastic modulus with this method were determined to be 1.06%.

When compared with conventional synthetic materials, the elastic modulus of the BioMid® samples is less than that of e-glass fibers, however, they are also half as dense, making them excellent candidates for high stiffness to weight ratio applications.

4.6 References

- [1] R. Dunne, D. Desai, R. Sadiku, and J. Jayaramudu, “A review of natural fibres, their sustainability and automotive applications,” *J. Reinf. Plast. Compos.*, vol. 35, no. 13, pp. 1041–1050, Jul. 2016.
- [2] L. Mohammed, M. N. M. Ansari, G. Pua, M. Jawaid, and M. S. Islam, “A Review on Natural Fiber Reinforced Polymer Composite and Its Applications,” *Int. J. Polym. Sci.*, vol. 2015, pp. 15, Oct. 2015.
- [3] K. L. Pickering, M. G. A. Efendy, and T. M. Le, “A review of recent developments in natural fibre composites and their mechanical performance,” *Compos. Part Appl. Sci. Manuf.*, vol. 83, pp. 98–112, Apr. 2016.
- [4] A. Mohanty, M. Misra, and L. Drzal, Eds., *Natural Fibers, Biopolymers, and Biocomposites*. CRC Press, 2005.
- [5] A. K. Bledzki, A. Jaszkiwicz, and D. Scherzer, “Mechanical properties of PLA composites with man-made cellulose and abaca fibres,” *Compos. Part Appl. Sci. Manuf.*, vol. 40, no. 4, pp. 404–412, Apr. 2009.
- [6] D. Ray, *Biocomposites for High-Performance Applications: Current Barriers and Future Needs Towards Industrial Development*. Woodhead Publishing, 2017.
- [7] “Standard Test Method for Tensile Properties of Polymer Matrix Composite Materials,” *ASTM International*, D 3039, Oct. 2017.

- [8] Sutton, Michael A., Jean Jose Orteu, and Hubert Schreier, *Image Correlation for Shape, Motion and Deformation Measurements: Basic Concepts, Theory and Applications*. Springer Science & Business Media, 2009.
- [9] H. B. Motra, J. Hildebrand, and A. Dimmig-Osburg, "Assessment of strain measurement techniques to characterise mechanical properties of structural steel," *Eng. Sci. Technol. Int. J.*, vol. 17, no. 4, pp. 260–269, Dec. 2014.
- [10] C. Ayranci and J. P. Carey, "Predicting the longitudinal elastic modulus of braided tubular composites using a curved unit-cell geometry," *Compos. Part B Eng.*, vol. 41, no. 3, pp. 229–235, Apr. 2010.
- [11] G. W. Melenka and J. P. Carey, "Experimental analysis of diamond and regular tubular braided composites using three-dimensional digital image correlation," *J. Compos. Mater.*, pp. 3887-3907, Jan. 2017.
- [12] C. Ayranci and J. Carey, "2D braided composites: A review for stiffness critical applications," *Compos. Struct.*, vol. 85, no. 1, pp. 43–58, Sep. 2008.
- [13] StrainMaster, Davis 8.2 Product-Manual, *LA Vision*, March 2014.
- [14] A. J. Hunt and J. P. Carey, "Towards the development of a machine vision system for tubular braided composite materials," *International SAMPE Technical Conference*, 2016, vol. Jan. 2016.
- [15] C. Ayranci and J. P. Carey, "Experimental validation of a regression-based predictive model for elastic constants of open mesh tubular diamond-braid composites," *Polym. Compos.*, vol. 32, no. 2, pp. 243–251.
- [16] C. K. Leung, G. W. Melenka, D. S. Nobes, and J. P. Carey, "The effect on elastic modulus of rigid-matrix tubular composite braid radius and braid angle change under tensile loading," *Compos. Struct.*, vol. 100, pp. 135–143, 2013.
- [17] A. M. Harte and N. A. Fleck, "On the mechanics of braided composites in tension," *Eur. J. Mech. - ASolids*, vol. 19, no. 2, pp. 259–275, Mar. 2000.
- [18] G. W. Melenka and J. P. Carey, "Development of a generalized analytical model for tubular braided-architecture composites," *J. Compos. Mater.*, pp. 3861-3875, Jan. 2017.
- [19] J. H. Byun, "The analytical characterization of 2-D braided textile composites," *Compos. Sci. Technol.*, vol. 60, no. 5, pp. 705–716, Apr. 2000.
- [20] Z. T. Kier, A. Salvi, G. Theis, A. M. Waas, and K. Shahwan, "Estimating mechanical properties of 2D triaxially braided textile composites based on microstructure properties," *Compos. Part B Eng.*, vol. 68, pp. 288–299, Jan. 2015.
- [21] I. I. Qamhia, S. S. Shams, and R. F. El-Hajjar, "Quasi-Isotropic Triaxially Braided Cellulose-Reinforced Composites," *Mech. Adv. Mater. Struct.*, vol. 22, no. 12, pp. 988–995, Dec. 2015.
- [22] L. Xu, S. J. Kim, C.-H. Ong, and S. K. Ha, "Prediction of material properties of biaxial and triaxial braided textile composites," *J. Compos. Mater.*, vol. 46, no. 18, pp. 2255–2270, Aug. 2012.

- [23] J. Carey, M. Munro, and A. Fahim, “Longitudinal elastic modulus prediction of a 2-D braided fiber composite,” *J. Reinf. Plast. Compos.*, vol. 22, no. 9, pp. 813–831, 2003.
- [24] H. Haddadi and S. Belhabib, “Use of rigid-body motion for the investigation and estimation of the measurement errors related to digital image correlation technique,” *Optics and Lasers in Engineering*, vol. 46, pp. 185-196, February 2008.

Chapter 5 Conclusions and Future Work

5.1 Conclusions

Tubular braided composites are conventionally fabricated with synthetic materials such as Kevlar, glass or carbon fibres, impregnated with epoxy or other synthetic resins. However, they may also be fabricated from bio-based sources that are renewable and more environmentally friendly. In this work, braid preform samples were manufactured at three braid angles (40°, 50° and 60°) with naturally derived materials (BioMid® cellulose fibre reinforcement in Ecopoxy high bio-content resin matrix). The samples were studied and tested to determine whether these materials were capable of producing strong and consistent composite structures.

The microstructures of the samples were examined using micro-computed tomography (μ CT) imaging to determine the void content and fibre volume fraction. Since these constituents have not been used together in a composite in available literature, it was important to investigate the interaction of the materials at the micro-structural level to determine if the materials were capable of producing a composite material with a low content of voids and imperfections. Since voids can affect the integrity of the entire composite, a crucial step in developing new types of composite materials is quantifying the presence of voids and determining how to reduce them to produce a more reliable composite. This was the first study of its kind to successfully use μ CT imaging to investigate the effect of modifying braid angle, resin type, and curing method (vacuum bagging or open atmosphere) on fibre volume fraction, void volume and void distribution for braided composite materials. This method of estimating void, fibre and resin content was deemed to be superior to other methods such as acid digestion, matrix burn-off or microscopy since the location, distribution and size of voids along the entire length of the scanned sample could be both visualized and quantified. It was determined that void content increased with an increase in braid angle, and

vacuum bagging reduced the total void content. The commercial resin (Ecopoxy) was also determined to contain less voids than the hemp-based research lab resin. The results of this study demonstrated that μ CT imaging is a powerful tool in determining how to reduce the content of imperfections and produce more consistent composite materials.

The tensile elastic properties of the samples were determined by loading the samples in an MTS machine and measuring the strain response with stereo-digital image correlation. Due to the braided structure, there are regions along the braid that are between the interlaced yarns that contain a matrix with no reinforcement. In these regions, there are areas of strain concentration, resulting in a large variation of strain over the entire braid surface. Therefore, digital image correlation was used to determine the full field strain. Image data was obtained every 2 seconds during the tests while load data was acquired at a frequency of 100 Hz. Five samples were tested in tension at each braid angle to show the elastic modulus is affected by braid angle. It was determined that the maximum elastic modulus was 4.20 GPa for a 39° braid angle. The elastic modulus decreased as the braid angle was increased as the smaller braid angles has the reinforcing yarns more closely aligned to the longitudinal direction. At each desired braid angle, the measured braid angle had a deviation of up to 2.7° and the resulting calculated elastic modulus had a deviation of up to 0.28 GPa per desired braid angle.

The main contribution from this work is that it is possible to create high-quality composite braids that contain minimal voids and consistent mechanical properties with values for specific stiffness that could be greater than that of glass fibres. As a result, these braids could be ideal for high-stiffness to weight ratio applications.

5.2 Recommendations/Limitations

The procedure for fabricating the composite samples should be improved to better achieve consistent samples that are closer to the desired braid angle. In addition, a more precise measurement method should be used when applying the resin to ensure that the resin is spread consistently and evenly around the entire preform.

The computed tomography results are extremely sensitive to the processing procedure, particularly the selection of the greyscale threshold limits for resin, fibres and voids. The fibres and resin vary in density, allowing the user to perform segmentation. However, they are still fairly close in greyscale values leaving room for error when the user selects the limits. This could be improved by further optimizing the contrast between the fibres and matrix by adding an opaque penetrant to the resin so the user can more clearly distinguish the fibres and resin. A limitation of the computed tomography method is the large amount of data storage and RAM required, causing scanning and processing to be both storage and time intensive.

The digital image correlation process was set up with what was available for the lab. There are certain steps in the process that could be improved with more advanced technology was adequate, however it was very difficult to apply uniformly sized and distributed speckles onto the sample surface with this method. Considering that the results of the correlation are extremely sensitive to the speckle pattern it is likely this caused some error in the results. In addition, in order to adequately illuminate the sample for image capture, an LED light source was used, which sometimes caused reflection off the sample surface, which affected the image.

However, it must be noted that an error analysis showed that the experimental methods were very accurate.

5.3 Future Work

The results of this work are a preliminary feasibility analysis on the potential of these materials as reliable composite material constituents. There are a number of other studies to be performed to fully understand the behaviour of these materials and to better justify their adoption by the composite industry.

As far as manufacturing the samples for testing, an improved method is required to achieve the desired braid angle more precisely. Quality control measures could be in place throughout the fabrication process to pinpoint the steps which are causing the majority of the error to occur [78]. Additional mechanical tests should be performed to gain the full elastic properties. The braids should be tested in torsion to determine the shear properties and the Ecopoxy resin should be tested in tension to determine the matrix elastic properties as there is currently no properties available from the manufacturer. In addition, samples should be fabricated with multiple types of natural based resins and/or bonding agents and the fibre wetting and interfacial strength should be investigated to determine the optimal resin for cellulose fibres.

Several different factors could affect the integrity of the natural fibres composites. To investigate the durability of these composites under UV rays, an experiment should be performed by testing the samples before and after exposing the braids to UV radiation. To determine the effects of moisture absorption, a test should be performed according to test method ASTM D5229, by weighing the specimen before and after placing within an environment of 85% relative humidity. Several tests should be performed to investigate thermal effects. Differential scanning calorimetry should be used to determine the phase transition temperatures. The coefficient of thermal expansion should be determined based Test Method ASTM D696 for a range of -30° to 30° as this range represents the temperatures that these composites may be exposed to in typical use.

While it is known that these materials are derived from renewable materials, it is unknown how harmful it is to process these raw materials into a useful form. A full life cycle analysis should be performed to determine the emissions produced from raw form to disposal at the end of life. This should be compared with conventional synthetic materials to better quantify how large of a reduction the use of these braids in place of glass, etc. could have.

References

- [1] X. Huang and A. N. Netravali, "Environment-Friendly 'Green' Resins and Advanced Green Composites," in *Cellulose Based Composites*, J. P. Hinestroza and A. N. Netravali, Eds. Wiley-VCH Verlag GmbH & Co. KGaA, 2014, pp. 137–155.
- [2] K. L. Pickering, M. G. A. Efendy, and T. M. Le, "A review of recent developments in natural fibre composites and their mechanical performance," *Compos. Part Appl. Sci. Manuf.*, vol. 83, pp. 98–112, Apr. 2016.
- [3] H. Lilholt and J. M. Lawther, "1.10 - Natural Organic Fibers A2 - Kelly, Anthony," in *Comprehensive Composite Materials*, C. Zweben, Ed. Oxford: Pergamon, 2000, pp. 303–325.
- [4] D. Gay, S. Hoa, and S. Tsai, *Composite Materials: Design and Applications*. CRC Press, 2002.
- [5] C. Ayranci and J. Carey, "2D braided composites: A review for stiffness critical applications," *Compos. Struct.*, vol. 85, no. 1, pp. 43–58, Sep. 2008.
- [6] D. S. Mazumdar, D. Karthikeyan, D. Pichler, M. Benevento, and R. Frassine, "Composites Industry Report for 2017," *Composites Manufacturing Magazine*, 02-Jan-2017. [Online]. Available: <http://compositesmanufacturingmagazine.com/2017/01/composites-industry-report-2017/>. [Accessed: 26-Apr-2017].
- [7] Y. Wang, J. Li, and P. B. Do, "Properties of Composite Laminates Reinforced with E-Glass Multiaxial Non-Crimp Fabrics," *J. Compos. Mater.*, vol. 29, no. 17, pp. 2317–2333, Nov. 1995.
- [8] V. Çeçen, M. Sarikanat, H. Yildiz, and I. H. Tavman, "Comparison of mechanical properties of epoxy composites reinforced with stitched glass and carbon fabrics: Characterization of mechanical anisotropy in composites and investigation on the interaction between fiber and epoxy matrix," *Polym. Compos.*, vol. 29, no. 8, pp. 840–853, Aug. 2008.
- [9] J. P. Carey, *Handbook of Advances in Braided Composite Materials: Theory, Production, Testing and Applications*, Woodhead Publishing, 2016.
- [10] G. W. Melenka and J. P. Carey, "Experimental analysis of diamond and regular tubular braided composites using three-dimensional digital image correlation," *J. Compos. Mater.*, pp. 3887-3907, Jan. 2017.
- [11] A. P. Mouritz, M. K. Bannister, P. J. Falzon, and K. H. Leong, "Review of applications for advanced three-dimensional fibre textile composites," *Compos. Part Appl. Sci. Manuf.*, vol. 30, no. 12, pp. 1445–1461, Dec. 1999.
- [12] F. Vilaplana, E. Strömberg, and S. Karlsson, "Environmental and resource aspects of sustainable biocomposites," *Polym. Degrad. Stab.*, vol. 95, no. 11, pp. 2147–2161, Nov. 2010.
- [13] P. L. Menezes, P. K. Rohatgi, and M. R. Lovell, "Tribology of Natural Fiber Reinforced Polymer Composites," pp. 341–343, Jan. 2011.

- [14] R. Dunne, D. Desai, R. Sadiku, and J. Jayaramudu, "A review of natural fibres, their sustainability and automotive applications," *J. Reinf. Plast. Compos.*, vol. 35, no. 13, pp. 1041–1050, Jul. 2016.
- [15] L. Mwaikambo, "Tensile properties of alkalised jute fibres," *Materials Science and Technology*, vol. 25, pp. 1289-1295, Jul 2009.
- [16] A. K. Bledzki and J. Gassan, "Composites reinforced with cellulose based fibres," *Prog. Polym. Sci.*, vol. 24, no. 2, pp. 221–274, May 1999.
- [17] T. Huber, J. Müssig, O. Curnow, S. Pang, S. Bickerton, and M. P. Staiger, "A critical review of all-cellulose composites," *J. Mater. Sci.*, vol. 47, no. 3, pp. 1171–1186, 2012.
- [18] J.-C. Zarges, C. Kaufhold, M. Feldmann, and H.-P. Heim, "Single fiber pull-out test of regenerated cellulose fibers in polypropylene: An energetic evaluation," *Compos. Part Appl. Sci. Manuf.*, vol. 105, pp. 19–27, Feb. 2018.
- [19] A. Mohanty, M. Misra, and L. Drzal, Eds., *Natural Fibers, Biopolymers, and Biocomposites*. CRC Press, 2005.
- [20] N. Shikamoto, P. Wongsriraksa, A Ohtani, L Y Wei and A Nakai. "Processing and mechanical properties of biodegradable composites." *The 9th International Conference on Flow Processes in Composite Materials*, Jul 2008.
- [21] C. Taylor, A. Amiri, A. Paramarta, C. Ulven, and D. Webster, "Development and weatherability of bio-based composites of structural quality using flax fiber and epoxidized sucrose soyate," *Mater. Des.*, vol. 113, pp. 17–26, 2017.
- [22] A. Couture, G. Lebrun, and L. Laperrière, "Mechanical properties of polylactic acid (PLA) composites reinforced with unidirectional flax and flax-paper layers," *Compos. Struct.*, vol. 154, pp. 286–295, 2016.
- [23] W. Li, Y. Zheng, L. Zhang, Z. Ou, and J. Zhou, "Preparation and characterization of nano-SiO₂/lignin-phenol-starch composite resin," *Polymeric Mater. Sci. Eng.*, vol. 32, no. 5, pp. 23–27, 2016.
- [24] K. Oksman, M. Skrifvars, and J.-F. Selin, "Natural fibres as reinforcement in polylactic acid (PLA) composites," *Compos. Sci. Technol.*, vol. 63, no. 9, pp. 1317–1324, Jul. 2003.
- [25] R. Aurus, L. Lim, S. Selke, H. Tsuji, *Poly (Lactic Acid): Synthesis, Structures, Properties, Processing, and Applications*, John Wiley and Sons, 2010.
- [26] P. Uawongsuwan et al., *Mechanical properties of poly (Lactic acid) based biocomposites: Comparison of different reinforcements*, vol. 2. 2013.
- [27] A. K. Bledzki, A. Jaszkiwicz, and D. Scherzer, "Mechanical properties of PLA composites with man-made cellulose and abaca fibres," *Compos. Part Appl. Sci. Manuf.*, vol. 40, no. 4, pp. 404–412, Apr. 2009.

- [28] Sicomin Epoxy Systems, *SR GreenPoxy 56 Clear Epoxy Resin Technical Datasheet*, Sicomin, 2015.
- [29] One High Bio-Content Resin, *Super Sap One System Technical Data Sheet*, Entropy Resins, 2015.
- [30] Ecopoxy, *Ecopoxy Resin and Clear Hardener Technical Data Sheet*, Ecopoxy, 2016.
- [31] M. Feldmann and A. K. Bledzki, “Bio-based polyamides reinforced with cellulosic fibres – Processing and properties,” *Compos. Sci. Technol.*, vol. 100, pp. 113–120, Aug. 2014.
- [32] A. Espert, F. Vilaplana, and S. Karlsson, “Comparison of water absorption in natural cellulosic fibres from wood and one-year crops in polypropylene composites and its influence on their mechanical properties,” *Compos. Part Appl. Sci. Manuf.*, vol. 35, no. 11, pp. 1267–1276, Nov. 2004.
- [33] L. Yan, N. Chouw, and K. Jayaraman, “Effect of UV and water spraying on the mechanical properties of flax fabric reinforced polymer composites used for civil engineering applications,” *Mater. Des.*, vol. 71, pp. 17–25, Apr. 2015.
- [34] C. S. Korach and F.-P. Chiang, “Characterization of carbon fiber-vinylester composites exposed to combined uv radiation and salt spray,” *ECCM 2012 - Compos. Venice Proc. 15th Eur. Conf. Compos. Mater.*, Jan. 2012.
- [35] J. Sousa, J. R. Correia, S. Cabral-Fonseca, “Durability of Glass Fibre Reinforced Polymer Pultruded Profiles: Comparison Between QUV Accelerated Exposure and Natural Weathering in a Mediterranean Climate,” *Experimental Techniques*, February 2016.
- [36] B. G. Kumar, R. P. Singh, and T. Nakamura, “Degradation of Carbon Fiber-Reinforced Epoxy Composites by Ultraviolet Radiation and Condensation,” *J. Compos. Mater.*, vol. 36, no. 24, pp. 2713–2733, Dec. 2002.
- [37] A. U. R. Shah, M. N. Prabhakar, and J.-I. Song, “Current advances in the fire retardancy of natural fiber and bio-based composites – A review,” *Int. J. Precis. Eng. Manuf. - Green Technol.*, vol. 4, no. 2, pp. 247–262, 2017.
- [38] K. A. Salmeia et al., “Flammability of Cellulose-Based Fibers and the Effect of Structure of Phosphorus Compounds on Their Flame Retardancy,” *Polymers*, vol. 8, no. 8, p. 293, Aug. 2016.
- [39] N. K. Kim, S. Dutta, and D. Bhattacharyya, “A review of flammability of natural fibre reinforced polymeric composites,” *Compos. Sci. Technol.*, vol. 162, pp. 64–78, Jul. 2018.
- [40] M. Kamaya, A. Nakai, E. Fukui, and H. Hamada, “Micro-braided yarn as intermediate material system for continues fiber reinforced thermoplastic composite,” *13th International Conference on Composite Materials*, August 2001.
- [41] O. Faruk, A. K. Bledzki, H.-P. Fink, and M. Sain, “Biocomposites reinforced with natural fibers: 2000–2010,” *Prog. Polym. Sci.*, vol. 37, no. 11, pp. 1552–1596, Nov. 2012.

- [42] T. Huber et al., “Three-dimensional braiding of continuous regenerated cellulose fibres,” *J. Ind. Text.*, vol. 45, no. 5, pp. 707–715, 2016.
- [43] I. I. Qamhia, S. S. Shams, and R. F. El-Hajjar, “Quasi-Isotropic Triaxially Braided Cellulose-Reinforced Composites,” *Mech. Adv. Mater. Struct.*, vol. 22, no. 12, pp. 988–995, Dec. 2015.
- [44] M. M. Kabir, H. Wang, K. T. Lau, and F. Cardona, “Chemical treatments on plant-based natural fibre reinforced polymer composites: An overview,” *Compos. Part B Eng.*, vol. 43, no. 7, pp. 2883–2892, Oct. 2012.
- [45] L. Yan, N. Chouw, and K. Jayaraman, “Flax fibre and its composites – A review,” *Compos. Part B Eng.*, vol. 56, pp. 296–317, Jan. 2014.
- [46] G. Lebrun, A. Couture, and L. Laperrière, “Tensile and impregnation behavior of unidirectional hemp/paper/epoxy and flax/paper/epoxy composites,” *Compos. Struct.*, vol. 103, pp. 151–160, 2013.
- [47] E. Ameri, L. Laperrière, and G. Lebrun, “Mechanical characterization and optimization of a new unidirectional flax/paper/epoxy composite,” *Compos. Part B Eng.*, vol. 97, pp. 282–291, 2016.
- [48] N. Soykeabkaew, N. Arimoto, T. Nishino, and T. Peijs, “All-cellulose composites by surface selective dissolution of aligned ligno-cellulosic fibres,” *Compos. Sci. Technol.*, vol. 68, no. 10–11, pp. 2201–2207, Aug. 2008.
- [49] S. Kalka, T. Huber, J. Steinberg, K. Baronian, J. Müssig, and M. P. Staiger, “Biodegradability of all-cellulose composite laminates,” *Compos. Part Appl. Sci. Manuf.*, vol. 59, pp. 37–44, 2014.
- [50] J. W. Dormanns, J. Schuermann, J. Müssig, B. J. C. Duchemin, and M. P. Staiger, “Solvent infusion processing of all-cellulose composite laminates using an aqueous NaOH/urea solvent system,” *Compos. Part Appl. Sci. Manuf.*, vol. 82, pp. 130–140, Mar. 2016.
- [51] X. Chen, J. Chen, T. You, K. Wang, and F. Xu, “Effects of polymorphs on dissolution of cellulose in NaOH/urea aqueous solution,” *Carbohydr. Polym.*, vol. 125, pp. 85–91, Jul. 2015.
- [52] T. Nishino, I. Matsuda, and K. Hirao, “All-cellulose composite,” *Macromolecules*, vol. 37, no. 20, pp. 7683–7687, 2004.
- [53] D. Ray, *Biocomposites for High-Performance Applications: Current Barriers and Future Needs Towards Industrial Development*. Woodhead Publishing, 2017.
- [54] Y. A. Gowayed, “The Effect of Voids on the Elastic Properties of Textile Reinforced Composites,” *J. Compos. Technol. Res.*, vol. 19, no. 3, pp. 168–173, 1997.
- [55] “Manual for Bruker-microCT CT-Analyser v. 1.13,” vol. 1, p. 139, 2013.
- [56] K. K. Chawla, “Micromechanics of Composites,” in *Composite Materials*, Springer, New York, NY, 2012, pp. 337–385.

- [57] J. E. Little, X. Yuan, and M. I. Jones, “Characterisation of voids in fibre reinforced composite materials,” *NDT E Int.*, vol. 46, no. 1, pp. 122–127, 2012.
- [58] J. S. U. Schell, M. Renggli, G. H. van Lenthe, R. Müller, and P. Ermanni, “Micro-computed tomography determination of glass fibre reinforced polymer meso-structure,” *Compos. Sci. Technol.*, vol. 66, no. 13, pp. 2016–2022, Oct. 2006.
- [59] G. W. Melenka, E. Lepp, B. K. O. Cheung, and J. P. Carey, “Micro-computed tomography analysis of tubular braided composites,” *Compos. Struct.*, vol. 131, no. Supplement C, pp. 384–396, Nov. 2015.
- [60] D. Zhang, D. Heider, and J. John W Gillespie, “Void reduction of high-performance thermoplastic composites via oven vacuum bag processing,” *J. Compos. Mater.*, vol. 51, no. 30, pp. 4219–4230, Dec. 2017.
- [61] D. Zhang, D. Heider, and J. W. Gillespie, “Determination of void statistics and statistical representative volume elements in carbon fiber-reinforced thermoplastic prepregs,” *J. Thermoplast. Compos. Mater.*, vol. 30, no. 8, pp. 1103–1119, Aug. 2017.
- [62] I. Straumit, S. V. Lomov, N. Q. Nguen, and M. Wevers, “From a micro-CT image to models of the internal geometry, defects, micromechanics and permeability of textile composites - VoxTex software,” *ECCM 2016 - Proceeding of the 17th European Conference on Composite Materials*, 2016.
- [63] Composites World, “New cellulose-based fiber,” Oct. 2012. [Online]. Available: <http://www.compositesworld.com/products/new-cellulose-based-fiber>. [Accessed: 12-Sep-2017].
- [64] T. S. Omonov, E. Kharraz, and J. M. Curtis, “The epoxidation of canola oil and its derivatives,” *RSC Adv.*, vol. 6, no. 95, pp. 92874–92886, Sep. 2016.
- [65] T. Omonov and J. Curtis, “Aldehyde Free Thermoset Bioresins and Biocomposites,” U.S. Patent, 14/442458, July 28 2016.
- [66] G. W. Melenka and J. P. Carey, “Development of a generalized analytical model for tubular braided-architecture composites,” *J. Compos. Mater.*, pp. 3861-3875, Jan. 2017.
- [67] J. Hsieh, *Computed Tomography: Principles, Design, Artifacts, and Recent Advances*, 3rd Edition, Spie Press, Oct. 2015.
- [68] F. E. Boas and D. Fleischmann, “CT artifacts: Causes and reduction techniques,” *Imaging Med.*, vol. 4, no. 2, pp. 229–240, 2012.
- [69] J. Chen, T.M. McBride, S.B. Sanchez, “Sensitivity of Mechanical Properties to Braid Misalignment in Triaxial Braid Composite Panels,” *Journal of Composites Science and Technology*, vol. 20, pp. 13-17, Jan. 1998.
- [70] J. Dong and Y. Gong, “Influence of void defects on progressive tensile damage of three-dimensional braided composites,” *J. Compos. Mater.*, pp. 2033-2045, Oct. 2017.

- [71] J. Summerscales, *Non-Destructive Testing of Fibre-Reinforced Plastics Composites*. Springer Science & Business Media, 1987.
- [72] L. Mohammed, M. N. M. Ansari, G. Pua, M. Jawaid, and M. S. Islam, “A Review on Natural Fiber Reinforced Polymer Composite and Its Applications,” *Int. J. Polym. Sci.*, vol. 2015, pp. 15, Oct. 2015.
- [73] “Standard Test Method for Tensile Properties of Polymer Matrix Composite Materials,” *ASTM International*, D 3039, Oct. 2017.
- [74] Sutton, Michael A., Jean Jose Orteu, and Hubert Schreier, *Image Correlation for Shape, Motion and Deformation Measurements: Basic Concepts, Theory and Applications*. Springer Science & Business Media, 2009.
- [75] H. B. Motra, J. Hildebrand, and A. Dimmig-Osburg, “Assessment of strain measurement techniques to characterise mechanical properties of structural steel,” *Eng. Sci. Technol. Int. J.*, vol. 17, no. 4, pp. 260–269, Dec. 2014.
- [76] C. Ayranci and J. P. Carey, “Predicting the longitudinal elastic modulus of braided tubular composites using a curved unit-cell geometry,” *Compos. Part B Eng.*, vol. 41, no. 3, pp. 229–235, Apr. 2010.
- [77] StrainMaster, Davis 8.2 Product-Manual, *LA Vision*, March 2014.
- [78] A. J. Hunt and J. P. Carey, “Towards the development of a machine vision system for tubular braided composite materials,” *International SAMPE Technical Conference*, 2016, vol. Jan. 2016.
- [79] C. Ayranci and J. P. Carey, “Experimental validation of a regression-based predictive model for elastic constants of open mesh tubular diamond-braid composites,” *Polym. Compos.*, vol. 32, no. 2, pp. 243–251.
- [80] C. K. Leung, G. W. Melenka, D. S. Nobes, and J. P. Carey, “The effect on elastic modulus of rigid-matrix tubular composite braid radius and braid angle change under tensile loading,” *Compos. Struct.*, vol. 100, pp. 135–143, 2013.
- [81] A.-M. Harte and N. A. Fleck, “On the mechanics of braided composites in tension,” *Eur. J. Mech. - ASolids*, vol. 19, no. 2, pp. 259–275, Mar. 2000.
- [82] J.-H. Byun, “The analytical characterization of 2-D braided textile composites,” *Compos. Sci. Technol.*, vol. 60, no. 5, pp. 705–716, Apr. 2000.
- [83] Z. T. Kier, A. Salvi, G. Theis, A. M. Waas, and K. Shahwan, “Estimating mechanical properties of 2D triaxially braided textile composites based on microstructure properties,” *Compos. Part B Eng.*, vol. 68, pp. 288–299, Jan. 2015.
- [84] L. Xu, S. J. Kim, C.-H. Ong, and S. K. Ha, “Prediction of material properties of biaxial and triaxial braided textile composites,” *J. Compos. Mater.*, vol. 46, no. 18, pp. 2255–2270, Aug. 2012.

[85] J. Carey, M. Munro, and A. Fahim, “Longitudinal elastic modulus prediction of a 2-D braided fiber composite,” *J. Reinf. Plast. Compos.*, vol. 22, no. 9, pp. 813–831, 2003.

[86] H. Haddadi and S. Belhabib, “Use of rigid-body motion for the investigation and estimation of the measurement errors related to digital image correlation technique,” *Optics and Lasers in Engineering*, vol. 46, pp. 185-196, February 2008.

[87] R. Figliola and D. Beasley, *Theory and Design for Mechanical Measurements*, 6th Edition, Wiley, Jan 2015.

[88] “Standard Practices for Verification of Force Testing Machines,” ASTM International, E4-16, June 2016.

Appendix A Equipment Setup and Calibration

A.1 Braiding Machine

The braiding machine is programmed to operate at a certain picks per inch (PPI) where a pick is defined as the dimension L in Figure A-1. The following equations were used to determine which PPI settings to use to produce the desired braid angles (θ) where N is the total number of yarn carriers.

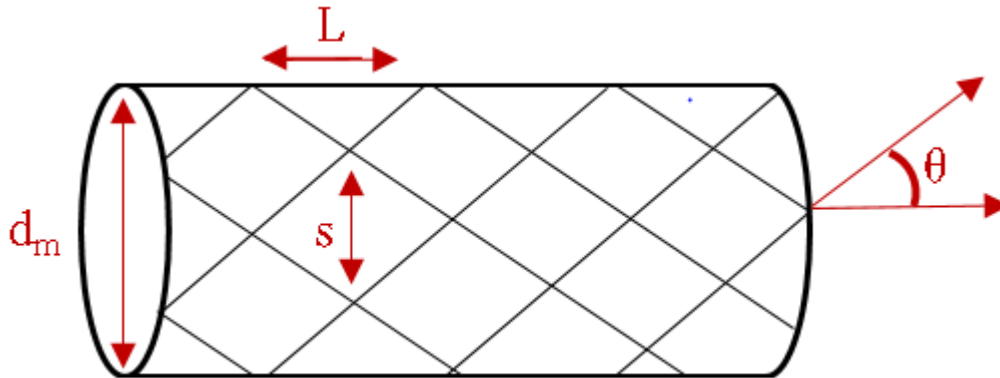


Figure A-1. Illustration of the parameters used to calculate braid angle based on the picks per inch (PPI)

$$s = \frac{\pi d_m}{N/2} \quad (\text{A.1})$$

$$L = PPI^{-1} \quad (\text{A.2})$$

$$\theta = \tan^{-1} \left(\frac{s}{L} \right) \quad (\text{A.3})$$

Table A-1. Calculated pick per inch setting on braiding machine to produce desired braid angles

Braid Angle (°)	PPI setting
30	13
40	18
50	25

A.2 MTS Machine

The DAQ recorded voltage data from the load cell. These voltage values were converted to load data according to A.4.

$$\text{load (N)} = \text{voltage} \left(\frac{\text{range of load}}{\text{range of voltage}} \right) * \text{magnification factor} - \text{offset} \quad (\text{A.4})$$

Load data was recorded at with zero load applied and a series of increasing standardized weights applied to determine the offset and magnification factor. Figure A-2 demonstrates a 1 kg load applied in order as shown in Figure A-2.

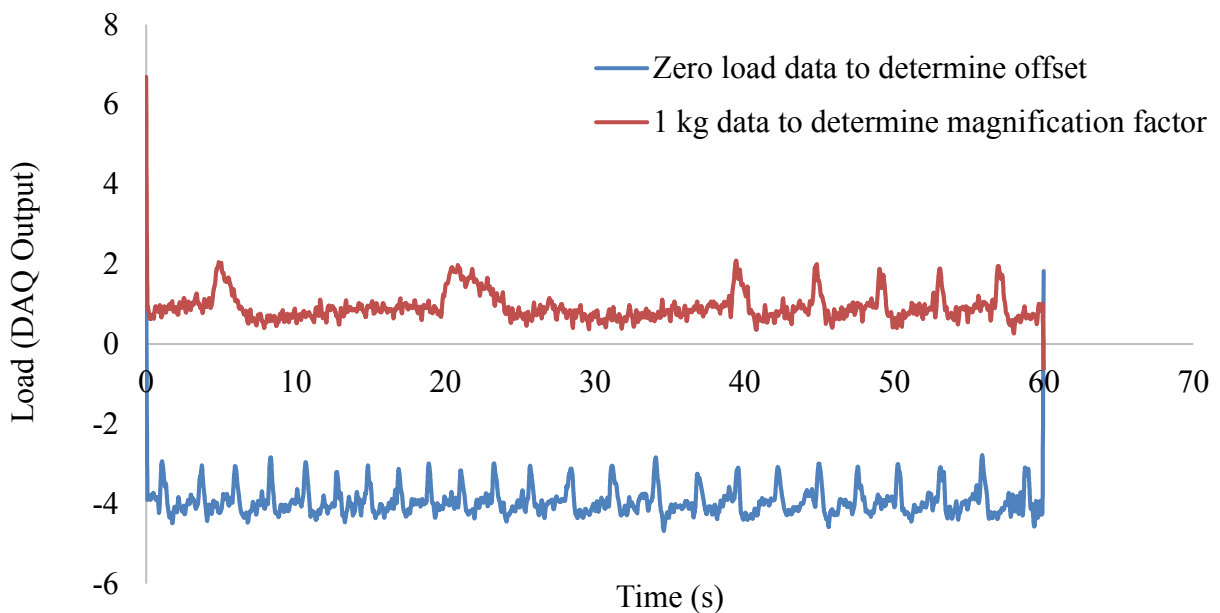


Figure A-2. Curves demonstrating the load calibration data

The magnification factors calculated for each of the masses are shown in Table A-2. The average used was 10.5 N/load output.

Table A-2. Magnification factor calibration

Mass (g)	Magnification Factor (N/load)
500	10.7
600	10.3
700	10.6
800	10.4
900	10.4
1000	10.7

The following Matlab code was used to filter all the load data by applying averaging in order to remove all phase distortion.

```
%plot original unfiltered data
plot(results(:,1),results(:,2), 'b');

%transfer function coefficient
b = ones(1,5000)/5000;

%for an all-zero filter input 1 for a
a = 1;

%input signal
x = results(:,2);

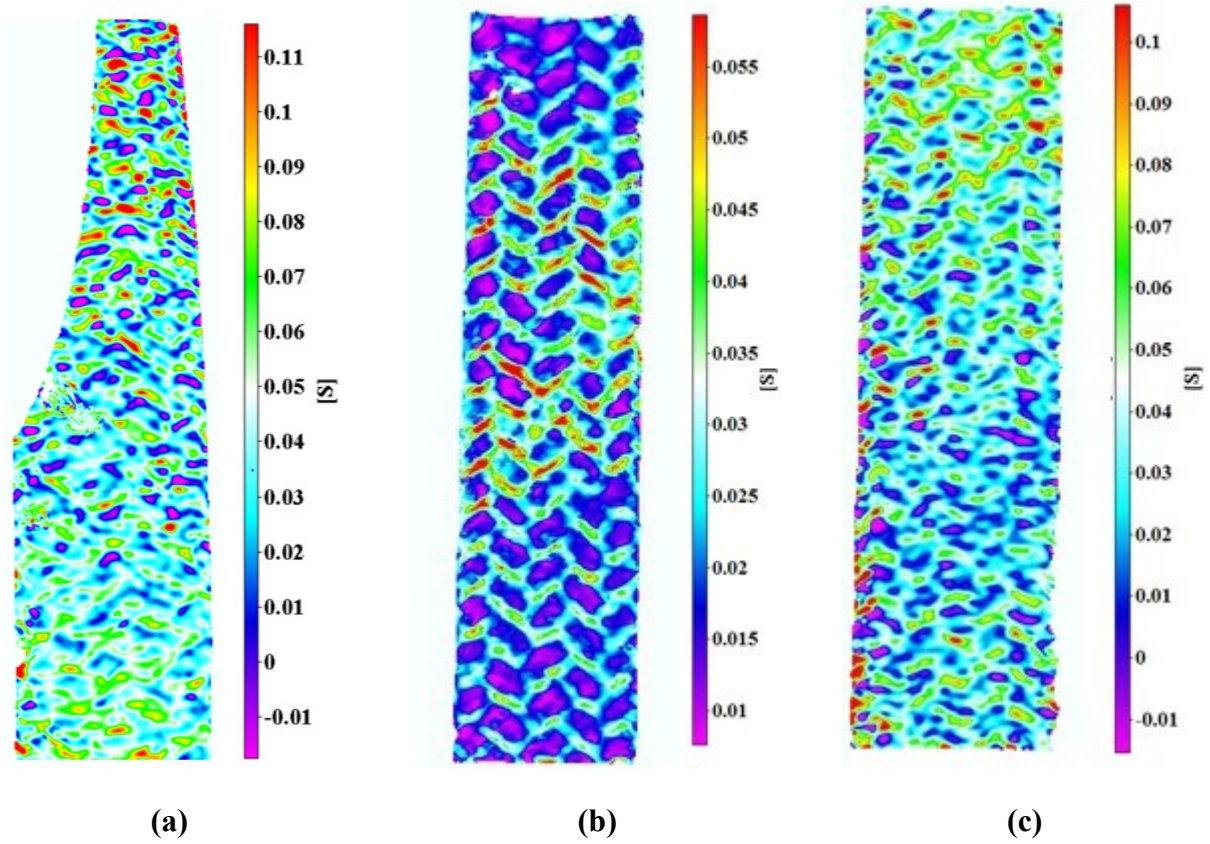
%evaluate filtered results by applying filtfilt
results_filt = filtfilt(a,1,x);

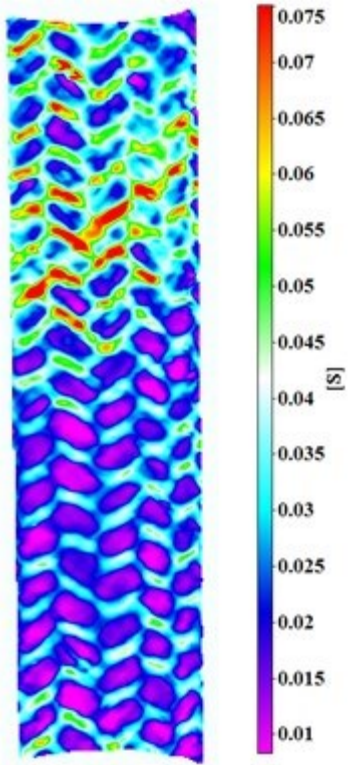
%plot curve with noise removed
plot(results(:,1),results_filt, 'r');
xlabel('time (s)');
ylabel('load (N)');
```

Appendix B Full Test Results

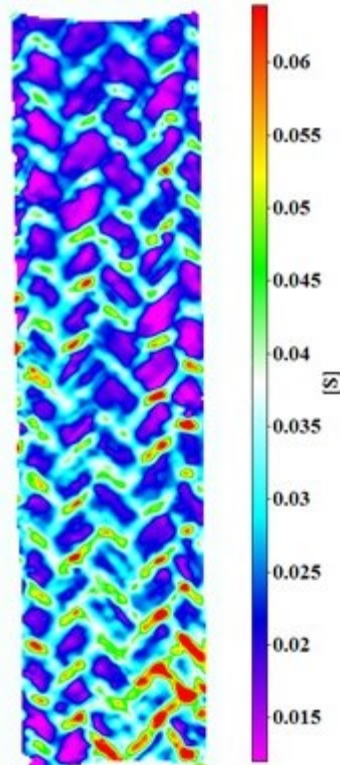
B.1 DIC Strain Fields

The stress-strain curves for all 15 samples plotted with the elastic modulus calculated by the least squares method described in Chapter 4 can be seen in Figure B-1.

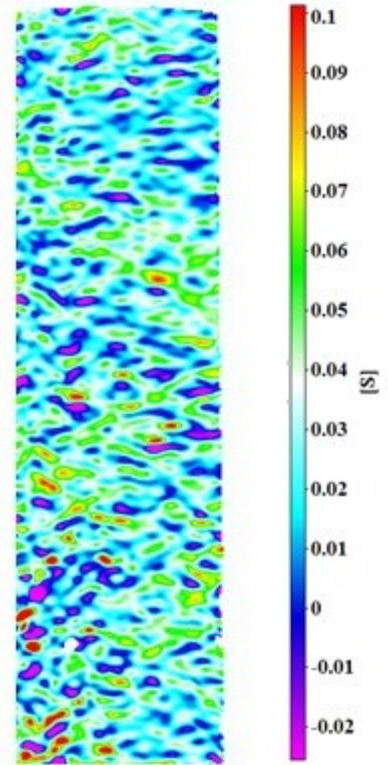




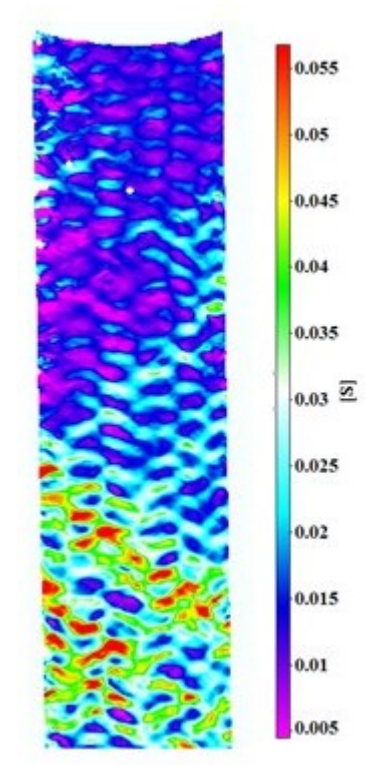
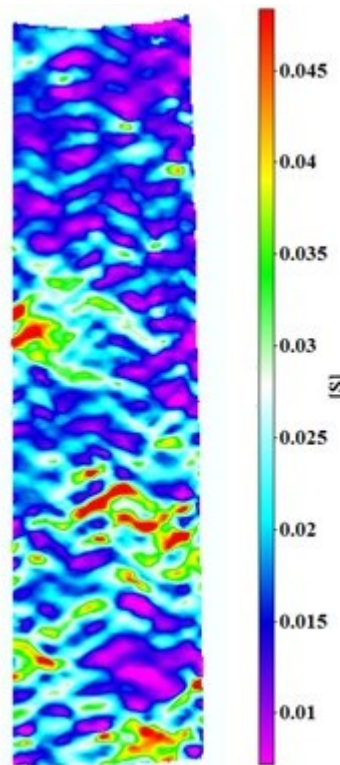
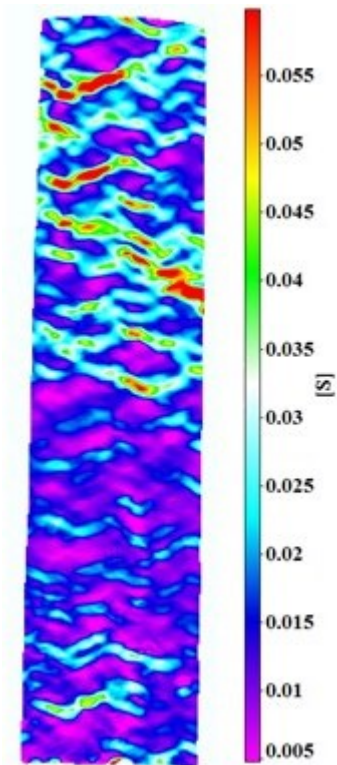
(d)



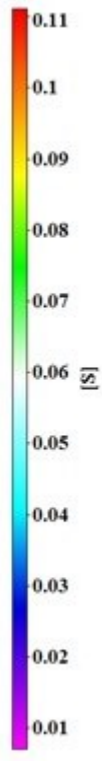
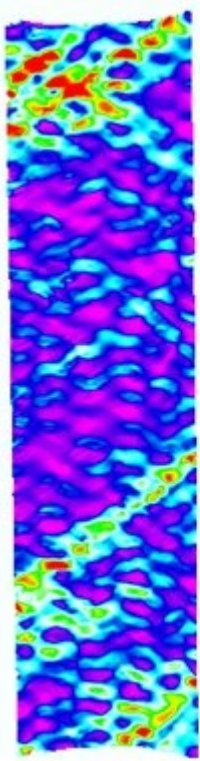
(e)



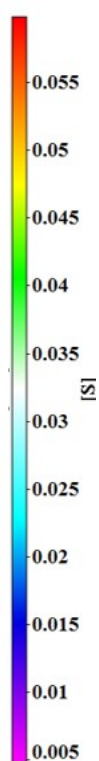
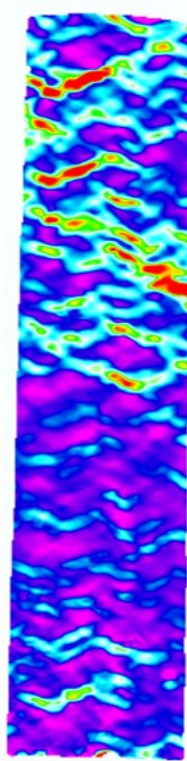
(f)



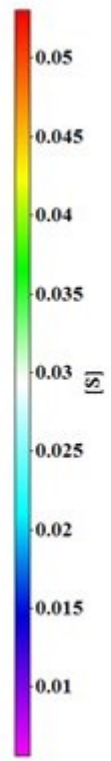
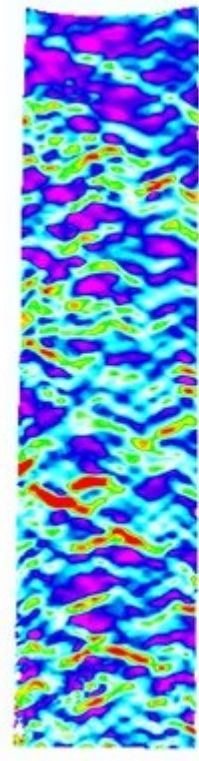
(g)



(h)



(i)



(j)

(k)

(l)

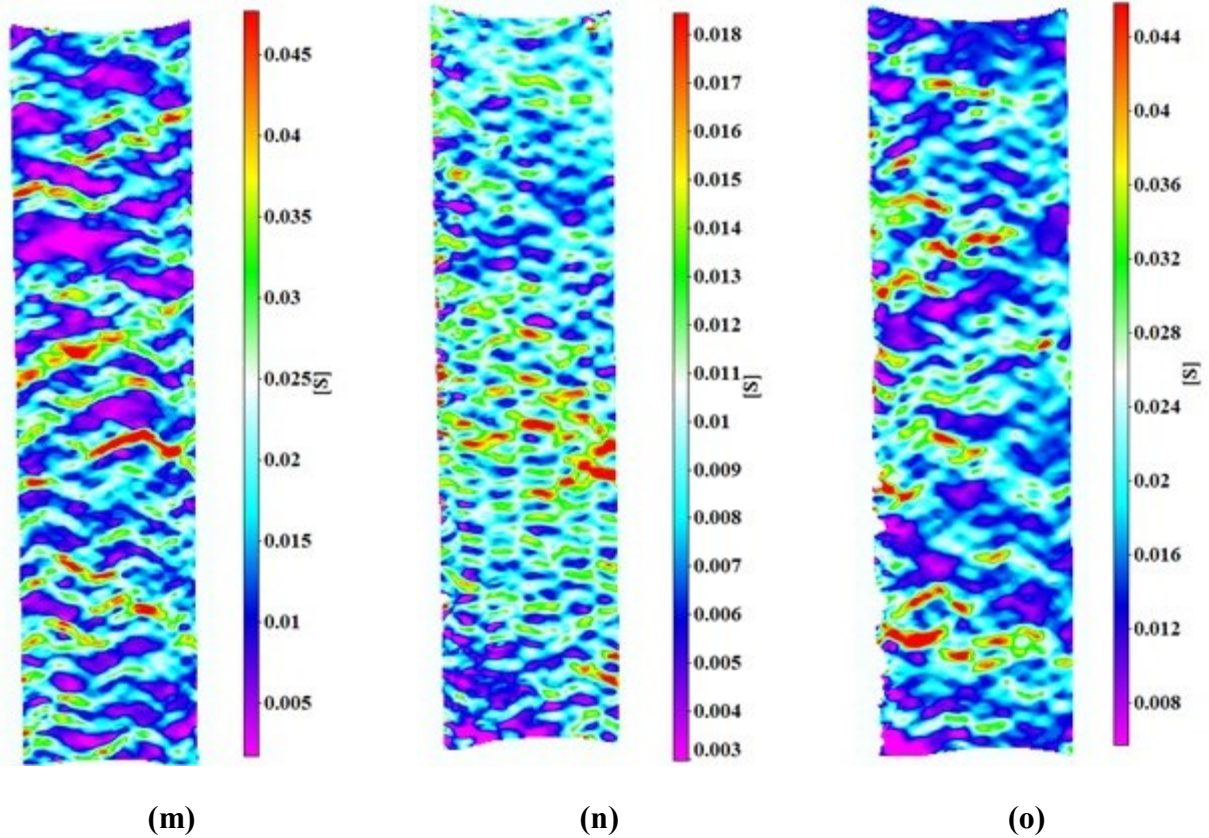


Figure B-3. DIC strain field at maximum stress for (a) sample 1 ($\sigma_{\max} = 53.3$ MPa), (b) sample 2 ($\sigma_{\max} = 46.0$ MPa), (c) sample 3 ($\sigma_{\max} = 53.0$ MPa), (d) sample 4 ($\sigma_{\max} = 51.4$ MPa), (e) sample 5 ($\sigma_{\max} = 45.9$ MPa), (f) sample 6 ($\sigma_{\max} = 28.1$ MPa), (g) sample 7 ($\sigma_{\max} = 24.3$ MPa), (h) sample 8 ($\sigma_{\max} = 21.0$ MPa), (i) sample 9 ($\sigma_{\max} = 19.6$ MPa), (j) sample 10 ($\sigma_{\max} = 29.3$ MPa), (k) sample 11 ($\sigma_{\max} = 9.48$ MPa), (l) sample 12 ($\sigma_{\max} = 14.9$ MPa), (m) sample 13 ($\sigma_{\max} = 9.70$ MPa), (n) sample 14 ($\sigma_{\max} = 14.3$ MPa) and (o) sample 15 ($\sigma_{\max} = 10.2$ MPa)

B.2 Stress-Strain Curves

The stress-strain curves for all 15 samples plotted with the elastic modulus calculated by the least squares method described in Chapter 4 can be seen in Figure B-6 to Figure B-18.

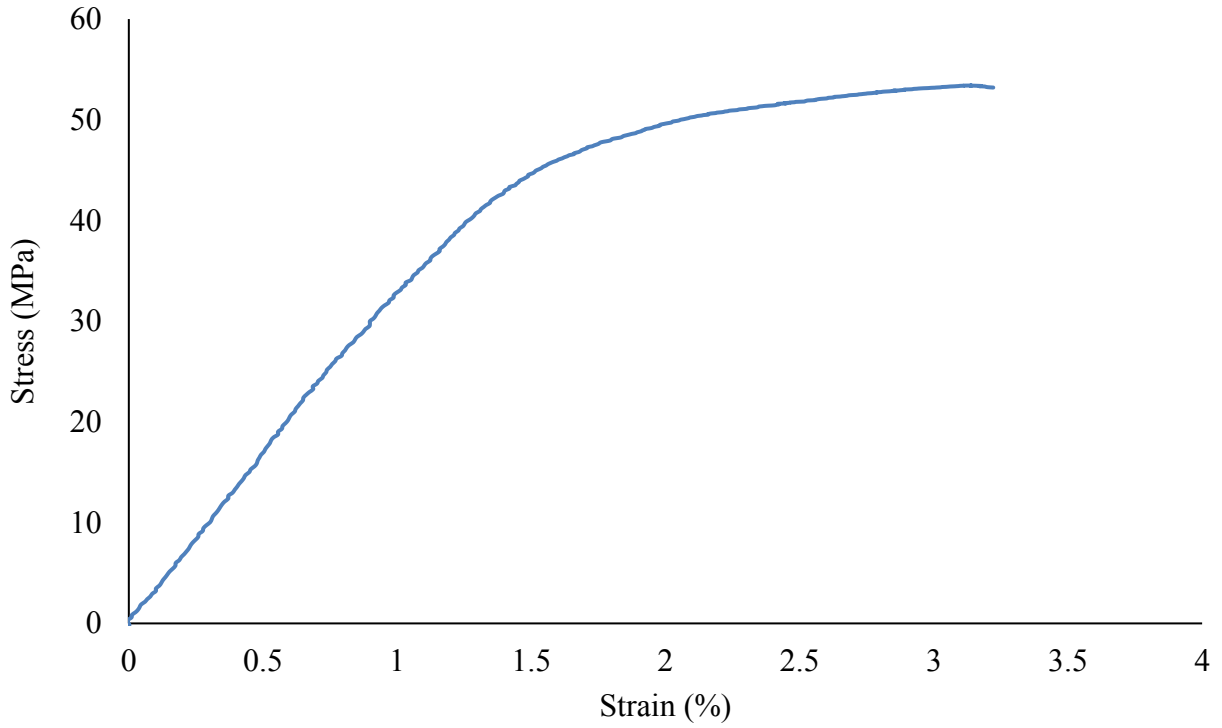


Figure B-4. Stress strain curve for sample 1 (E = 3.33 GPa)

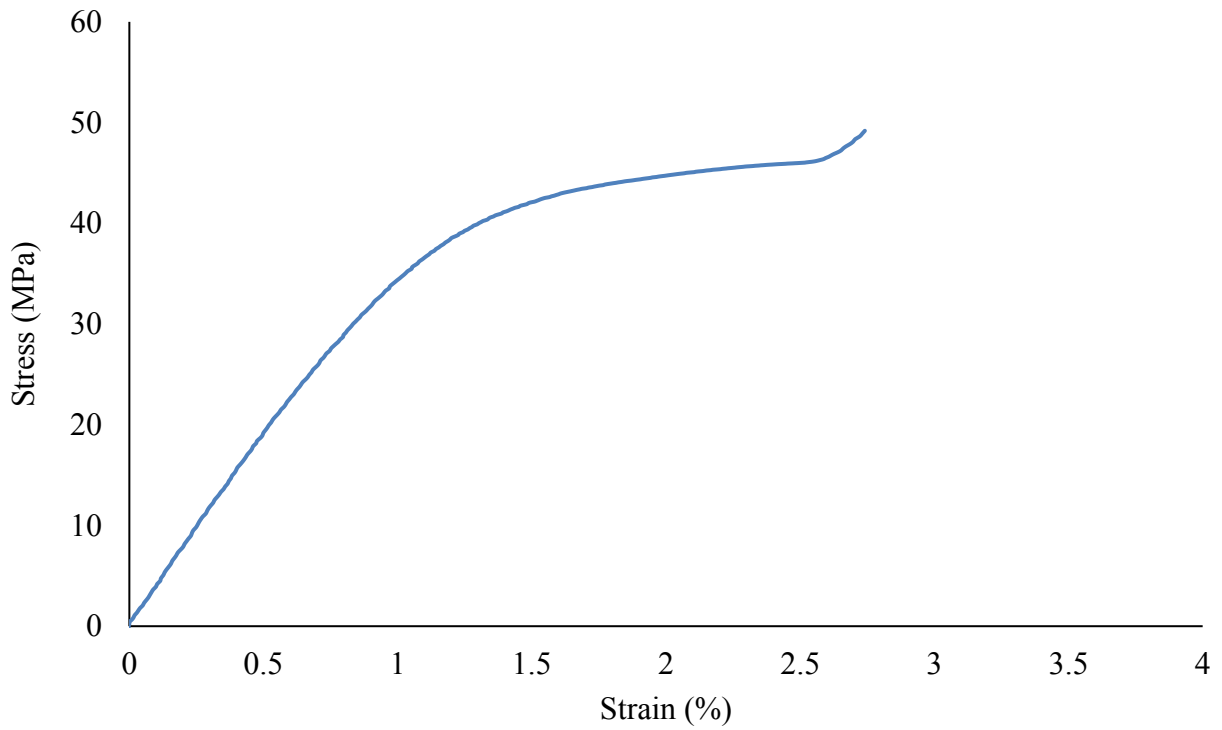


Figure B-5. Stress strain curve for sample 2 (E = 3.60 GPa)

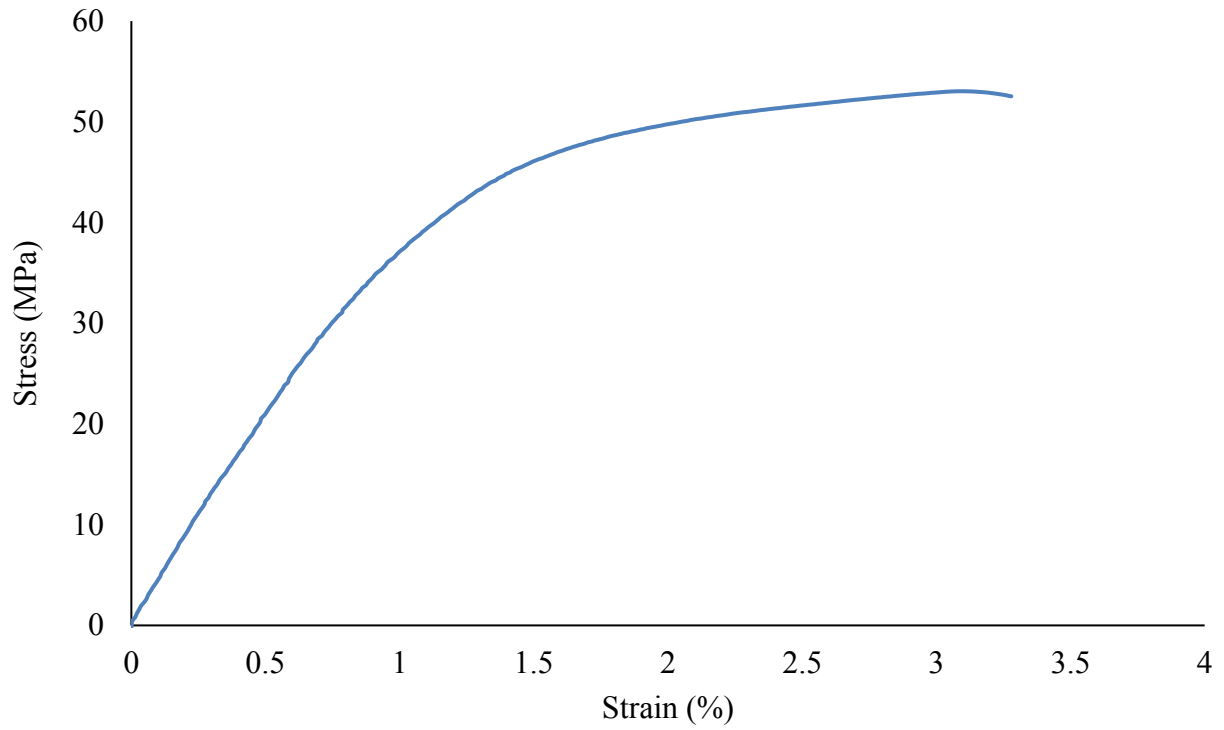


Figure B-6. Stress strain curve for sample 3 (E = 3.74 GPa)

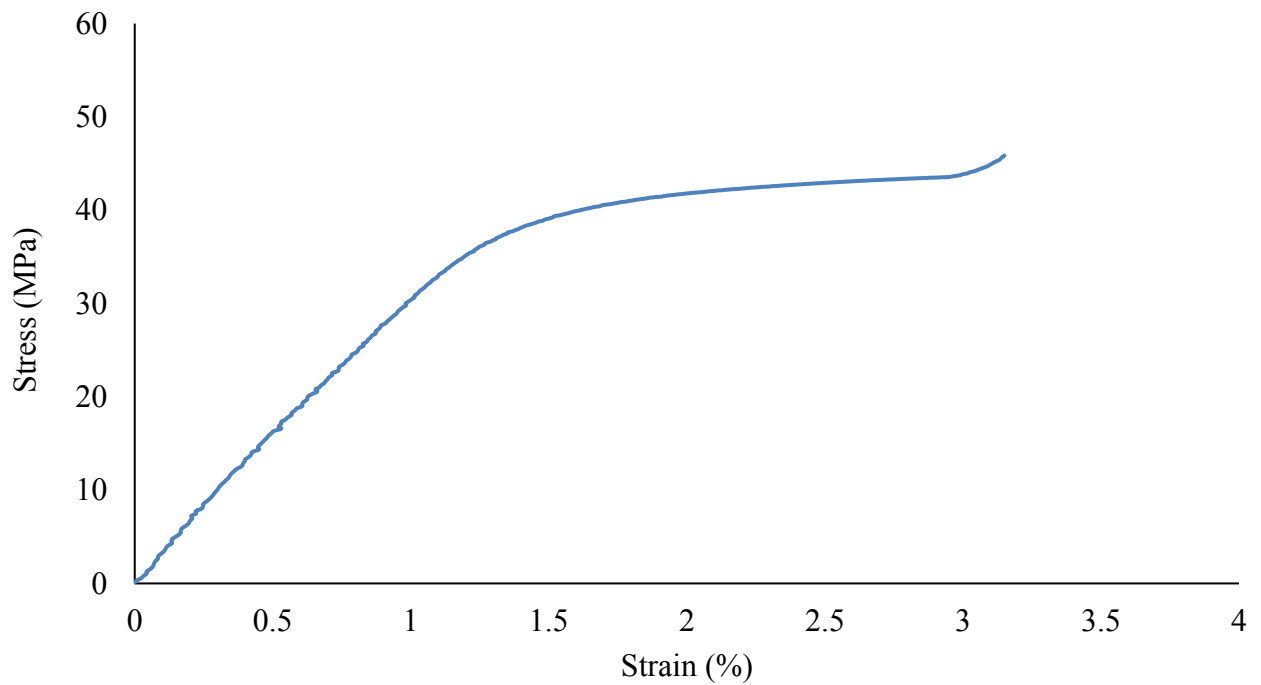


Figure B-7. Stress strain curve for sample 4 (E = 3.07 GPa)

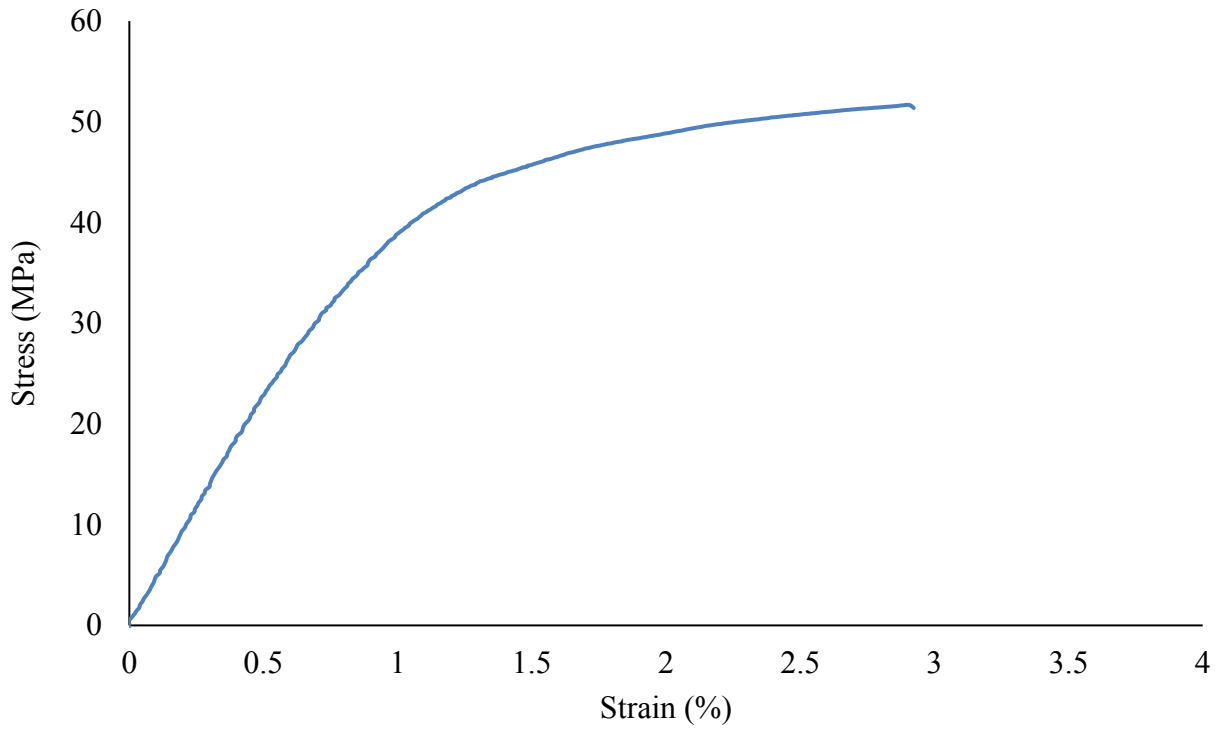


Figure B-8. Stress strain curve for sample 5 ($E = 4.20$ GPa)

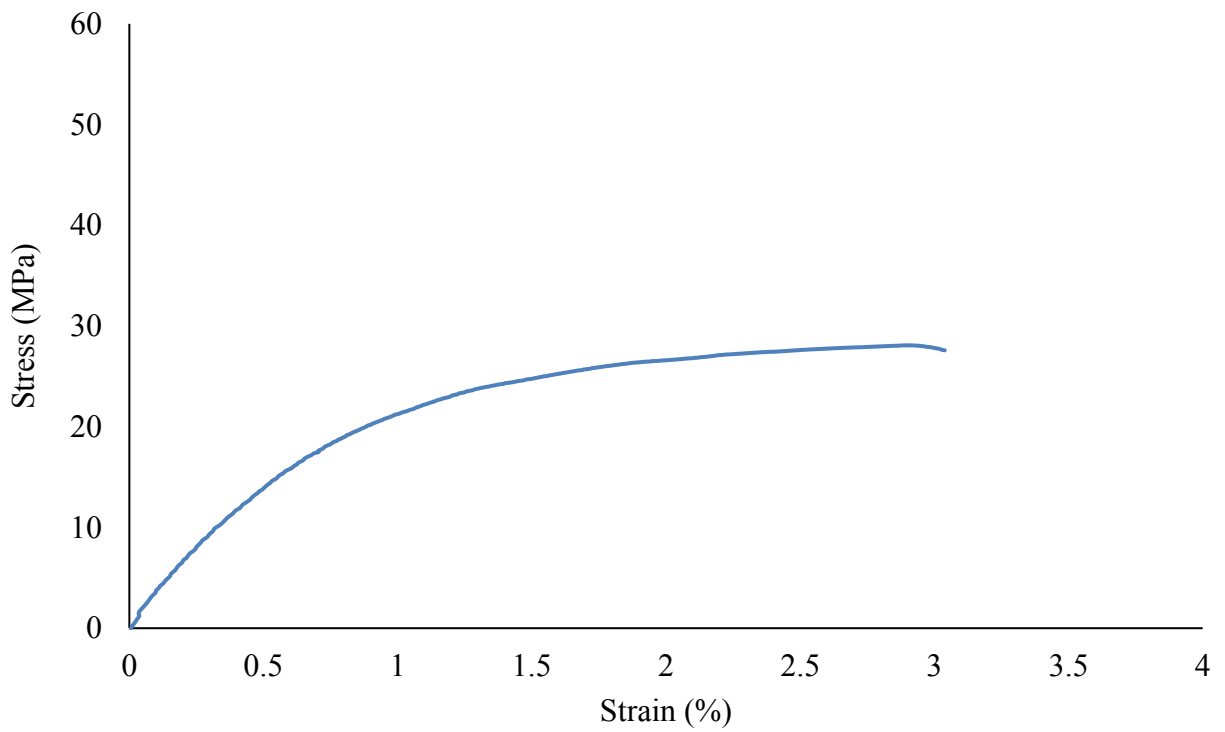


Figure B-9. Stress strain curve for sample 6 ($E = 2.50$ GPa)

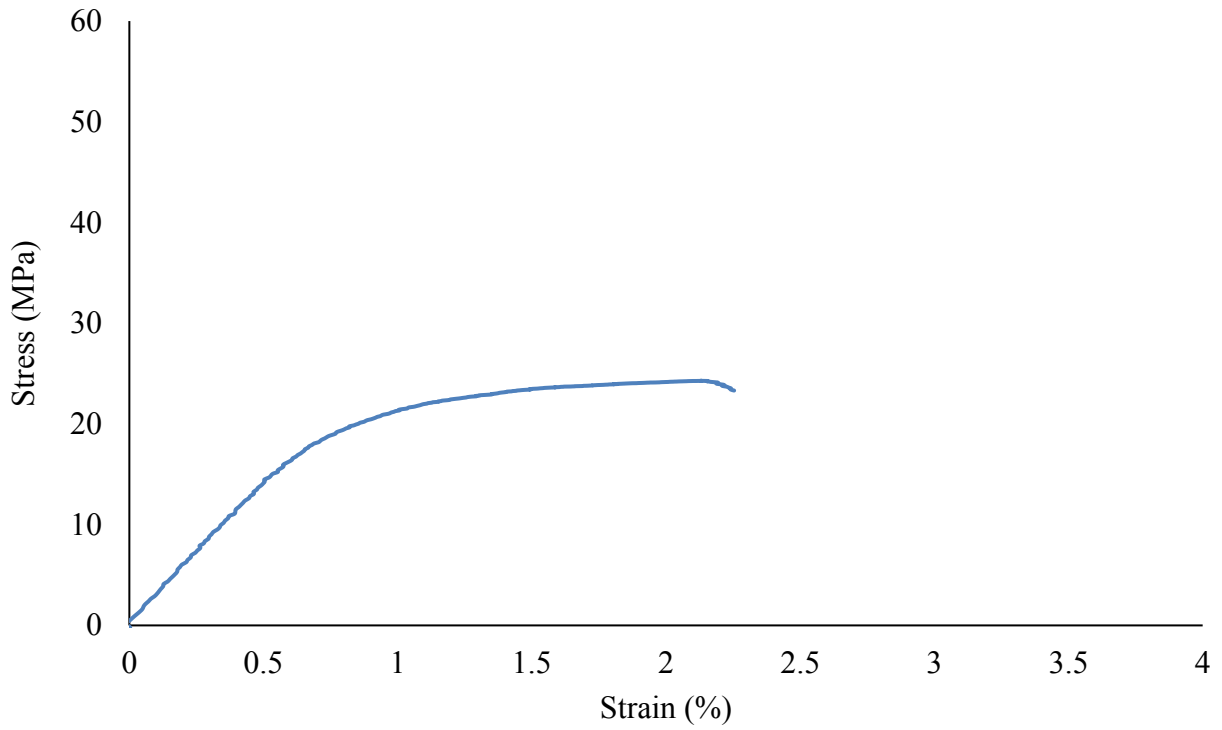


Figure B-10. Stress strain curve for sample 7 ($E = 2.67$ GPa)

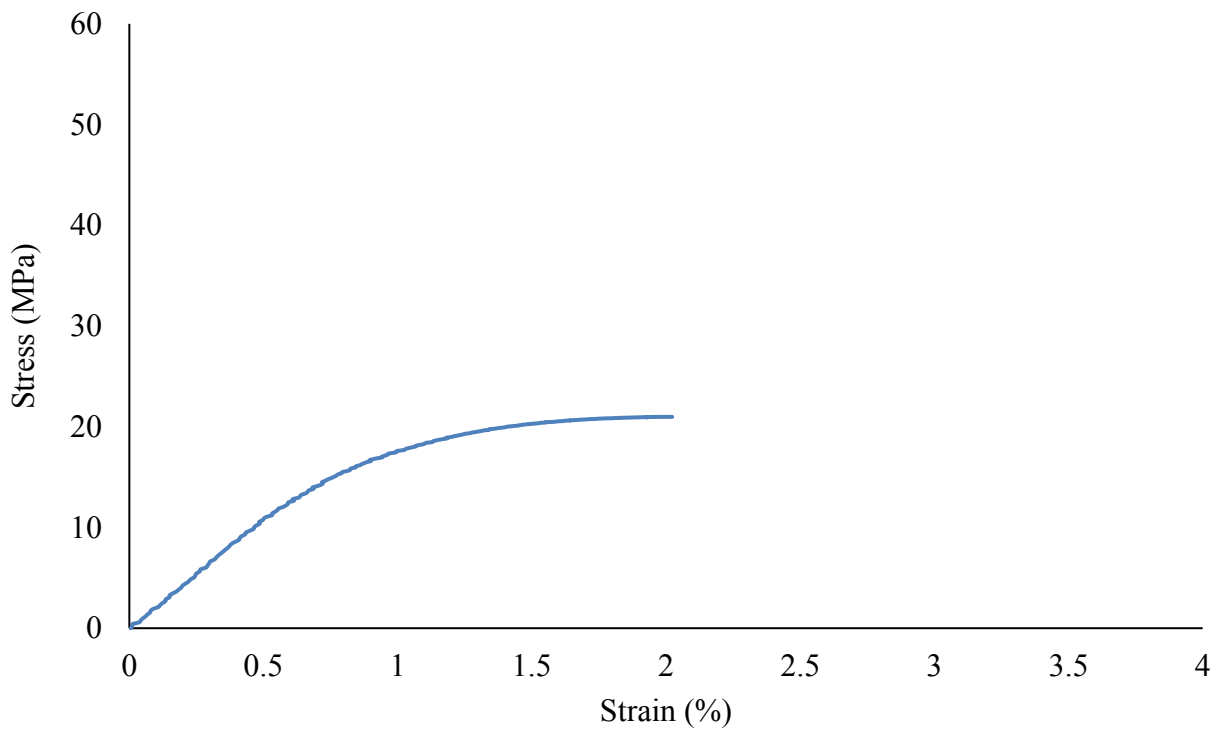


Figure B-11. Stress strain curve for sample 8 ($E = 2.09$ GPa)

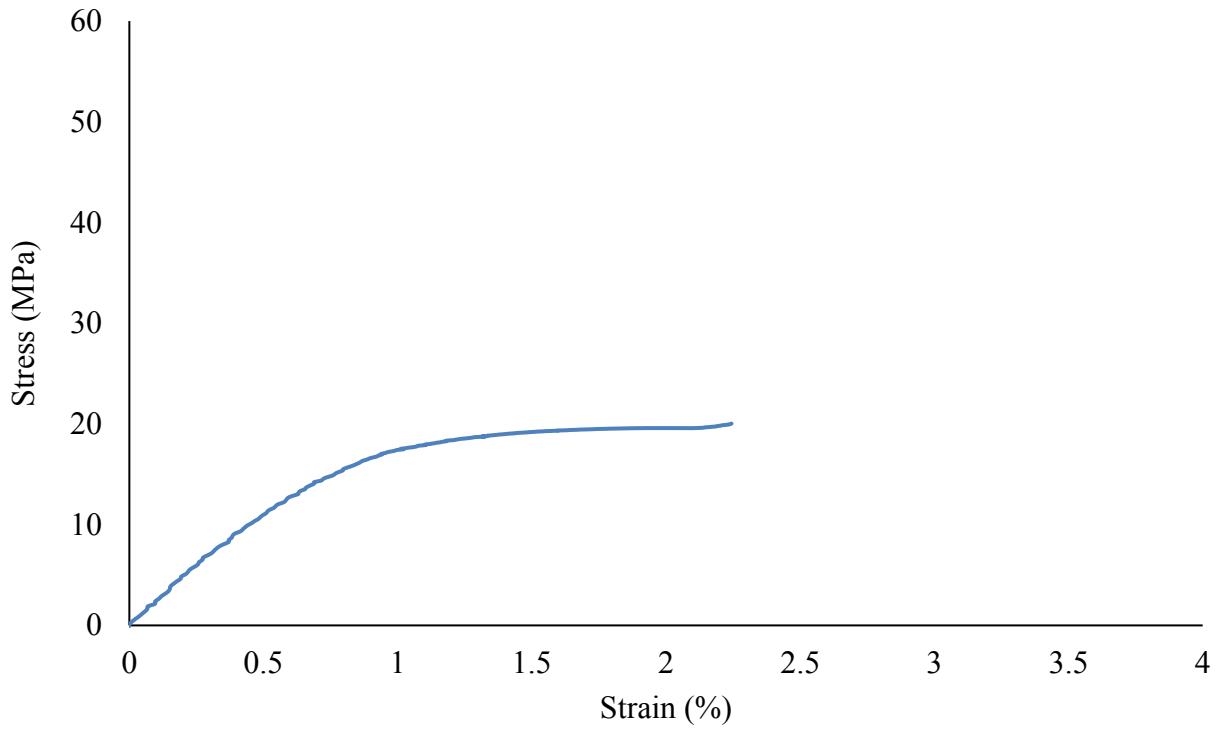


Figure B-12. Stress strain curve for sample 9 ($E = 1.94$ GPa)

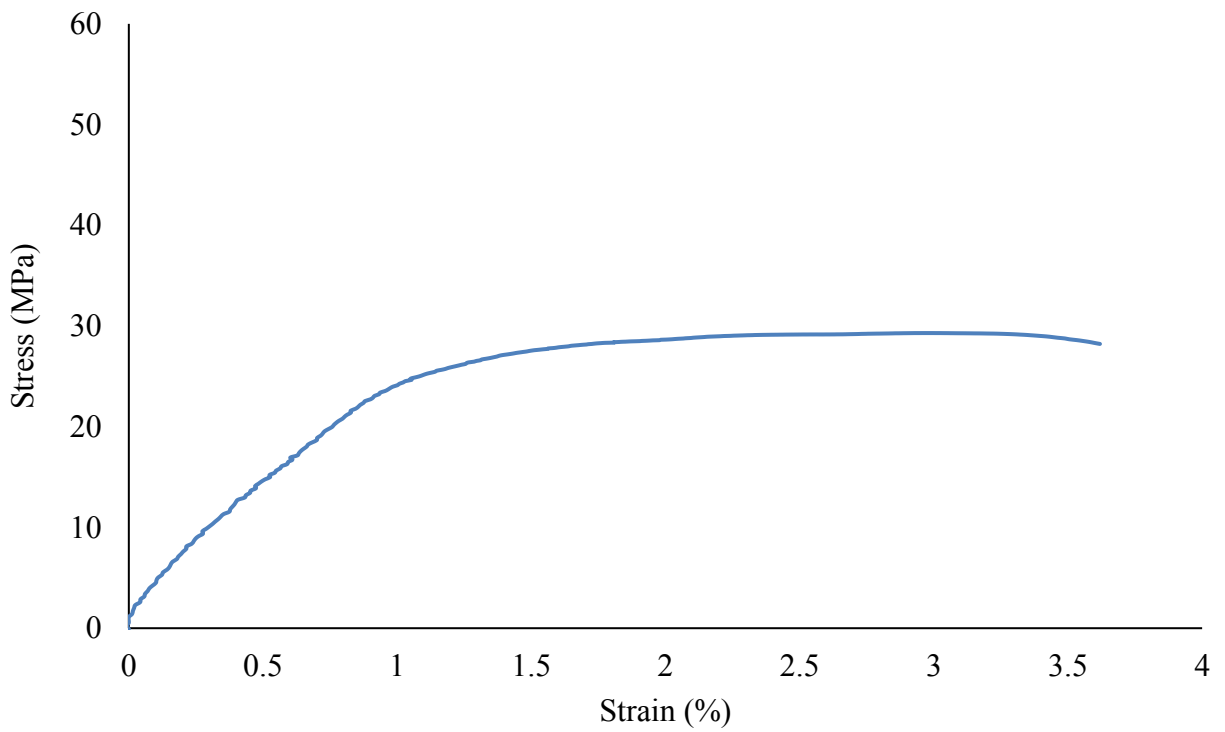


Figure B-13. Stress strain curve for sample 10 ($E = 2.42$ GPa)

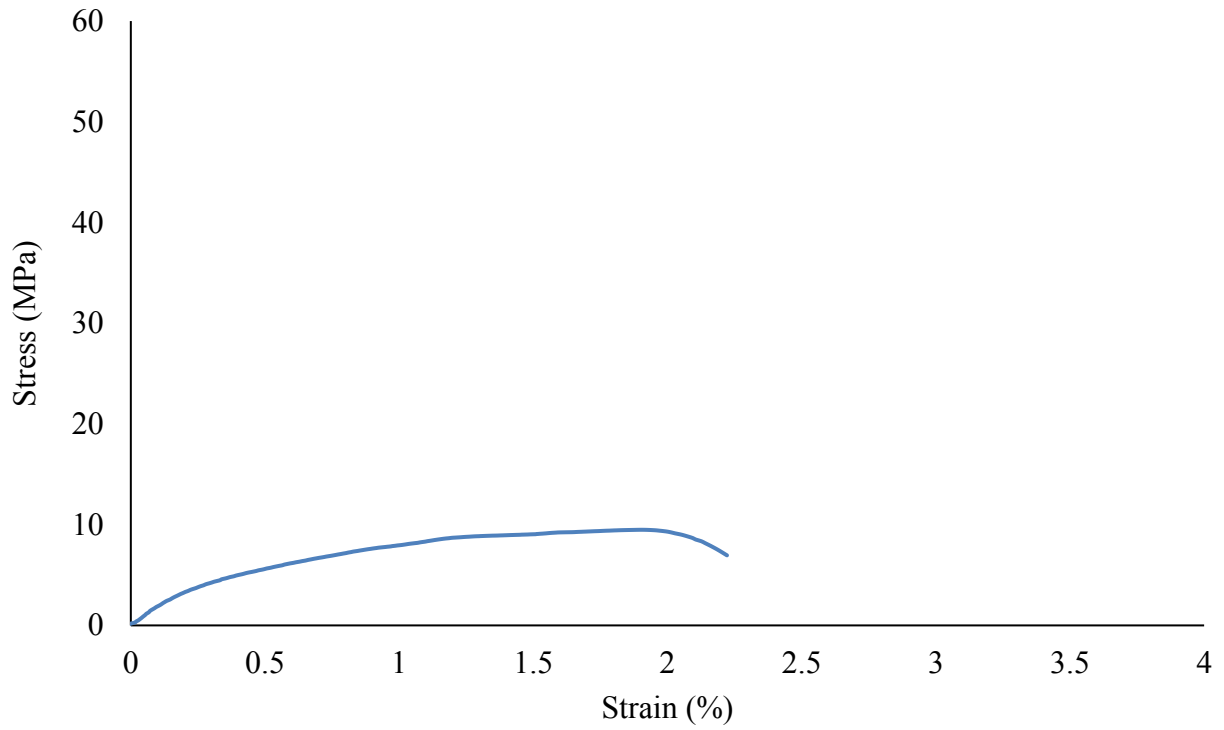


Figure B-14. Stress strain curve for sample 11 ($E = 1.68$ GPa)

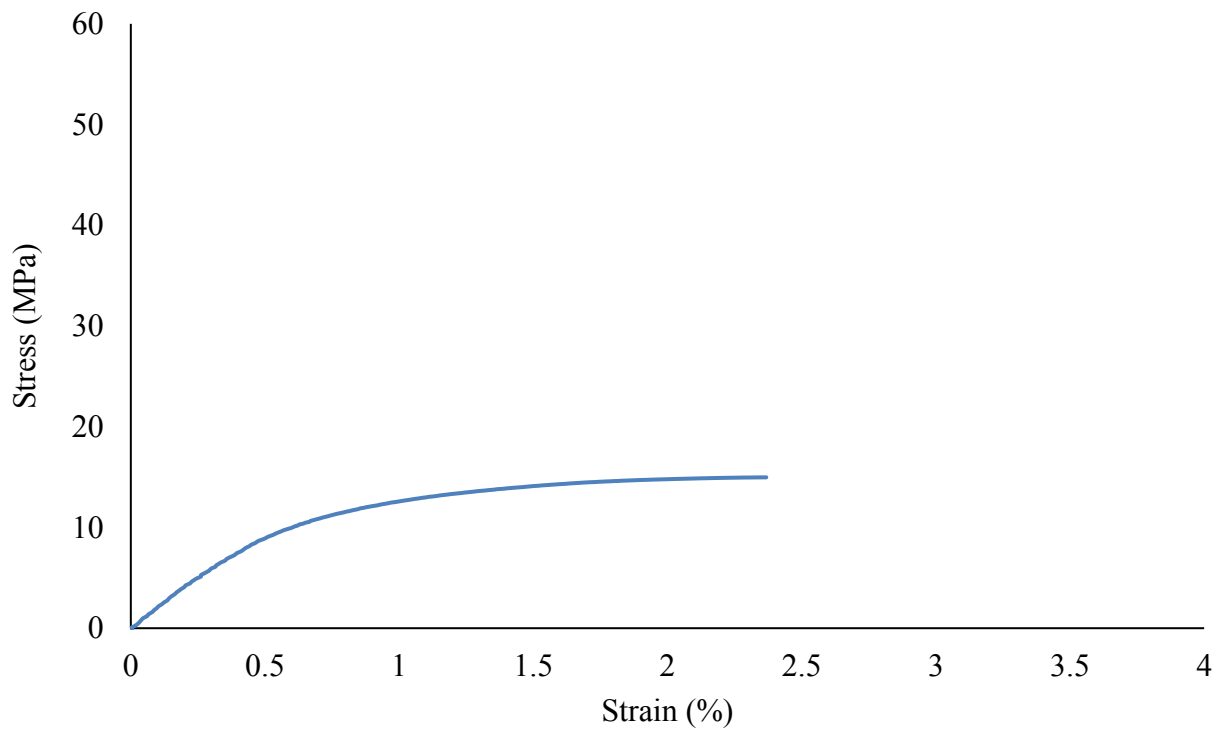


Figure B-15. Stress strain curve for sample 12 ($E = 1.99$ GPa)

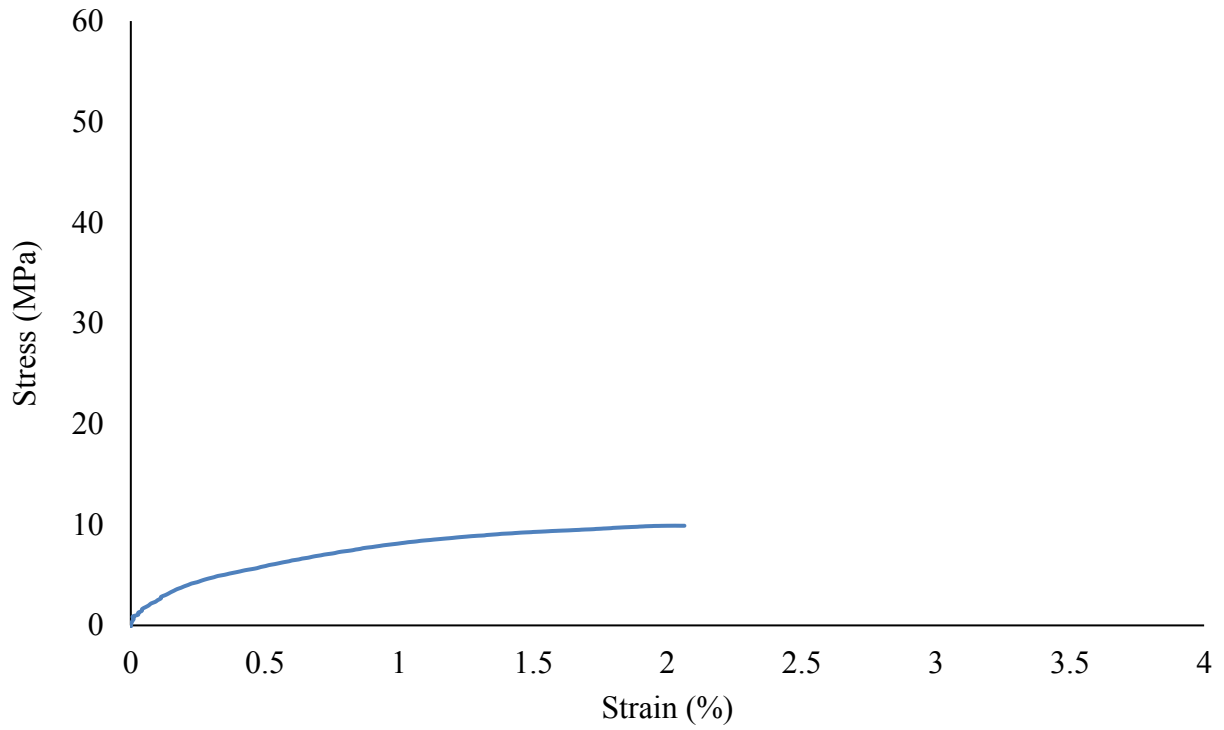


Figure B-16. Stress strain curve for sample 13 ($E = 1.89$ GPa)

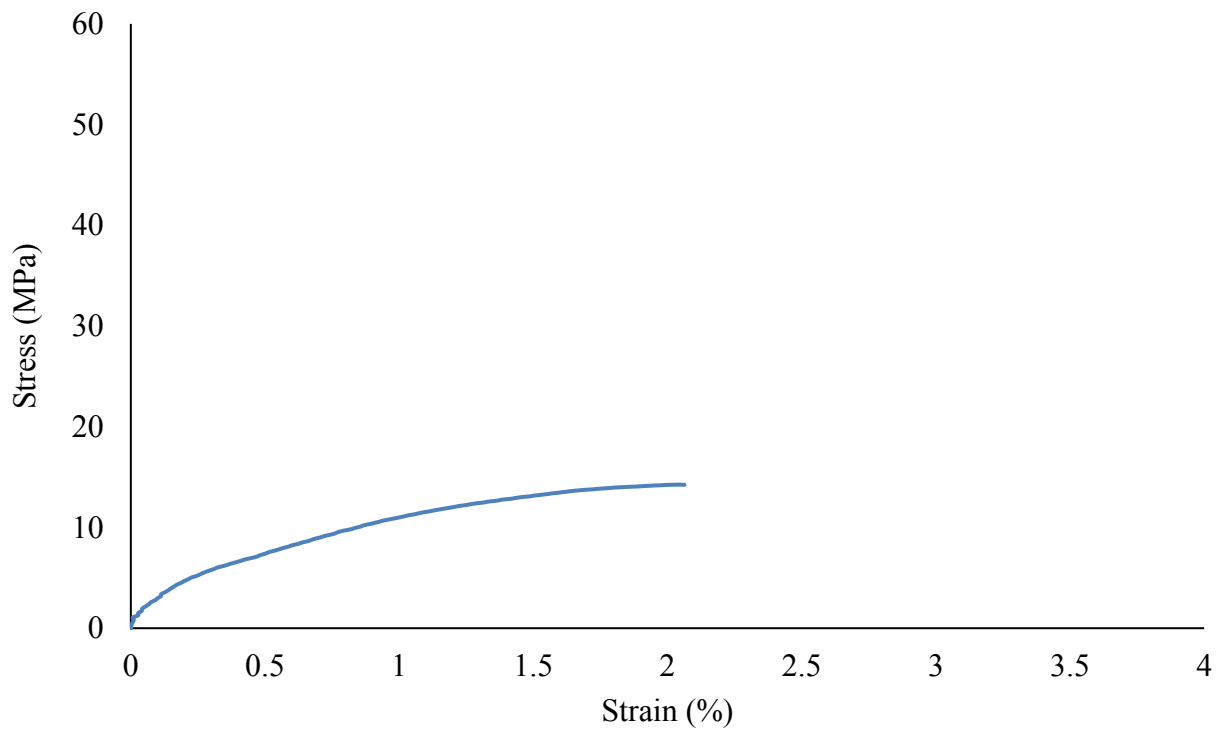


Figure B-17. Stress strain curve for sample 14 ($E = 2.14$ GPa)

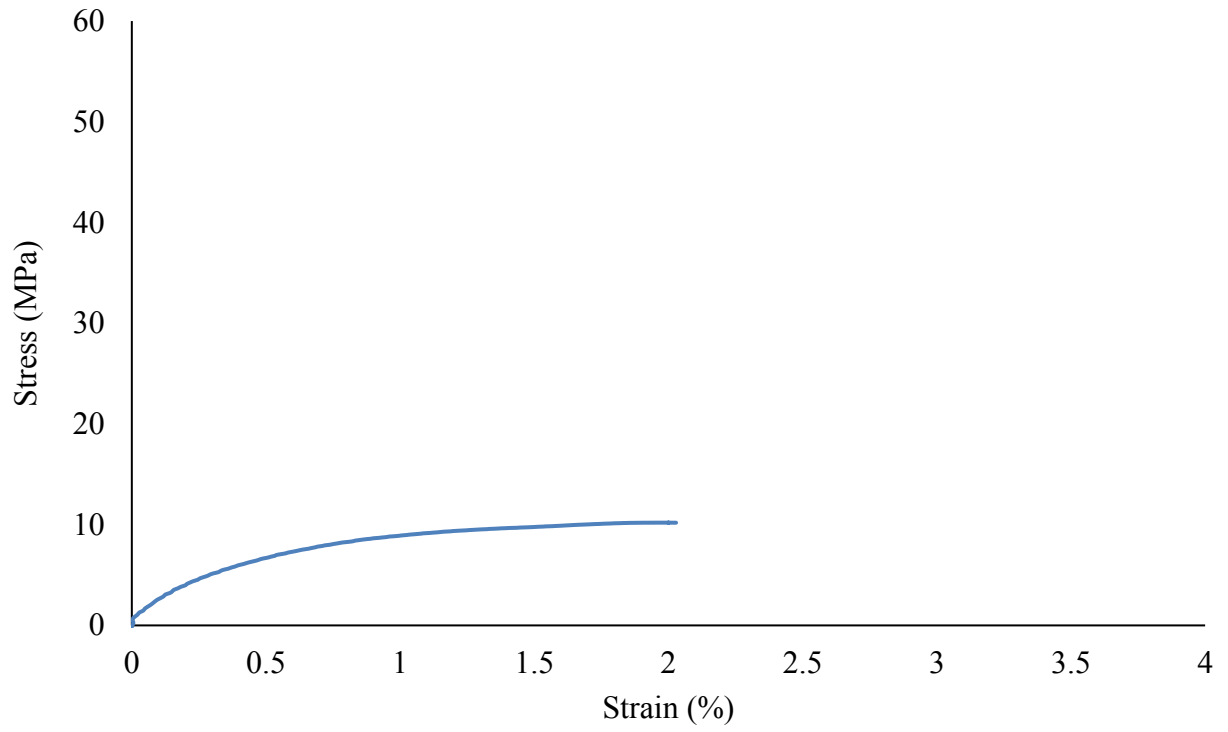


Figure B-18. Stress strain curve for sample 15 ($E = 1.40$ GPa)

B.3 Least Square Fitting

The following Matlab Code was used to perform least squares linear regression on the numerical stress-strain data to obtain the elastic modulus in the linear region.

```
data = sample1;

%define variables from data
X = data(:,1);
Y = data(:,2);
K = length(X);
X_bar = sum(X)/K;
Y_bar = sum(Y)/K;

%initiate sums at 0 for for loop
sum_XY = 0;
sum_X2 = 0;
sum_Y2 = 0;

%sum from 1 to K
for i = 1:K
    XY = sum_XY + sum(X(i)*Y(i));
    X2 = sum_X2 + sum(X(i)^2);
    Y2 = sum_Y2 + sum(Y(i)^2);
    sum_XY = XY;
    sum_X2 = X2;
    sum_Y2 = Y2;
end

%calculate modulus with Least Squares Fitting equation (9.3.2 ASTM E111)
E = (sum_XY - (K*X_bar*Y_bar))/(sum_X2-(K*(X_bar^2)))*10^-3;

%calculate coefficient of determination
r2 = (sum_XY - (sum(X)*sum(Y)/K))^2/((sum_X2-(sum(X)^2/K))*(sum_Y2-(sum(Y)^2/K)));

%coefficient of variation
V1 = 100*sqrt(((1/r2)-1)/(K-2));

%save values to vector
results = [E;r2;V1];
```

Appendix C Digital Image Correlation Uncertainty Analysis

The objective of this analysis is to quantify the uncertainty in calculating the elastic modulus by estimating the uncertainty in the measurements in the initial test procedures and using error propagation to determine how these errors effect the final calculation of the elastic modulus.

C.1 Micrometer Measurements

The uncertainty in diameter measurements were taken from the worst case standard error for inner and outer diameter measurements.

$$\Delta d_i = \frac{\sigma}{\sqrt{n}} = \frac{0.20mm}{\sqrt{5}} = 0.0894 \text{ mm}$$

$$\frac{\Delta d_i}{d_i} = \frac{0.0894mm}{9.86 \text{ mm}} = 0.00907\%$$

$$\Delta d_o = \frac{\sigma}{\sqrt{n}} = \frac{0.15mm}{\sqrt{5}} = 0.0671 \text{ mm}$$

$$\frac{\Delta d_o}{d_o} = \frac{0.0671 \text{ mm}}{10.83 \text{ mm}} = 0.00620\%$$

C.2 Load Cell Measurements

Information on the accuracy of the load cell was not provided by the manufacturer so the catalogue data from another Instron load cell was used for the approximate error in linearity, repeatability and hysteresis. The total uncertainty was determined based on methods by Figliola *et. al* [1].

$$u_{lin} = 0.25\% \text{ of reading}$$

$$u_{rep} = 0.25\% \text{ of reading}$$

$$u_{hist} = 0.1\% \text{ of reading}$$

$$u_{res} = 1\% \text{ of reading (ASTM E4 [2])}$$

$$\Delta P = \sqrt{0.25^2 + 0.25^2 + 0.1^2 + 1} = 1.06\%$$

C.3 Strain Measurements

The strain error was estimated by artificially displacing a sample by translating by a varying number of pixels. Since the strain should be 0 as no deformation occurs, the strain output from DaVis due to the artificial displacement was estimated to be the approximate error.

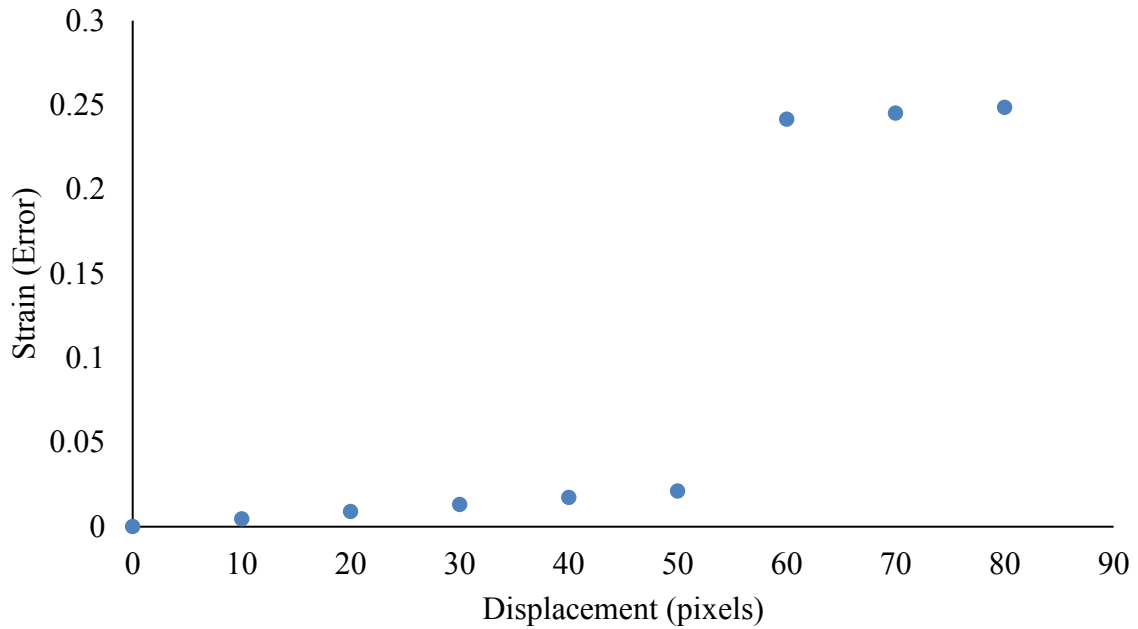


Figure C-19. Strain error as a function of rigid body displacement

$$\Delta S = 0.0212 \%$$

C.4 Error Propagation

The error in cross-sectional area of the samples was propagated by C.1 and the error in stress was then determined from C.2.

$$\frac{\Delta A}{A} = \sqrt{\left(\frac{\Delta d_o}{d_o}\right)^2 + \left(\frac{\Delta d_i}{d_i}\right)^2} = 0.011 \quad (\text{C.1})$$

$$\frac{\Delta \sigma}{\sigma} = \sqrt{\left(\frac{\Delta P}{P}\right)^2 + \left(\frac{\Delta A}{A}\right)^2} = 1.0601 \quad (\text{C.2})$$

The resulting error in elastic modulus was then determined from the errors in stress and strain values from C.3.

$$\frac{\delta E}{E} = \sqrt{\left(\frac{\Delta \sigma}{\sigma}\right)^2 + \left(\frac{\Delta S}{S}\right)^2} \quad (\text{C.3})$$

The total uncertainty in the elastic modulus value was determined as 1.0603%.

C.4 References

- [1] R. Figliola and D. Beasley, *Theory and Design for Mechanical Measurements*, 6th Edition, Wiley, Jan 2015.
- [2] “Standard Practices for Verification of Force Testing Machines,” ASTM International, E4-16, June 2016.